

**Project Report  
NASA/L-2**

# **Wake Vortex Field Measurement Program at Memphis, TN Data Guide**

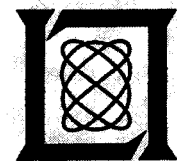
**S.D. Campbell  
T.J. Dasey  
R.E. Freehart  
R.M. Heinrichs  
M.P. Matthews  
G.H. Perras  
G.S. Rowe**

**14 January 1997**

---

**Lincoln Laboratory**  
MASSACHUSETTS INSTITUTE OF TECHNOLOGY  
*LEXINGTON, MASSACHUSETTS*

---



Prepared for the National Aeronautics and Space Administration  
Langley Research Center, Hampton, Virginia 23681-0001.

**ACCESSION NUMBER**

**395273**

**FEB 3 1997**

**ARCHIVES  
MIT LINCOLN LABORATORY**

This document is available to the public through  
the National Technical Information Service,  
Springfield, Virginia 22161.



**MIT LINCOLN LABORATORY  
Document Control**



## ABSTRACT

Eliminating or reducing current restrictions in the air traffic control system due to wake vortex considerations would yield increased capacity, decreased delays, and cost savings. Current wake vortex separation standards are widely viewed as very conservative under most conditions. However, scientific uncertainty about wake vortex behavior under different atmospheric conditions remains a barrier to development of an adaptive vortex spacing system.

The objective of the wake vortex field measurement efforts during December, 1994 and August, 1995 at Memphis, TN were to record wake vortex behavior for varying atmospheric conditions and types of aircraft. This effort is part of a larger effort by the NASA Langley Research Center to develop an Aircraft Vortex Spacing System (AVOSS) as an element of the Terminal Area Productivity (TAP) program. The TAP program is being performed in concert with the FAA Terminal Air Traffic Control Automation (TATCA) program and ATC Automation.

Wake vortex behavior was observed using a mobile continuous-wave (CW) coherent laser Doppler radar (lidar) developed at Lincoln Laboratory. This lidar features a number of improvements over previous systems, including the first-ever demonstration of an automatic wake vortex detection and tracking algorithm. An extensive meteorological data collection system was deployed, including a 150-foot instrumented tower, wind profiler/RASS (radio acoustic sounding system), sodar and balloon soundings. Aircraft flight plan and beacon data were automatically collected to determine aircraft flight number, type, speed and descent rate. Additional data was received from airlines in post-processing to determine aircraft weight and model. Wake vortices from several hundred arriving aircraft were measured during various times of the day over several weeks. This document describes the methods of data collection and analysis, and the content and formats of the available data.



## ACKNOWLEDGMENTS

The authors wish to thank David Hinton, George Greene, Roland Bowles, and Fred Proctor of NASA Langley Research Center for their advice and support. Thank you also to Al Zak of NASA Langley Research Center for his analysis and contribution to the summary of meteorological data. We also wish to thank Robert Beesley (Memphis International Airport), Major Michael Armour (Tennessee National Guard), Captain Randy Myers (Tennessee Air National Guard), Robert Lester (Federal Express), Paul Van Fossen (Northwest Airlines), Lee McGlamery (FAA Memphis Airport Tower), Gerald Vowell (FAA Memphis Sector Field Office) and Martha Henderson (FAA Memphis Airports District Office). We wish to thank NOAA, particularly Kirk Clawson, for contributing to the experimental design and sensors of the meteorological measurement system. The Volpe Transportation Systems Center and its contractors, particularly Dave Burnham and Steve Abramson, offered much experience and insight into vortex measurement and contributed to the meteorological sensor suite. The authors wish to thank Mark Isaminger, Ben Boorman, Brad Crowe and Durant White of the Lincoln Memphis field office, and Frank Yachimski, Maurice Couture and Scott Littlefield of Lincoln. Special thanks to Skip Copeland for his invaluable administrative assistance.



## TABLE OF CONTENTS

<b><u>Section</u></b>	<b><u>Page</u></b>
Abstract	iii
Acknowledgments	iv
1. INTRODUCTION	1
1.1. Overview	1
1.2. Background	1
1.3. Memphis Data Collection Systems	2
1.4. Organization of Report	3
2. VORTEX DATA COLLECTION AND PROCESSING	5
2.1. Wake Vortex Measurement System	5
2.1.1. Lidar Design	5
2.1.2. Scan Strategies	6
2.1.3. High-Level Software Organization	7
2.1.4. Alignment and Calibration Procedures	18
2.2. Vortex Data Processing	20
2.2.1. Vortex Position Estimation	20
2.2.2. Circulation Definition and Basic Calculation	22
2.2.3. Vortex Tangential Velocity Determination	32
2.2.4. Selected Circulation Results	36
2.2.5. Synopsis of Circulation Calculation Procedure	44
2.2.6. Circulation Computation Summary	45
3. METEOROLOGICAL DATA COLLECTION AND PROCESSING	47
3.1. Instrumented Tower	48
3.2. Profiler/RASS	51
3.3. Sodar	51
3.4. Balloon-LORAN System	51
3.5. Miscellaneous Sensors	52
3.6. Computer Systems	53
3.6.1. ASTER Data Acquisition Module (ADAM)	54
3.6.2. Campbell Scientific Datalogger	54
3.6.3. Sun SPARC5 Workstation at Shed	54
3.6.4. Sun SPARC5 Workstation at Lincoln Memphis Office	56
3.7. Alignment and Calibration	57
3.8. Sensor Limitations	57
3.9. Meteorological Processing	58
3.10. Atmospheric Profiles	59
4. AIRCRAFT DATA COLLECTION AND PROCESSING	61
5. FIELD MEASUREMENTS	63
5.1. Field Deployment Sites	63
5.2. Case Lists	63
5.3. Hourly Weather Observations and General Comments	67

## TABLE OF CONTENTS (Continued)

<b><u>Section</u></b>	<b><u>Page</u></b>
6. SUMMARY	71
APPENDIX A: DATA FORMATS	73
APPENDIX B: LIDAR SITE DESCRIPTIONS	85
APPENDIX C: PARAMETER SETTINGS	91
APPENDIX D: METEOROLOGICAL SENSOR CHARACTERISTICS	93
ACRONYMS AND ABBREVIATIONS	95
GLOSSARY OF MATHEMATICAL SYMBOLS	97
REFERENCES	99



## LIST OF ILLUSTRATIONS

<u>Figure</u>	<u>Page</u>
1. Memphis wake vortex field measurement system.	2
2. Post-processing system.	3
3. Wake vortex detection lidar design.	5
4. Lidar scanning strategies.	6
5. Functional outline of the high-level lidar software.	8
6. Lidar high-level software interconnectivity diagram.	9
7. Sample color-coded spectrum display.	15
8. Lidar software graphical user interface (GUI).	17
9. Effect of manual angle editing on detected vortex angles and resulting tracks for MEM case 1252.	21
10. Assumed circularly symmetric flow field of a wake vortex, showing the radial dependence of the tangential velocity.	24
11. Theoretical spectra corresponding to a lidar beam focused on a vortex, with the beam passing 7 m from the center of the vortex.	24
12. Geometry for circulation estimation in the presence of the neighboring vortex, lidar looking straight up at vortex.	27
13. Relative circulation versus vortex pair separation for various radius averaging regimes, calculated from Equation (22).	27
14. (a) Diagram showing geometry of lidar scanning a pair of vortices with azimuth angle $q$ . (b) Geometry used for numerical calculation of circulation.	28
15. Coordinate system definition for numerical calculation of Figure 14.	28
16(a). Relative circulation increase due to second vortex versus angle between lidar LOS and line connecting vortices.	30
16(b). Same as Figure 16(a) except the radius averaging range is 5 m – 15 m for each curve and the vortex separations for each curve correspond to the aircraft shown.	30
16(c). Same as Figure 16(b) except the circulation is calculated with only maximum velocities out to 12 m beyond the primary vortex.	31
17(a). Hanning window function from equation (26).	34
17(b). The corresponding power spectra of the Hanning window (solid line) and Gaussian profile (dashed line) versus the relative frequency in spectral bins.	34
18. Zero-Doppler peak averaged over 20 spectra (points) with Gaussian fit (solid line)	37
19. Velocity versus cross range for a scan through a B727 vortex comparing the results for the three velocity estimation algorithms considered.	37
20. Plots of individual spectra corresponding to the location as shown in Figure 17.	38
21. Circulation normalized to the initial theoretical value versus time for several representative aircraft.	40
22. Same as Figure 21 except for different aircraft.	41
23. Normalized circulation versus time for DC9, 727, and A320 aircraft over an entire push.	42

## LIST OF ILLUSTRATIONS (Continued)

<u>Figure</u>	<u>Page</u>
24. Same as Figure 23 except 757, A300, and DC10 aircraft data are shown.	43
25. Memphis airport meteorological site.	47
26. 150-foot instrumented tower.	49
27. Orientation of Wind Monitor to tower structure.	50
28. Tower site layout & soil sensors.	53
29. Meteorological data collection computer system.	55
30. Memphis airport lidar sites with distances to touchdown zone for 1995 deployment.	64
A-1. Runway Axis Coordinate System.	73
A-2. Lidar Axis Coordinate System.	74
B-1. Armory lidar sites.	86
B-2. Tchulahoma lidar site (plan view).	87
B-3. Tchulahoma lidar site (surface profile).	88
B-4. Lidar sites along runway 27.	90

## LIST OF TABLES

<u>Table</u>	<u>Page</u>
1 Scan Mode Control Table	13
2 Theoretically Calculated Power Signal-to-Noise for the Lidar Return from a Vortex at 300 m Range for Various Atmospheric Conditions	19
3 Memphis Wake Vortex Case List	65
4 Memphis Aircraft Types Sorted by Traffic Push	66
A-1 Wake Vortex Summary File Contents	75
A-2 Wake Vortex Location and Circulation Estimates	77
A-3 Lidar Crosswind File Header Data	78
A-4 Lidar Crosswind File Estimate Data	78
A-5 SAVPAK Data File Contents	79
A-6 FLUXPAK Data File Contents	81
A-7 Soil Data File Contents	82
A-8 Atmospheric Profile File Contents	83
D-1 Meteorological Sensor Characteristics	93

# 1. INTRODUCTION

## 1.1. Overview

This report describes wake vortex field measurements conducted during December, 1994 (Campbell, et al., 1995) and August, 1995 (Dasey, et al., 1996) at Memphis, TN. This effort is part of a larger effort by the NASA Langley Research Center to develop an Aircraft Vortex Spacing System (AVOSS) (Hinton, 1995) as an element of the Terminal Area Productivity (TAP) program. The TAP program is being performed in concert with the FAA Terminal Air Traffic Control Automation (TATCA) program and ATC Automation.

Wake vortex behavior was observed using a mobile continuous-wave (CW) coherent laser Doppler radar (lidar) developed at Lincoln Laboratory (Heinrichs, et al., 1995; Heinrichs, et al., 1996). This lidar features a number of improvements over previous systems, including the first-ever demonstration of an automatic wake vortex detection and tracking algorithm (Dasey and Heinrichs, 1995). An extensive meteorological data collection system was deployed, including a 150-foot instrumented tower, wind profiler/RASS (radio acoustic sounding system), sodar and balloon soundings (Matthews, et al., 1997). Aircraft flight plan and beacon data were automatically collected to determine aircraft flight number, type, speed and descent rate. Additional data was received from airlines in post-processing to determine aircraft weight and model. Several hundred aircraft vortices were measured during various times of the day over several weeks. This document describes the methods of data collection and analysis, and the content and formats of the available data.

## 1.2. Background

Significant restrictions currently exist in the air traffic control system due to wake vortex considerations. Eliminating or reducing these restrictions would yield increased capacity, decreased delays and significant cost savings (Evans and Welch, 1991). Current wake vortex separation standards are widely viewed as very conservative under most conditions. However, scientific uncertainty about wake vortex behavior under different atmospheric conditions remains a barrier to development of an adaptive vortex spacing system.

Wake vortex measurements have been conducted in the U.S. and elsewhere since the late 1960s (Olsen, et al., 1971). A number of sensors have been employed for wake vortex measurements, including CW lidar (Huffaker, et al., 1970; Burnham, 1977; Koepp, 1991; Constant, et al., 1994), pulsed lidar (Hannon, et al., 1994), anemometer lines and acoustic sensors (Page et al., 1991). Early wake vortex measurements were often not accompanied by suitable atmospheric measurements. This deficiency became more apparent with the publication of an approximate theory of wake vortex behavior relating circulation decay and descent rate to nondimensionalized atmospheric conditions (i.e., normalized to aircraft characteristics) (Greene, 1986).

More recent wake vortex field measurements were made during tower fly-by tests at Idaho Falls in 1990 (Page, et al., 1991). A major aim of this effort was to collect wake vortex, atmospheric and aircraft data under controlled conditions. A variety of wake vortex sensors were employed, including an instrumented tower, CW lidar, monostatic acoustic vortex sensing system (MAVSS) and an anemometer line. Atmospheric data was collected with a tether sonde, tower and the flight profiles of the test aircraft were carefully controlled. While constituting the most comprehensive set of measurements to that time, the experimental protocol suffered from some deficiencies. Only three types of aircraft were studied (Boeing 727, 757 and 767), the aircraft made low passes instead of actually landing, and data were collected on only two days for each type.

### 1.3. Memphis Data Collection Systems

The elements of the Memphis field measurement program are summarized in Figure 1. These elements include wake vortex measurements, atmospheric measurements and aircraft data collection.

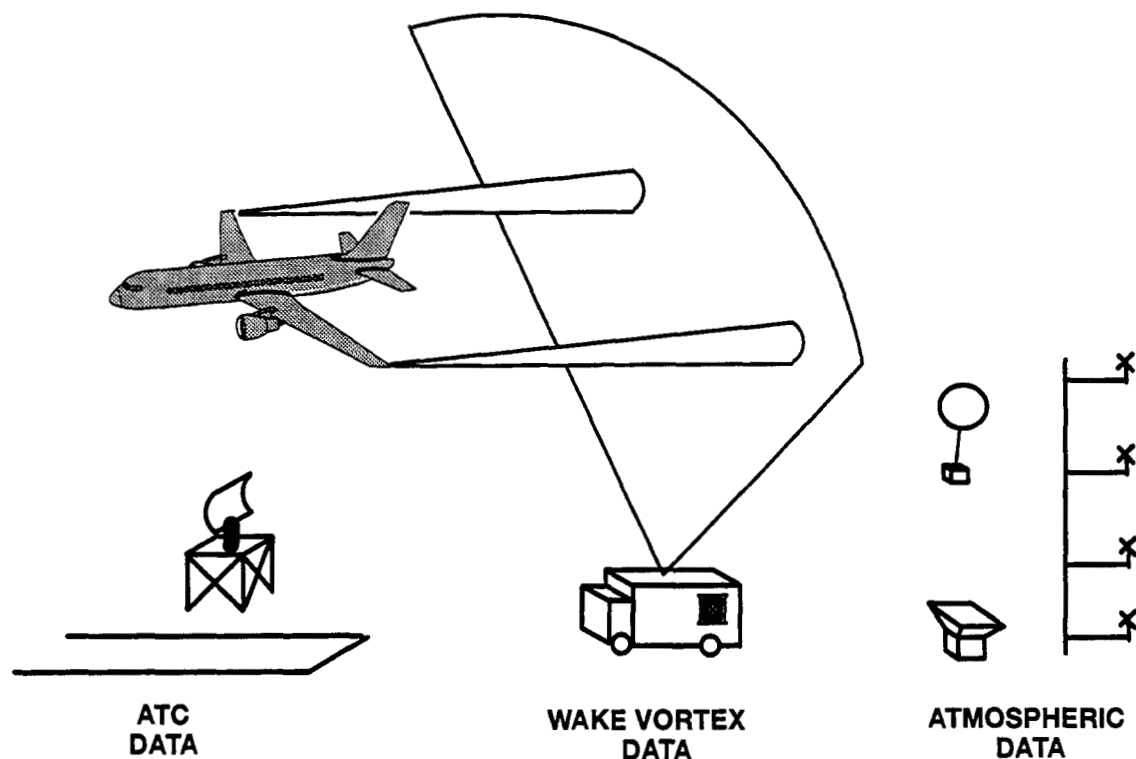


Figure 1. Memphis wake vortex field measurement system.

Wake vortex measurements were performed by a van-mounted  $10.6\ \mu\text{m}$   $\text{CO}_2$  CW lidar (Heinrichs, et al., 1995; Heinrichs, et al., 1996). The lidar measures line-of-sight velocities in a plane perpendicular to the flight path in order to characterize vortices generated by approaching or departing aircraft. An algorithm was developed to allow the lidar to automatically recognize, track and characterize wake vortices (Dasey and Heinrichs, 1995). Various lidar scanning strategies are employed to study wake vortices generated in, near and out of ground effect.

Atmospheric data were obtained from several sources (Matthews, et al., 1997). These sources consist of a 150-foot tower instrumented with various meteorological sensors, a profiler with the RASS option, a phased array sonic radar (Sodar), radiosonde balloon launches, and a group of soil sensors. The instrumentation was located at the Memphis International Airport between the two primary north-south runways.

Aircraft beacon and flight plan data data was obtained from the Air Traffic Control (ATC) system. The major air carriers at Memphis contributed information on the weight and model of each jet aircraft.

Due to the diverse nature of the data sources, post-processing is required to analyze and correlate the data. The overall design of the post-processing system is shown in Figure 2. The lidar data

processing, meteorological processing, aircraft data processing, and the summary data file processing are described in the following sections.

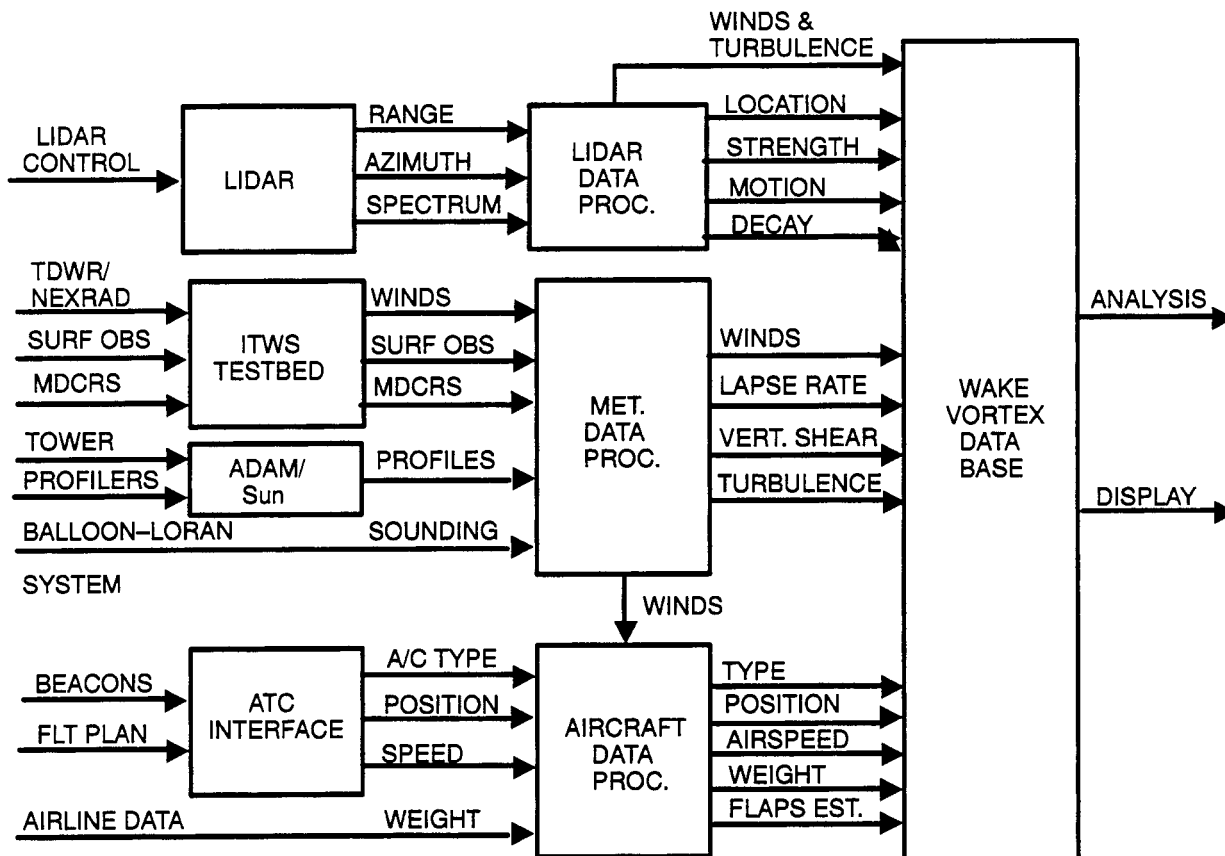


Figure 2. Post-processing system.

#### 1.4. Organization of Report

This report is organized into four sections and three appendices. Section 2 describes the lidar and vortex data processing systems. Section 3 describes the meteorological sensors and data. Section 4 discusses the aircraft data processing. Section 5 provides a data summary, including the deployment sites, aircraft types, hours of collection and related data. Section 6 describes future work and Section 7 provides a summary. Appendix A contains the data formats for the summary, lidar and meteorological data. Appendix B provides detailed descriptions of the lidar sites, and Appendix C lists the parameter settings used during the data collection period. Appendix D provides the detailed meteorological sensor characteristics.



## 2. VORTEX DATA COLLECTION AND PROCESSING

### 2.1. Wake Vortex Measurement System

#### 2.1.1. Lidar Design

The Coherent CW lidar operates by combining the atmospheric return with a reference on an optical detector. The interference between these signals creates a beat signal with a frequency related to the Doppler shift of the backscattered laser from motion of the atmospheric particles. At  $10.6\ \mu\text{m}$  the scatterers are primarily aerosols. The lidar design (Figure 3) is similar to those used in previous work (Huffaker, et al., 1970; Burnham, 1977; Koepp, 1991; Constant, et al., 1994), but with some significant improvements. First, the reference laser is offset in frequency from the primary laser by 10 MHz in order to resolve positive and negative Doppler shifts. The design also features a fully digital signal processing (DSP) system which offers greater flexibility than the analog techniques previously used.

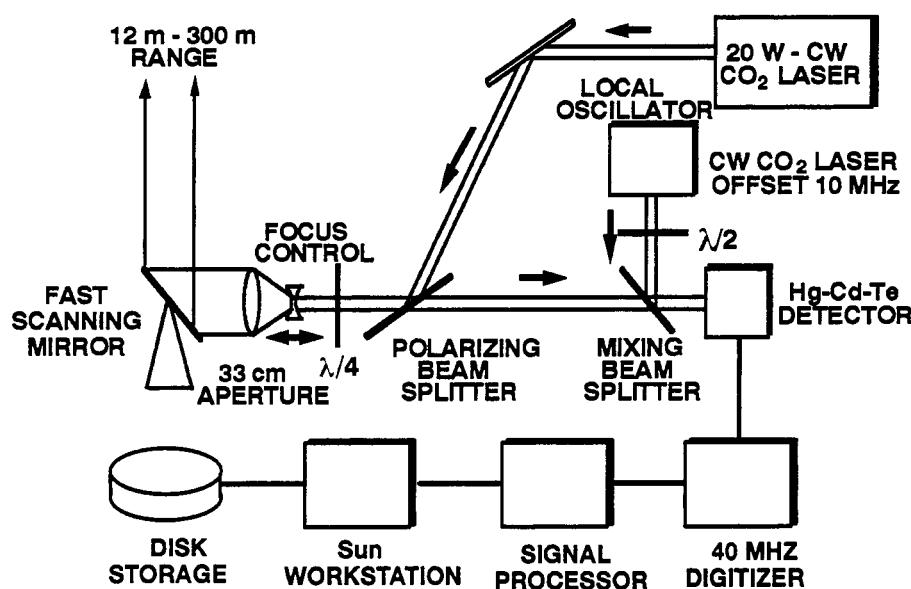


Figure 3. Wake vortex detection lidar design.

A CW lidar collects data by adjusting the focus range of the transmitted laser and scanning the beam across a region of interest. The lidar utilizes a 20 W CO<sub>2</sub> laser and a 33 cm aperture which provides an effective range resolution (related to the depth of focus) of  $\sim 6$  m at 100 m range. The range resolution increases as the square of the distance, which restricts the practical maximum measurement range to roughly 300 m. This range limitation was the primary reason that the wake vortex observations were almost entirely of landing aircraft. The lidar collects data while sweeping a range of angles in a vertical plane while at a constant focus range. The maximum sweep rate is in excess of  $180^\circ/\text{s}$ , but typical scan rates are between  $30^\circ/\text{s}$  and  $60^\circ/\text{s}$ .

The backscattered laser radiation is collected by the lidar transmit/receive aperture and directed onto a HgCdTe detector along with the reference laser beam where they create a beat signal at their difference frequency. This beat signal is measured by the detector and is then amplified, filtered and digitized with a 10-bit analog-to-digital convertor at a 40-MHz rate. Since the Doppler shift ( $\Delta\nu$ ) of

the backscattered radiation is related to the line-of-sight velocity of the scatterers by  $\Delta f = 2\Delta v/\lambda$ , the 20 MHz Nyquist frequency of the digitizer corresponds to a 106 m/s velocity bandwidth for the  $\lambda=10.6 \mu\text{m}$  wavelength of the lidar. The 10 MHz offset of the reference laser shifts this to an effective  $-53 \text{ m/s}$  to  $+53 \text{ m/s}$  velocity dynamic range. During the 8/95 Memphis field measurements, the system was arranged to continuously digitize  $256 \times 18$  points, requiring  $115 \mu\text{s}$  at the 40 MHz rate. These data were then stored temporarily in a buffer, while a Sharp LH9124 digital-signal-processor (DSP) calculated 18 individual power spectra, each containing 128 points and corresponding to a velocity resolution of 0.8 m/s. These power spectra were then averaged together and the single averaged spectra were sent to one of the Sun workstations. The Sun workstations collected these power spectra in this mode at an average rate of 300 Hz in 1995. In 1994, the system was arranged to provide 512 point power spectra averaged from 25 individual spectra. A slower Sun workstation was used in 1994, so that the Sun workstations collected spectra at an average rate of 60 Hz.

### 2.1.2. Scan Strategies

Figure 4 summarizes the scan strategies used to make the wake vortex measurements. The scan strategies are used to measure vortices out-of-ground effect (OGE), near ground effect (NGE) and in ground effect (IGE). The onset of ground effect occurs at an altitude of approximately half the generating aircraft's wingspan. As illustrated in the figure, vortices tend to descend downwards above this level and to diverge horizontally below it. The lidar scans in an arc-scan mode, where the focus range is left constant and the lidar sweeps a range of scan angles. The focus range is then changed for additional arc scans.

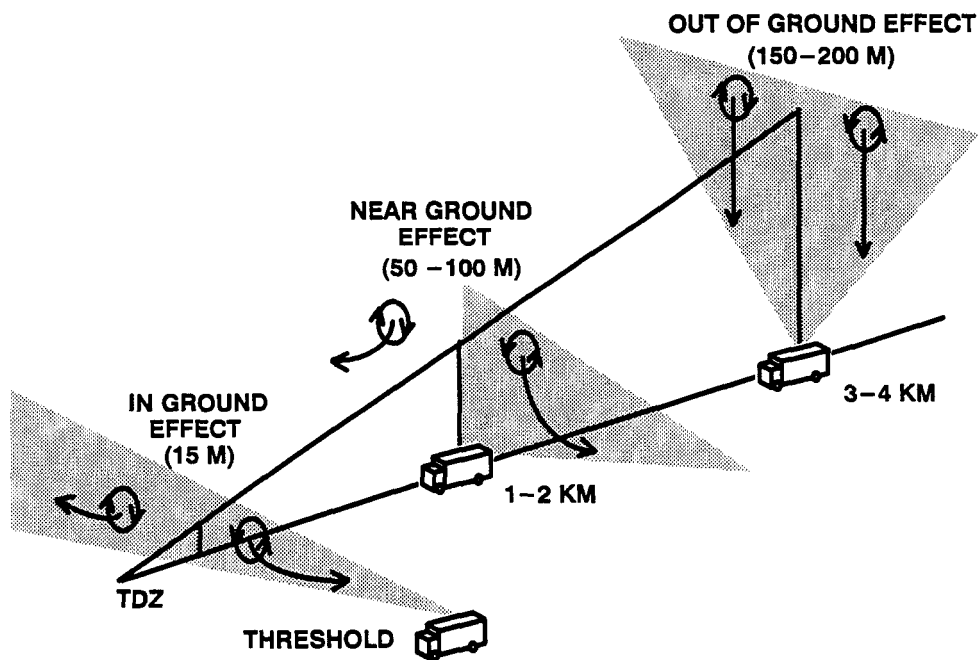


Figure 4. Lidar scanning strategies.



### 2.1.3. High-Level Software Organization

The output of the digital signal processor (DSP) is fed to two workstations which perform data archiving, vortex detection and tracking, data displaying, and scanning control. The workstations are VME-based Sun Sparc model 10 and 20 equivalents from Themis running SunOS 4.2.

A functional description of the workstation (DSP) processing is shown in Figure 5. The software is a mixture of C language and Interactive Data Language (IDL) on a UNIX operating system. The software consists of a set of processes communicating asynchronously via a Lincoln Laboratory interprocess communications library. Most C processes communicate using a TCP/IP communications protocol, with the exception of the spectra data stream, whose high bandwidth dictated the use of a shared-memory (SHM) protocol. IDL processes communicate with C processes via text pipes. A software processing diagram is shown in Figure 6. The following paragraphs detail the processing components indicated in Figure 6, with references to the specific software components in Figure 7. It should be noted that the vortex location and crosswind processing performed in the real-time system may differ somewhat from the methods used in post-processing the data and estimating the vortex locations for data delivery (described in section 2.2). These differences are generally due to computational constraints in the real-time system, where processing speed is important, or to development of more advanced processing techniques after the data collection exercises.

#### 2.1.3.1. Spectrum Labeling

Averaged power spectra are collected from the DSP during the time of active motion of the scanning mirror. Collection of the spectra from the DSP is suppressed while the focus range is being changed to allow time for the vortex location estimation routines. The spectra generated during the time of focus change is contaminated by the focus lens Doppler shift and vibration noise and so is not useful to the detection algorithms.

Each spectrum is tagged with a header which contains the time the spectrum was received by the workstation, the current focus range, declination angle, and scan mirror angle. The DSP waits until the workstation has received the spectra before beginning to process another. For this reason, the processing time for labeling the spectra with the collection point and time can limit the system data collection rate if the time required for this labeling is greater than the time the DSP requires to generate an averaged power spectrum. The spectra for each scan are buffered and processed further at the end of a scan to provide the highest possible data collection rate. The spectrum labeling processing tasks are undertaken by the *lidarServer* software module. Information about the focus and declination positions are received from the *mc* module, which received the data from the motor controller through a serial interface. Information about the scan mirror position is read from a scan mirror position encoder through a parallel interface.

#### 2.1.3.2. Vortex Location Estimation

The vortex location estimation is performed by the *vortrac* software module. Labeled power spectra (from the *lidarServer* module) are examined at the conclusion of each scan for evidence of the presence of wake vortices. If a vortex is found, its angular position and range are estimated and forwarded to subsequent processes. Otherwise, the crosswind profile is updated.

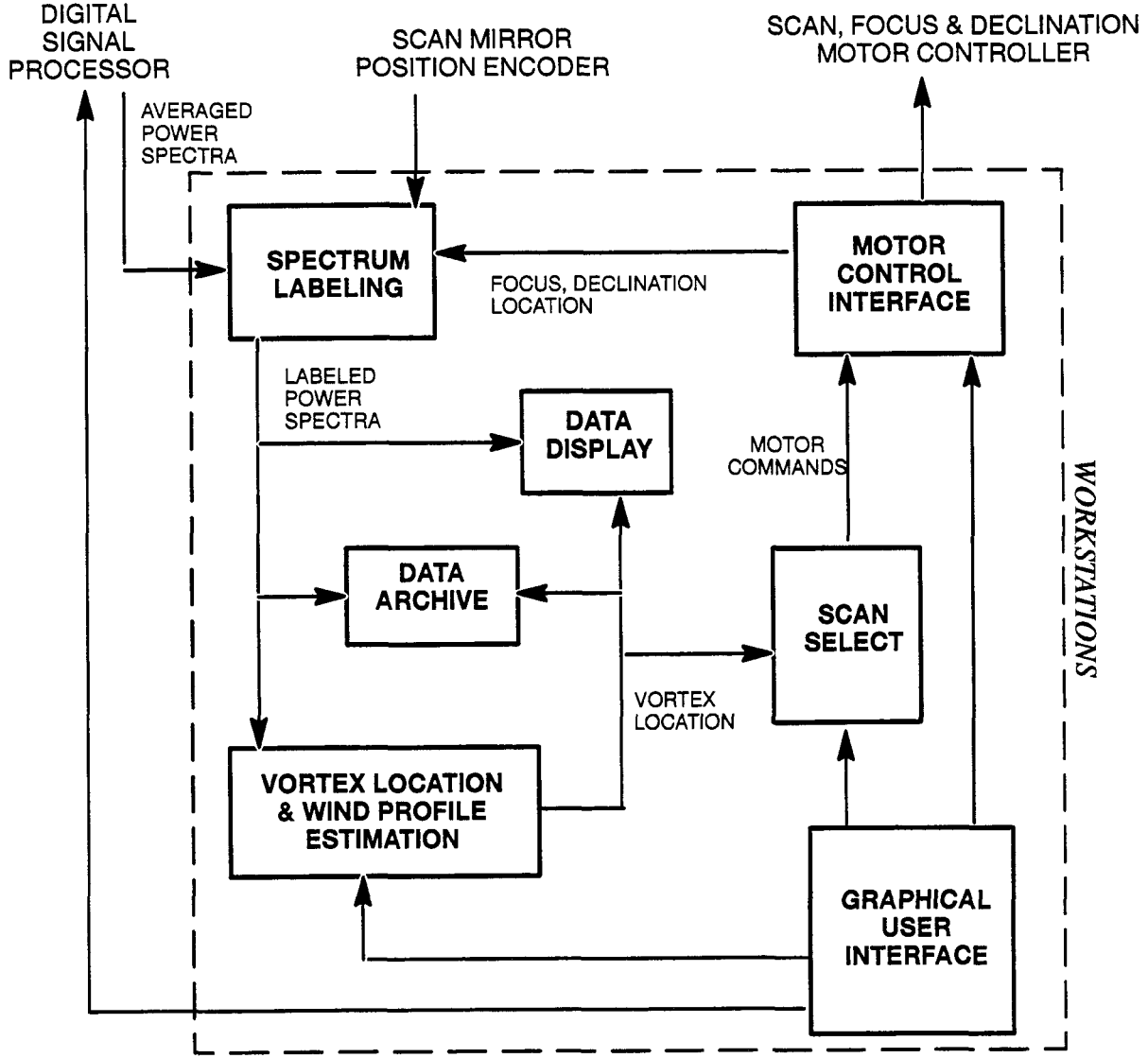


Figure 5. Functional outline of the high-level lidar software.

To begin the process of looking for a vortex, the maximum velocities are extracted from each spectrum. The maximum velocity ( $\Psi_i$ ) of a spectrum is defined as the spectrum velocity ( $V_k$ ) corresponding to the largest absolute velocity difference from a precomputed ambient wind bin ( $C_i$ ) for which the spectrum power ( $A_k$ ) exceeds the precomputed noise floor power ( $N_k$ ) for all bins ( $k$ ) in a spectrum, expressed as

$$\Psi_i = V_m \text{ where } m = (k \text{ where } \text{MAX} \{ |V_k - C_i| \} \forall A_k \geq N_k, 1 \leq k \leq n), \quad (1)$$

where  $n$  is the number of bins/spectrum. The Doppler velocity of each bin is determined as

$$V_k = P_{fl} * f_{BW} * \lambda * (k - K_{zd}) / (2.0 * n) \quad (2)$$

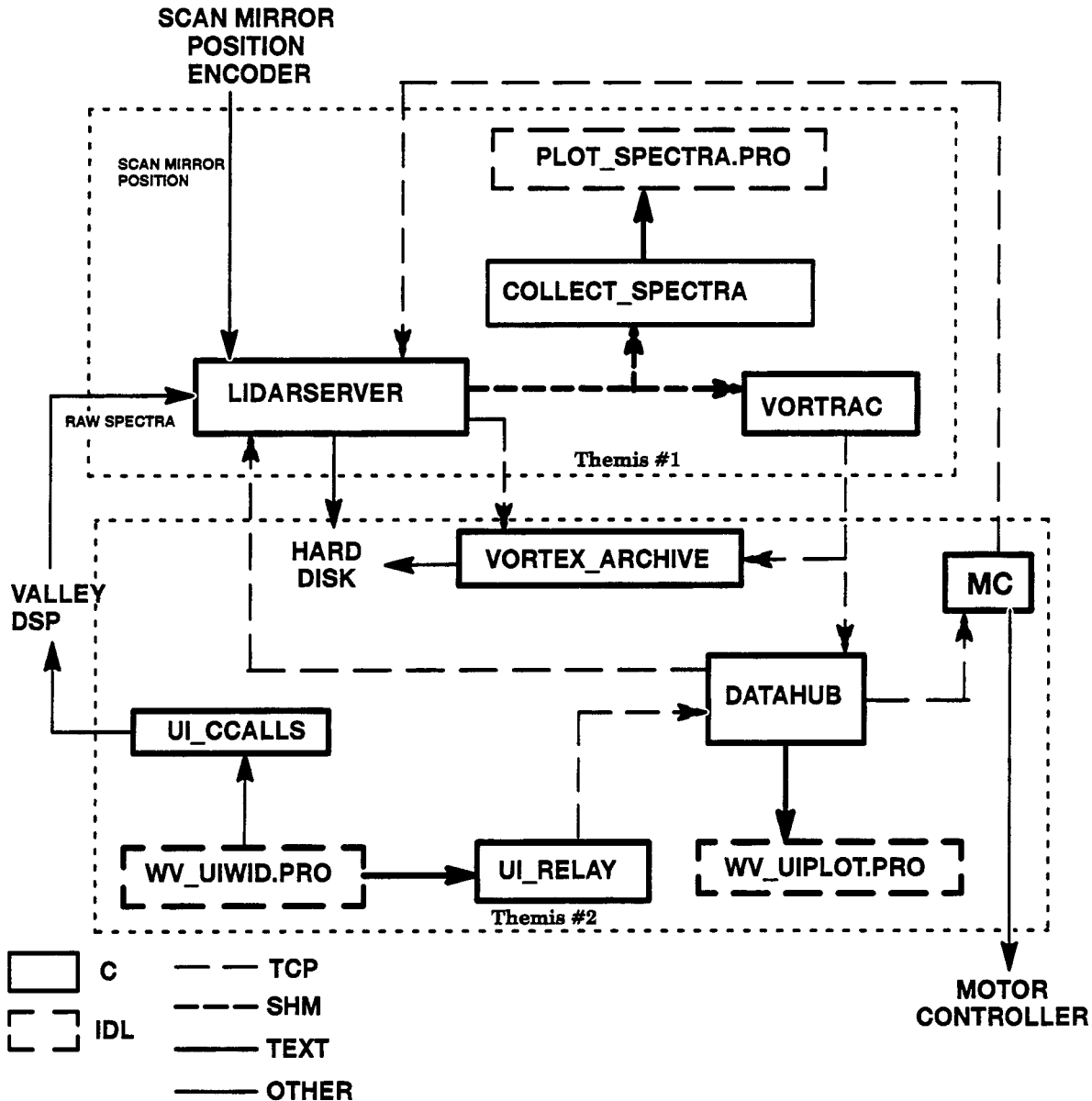


Figure 6. Lidar high-level software interconnectivity diagram.

where  $f_{BW}$  is the effective system bandwidth (20.0 MHz),  $\lambda$  is the wavelength (10.6  $\mu\text{m}$ ),  $P_{fl}$  is the polarity of the frequency lock between the master and local oscillators, and  $K_{zd}$  is the zero Doppler frequency bin. The zero Doppler frequency bin  $K_{zd}$  is found as the maximum bin of a histogram of spectrum peak locations for all peaks for all spectra in the current scan. This is a very reliable indicator since an omnipresent spectrum peak at zero Doppler is anticipated, due primarily to backscatter from stationary system optics.

The noise floor ( $N$ ) is computed each time the operator presses "SAVE" on the Graphical User Interface (GUI), generally  $\sim 10$  seconds prior to aircraft passage. When this occurs, the mean and standard deviation of the first 30–100 spectra are computed for each spectral bin. The noise floor is chosen as the spectrum power level corresponding to a certain number (generally between 5 and 20)

of standard deviations above the mean for each bin. The noise floor for spectral bins between  $-10$  m/s and  $10$  m/s are linearly interpolated to prevent noise floor contamination with real wind measurements. Spectra whose total power deviates more than 50 percent from the median power level of the  $m$  spectra are not used in computing the noise floor.

The ambient wind bin ( $C_i$ ) is found as

$$C_i = \text{nearest integer to } CW_{\text{COMP}}(Z_i) * \cos(\theta_i) \quad (3)$$

where  $\theta_i$  is the scan mirror angle corresponding to spectrum  $i$  and  $CW_{\text{COMP}}(Z_i)$  is the composite crosswind value at the approximate altitude of the focus point of the lidar ( $ZF_i = F_i * \sin(\theta_i)$ ,  $F_i$  is the focus range). The crosswind value is found by interpolating between crosswind bins in the currently stored wind profile or as zero if no crosswind profile currently exists.

The series of maximum velocities ( $\Psi_k$ ) for the scan is then convolved with a filter ( $X_k$ ) which contains attributes representative of a theoretical vortex velocity distribution. The convolved output is not sensitive to small perturbations in this model waveform, so a filter of the form

$$\begin{aligned} X_k &= \delta / (k - c + 1), c \leq k \leq p \\ &= k / c, 0 \leq k < c \\ &= -X_{-k}, 0 > k \geq -p \end{aligned} \quad (4)$$

where  $\delta = 1$  for scans whose direction is toward increasing scan mirror angles, or  $\delta = -1$  for scans which move toward decreasing angles over time. The parameters  $c$  and  $p$  are determined for each scan based on the estimated cross-range resolution  $\zeta$ . The cross-range resolution  $\zeta$  is estimated as the mode of a histogram of absolute differences between the scan angles of adjacent samples during the scan multiplied by the focus range. Typically, the filter core radius is chosen as  $2.0$  m and the filter half-width is chosen as  $10$  m, so that

$$c = \text{nearest integer to } 2.0 / \zeta \quad (5)$$

and

$$p = \text{nearest integer to } 10.0 / \zeta. \quad (6)$$

The edges of the convolution are handled by shrinking the extent of  $X$  as we move closer to the edge.

The resulting convolution waveform  $\Lambda$  is analyzed for vortices. A driver side (denoted by the relative direction of the vortex with respect to the sides of the lidar truck) vortex is detected when  $\text{MAX}\{\Lambda_i, 1 \leq i \leq l\} > T_{\text{CONV}}$ , while a passenger side vortex is detected for  $\text{MIN}\{\Lambda_i, 1 \leq i \leq l\} < -T_{\text{CONV}}$ . The parameter  $T_{\text{CONV}}$  is adjustable by the operator using the GUI. A driver side vortex corresponds to a port vortex and a passenger side vortex corresponds to a starboard vortex for aircraft arrivals, and the reverse is true for aircraft departures. The vortex angles ( $\Phi_p$  and  $\Phi_d$ ) are chosen as the scan angles of the maximum or minimum convolution indices.

Let  $0, 1, \dots, m-1, m$  describe the set of scan indices, prior to the scan being analyzed, for which there was a vortex detection, and  $\Lambda_k$  refer to the absolute convolution value at the detected vortex angle  $\Phi_k$  for scan  $k$ . The vortex range is found as

If  $(k \text{ where } \text{MAX}\{\Lambda_k\}) = (k \text{ where } \text{MEDIAN}\{F_k + \Delta F_k\})$

$$R_{m-1} = \sum_k \Lambda_k * (F_k + \Delta F_k) / \sum_k \Lambda_k$$

If  $(k \text{ where } \text{MAX}\{\Lambda_k\}) = (k \text{ where } \text{MAX}\{F_k + \Delta F_k\}), m-2 \leq k \leq m$

$$R_{m-1} = \text{MAX}\{F_k + \Delta F_k\}$$

If  $(k \text{ where } \text{MAX}\{\Lambda_k\}) = (k \text{ where } \text{MIN}\{F_k + \Delta F_k\}), m-2 \leq k \leq m$

$$R_{m-1} = \text{MIN}\{F_k + \Delta F_k\} \quad (7)$$

The  $\Delta F$  terms are found as the estimated vortex range rate ( $dR_k/dt$ ) multiplied by the time difference of the scan relative to the vortex detection time of scan  $m-1$ . The estimated vortex range rate is taken as  $CW(Z_k) * \cos(\Phi_k) - \sin(\Phi_k)$ . Note that this latter computation makes a rough assumption of a 1 m/s vortex descent rate. This range analysis is performed separately for both the driver and passenger vortices.

Finally, since the range estimate is made for the scan before the most recent, an extrapolated range estimate to the last scan is performed using the method described previously for determining  $\Delta F$ .

#### 2.1.3.3. Crosswind Profile Estimation

For scans where the vortex detection algorithm did not detect a vortex, ambient wind peak detections from each spectrum are used to estimate a vertical crosswind profile. This operation is performed in the *vortrac* software module. The ambient wind peak (VA) of a spectrum is determined as the largest spectrum peak which is at least  $N_{aw}$  standard deviations (typically 100) above the noise floor and is not the zero Doppler peak and which is in the interval  $[-15 \text{ m/s}, 15 \text{ m/s}]$ . If no such peak exists, the ambient wind is assumed to be zero.

A crosswind estimate is made every  $I_{cw}$  meters (typically 30), with the first estimate at  $I_{cw} / 2$  meters, and the last estimate over 300 m above the truck. The altitude bin of each spectrum is determined according to the altitude of the lidar focus when the spectrum was collected. The crosswind of each spectrum is determined by making a zero vertical wind assumption and making a trigonometric transformation of the spectrum ambient wind peak as

$$CW_{\text{SPECT}}(i) = VA_i / \cos(\theta_i). \quad (8)$$

Spectra collected with scan angles  $|\cos(\theta_i)| < 0.3$  or which have computed wind peaks at zero m/s are not used in computing the profile. The nearest bin in the vertical wind profile to each spectrum collection altitude is determined, and the set of crosswind estimates at each bin from the scan is averaged. The mean ( $CW_{\text{SCAN}}$ ), standard deviation, and number of data points ( $N_{\text{SCAN}}$ ) of the data points for each bin is also computed. This data is referred to as the *scan crosswind profile*.

A *composite crosswind profile* ( $CW_{\text{COMP}}$ ) is also determined based on a set of recent *scan crosswind profiles*. At most, the last 20 *scan crosswind profiles* are used. The *composite crosswind profile* is made by combining the *scan crosswind profiles* with both a population and age weighting. The *composite crosswind profile* at each altitude bin is estimated as

$$CW_{COMP} = \sum_k \alpha_k * N_{SCAN}(k) * CW_{SCAN}(k) / \sum_k \alpha_k * N_{SCAN}(k), 1 \leq k \leq 20 \quad (9)$$

where the aging coefficient  $\alpha_k$  is determined as

$$\alpha_k = \text{MAX} \{ 1 - T_k / \tau_{AW}, 0 \}, \quad (10)$$

$T_k$  is the age of the  $k$ th scan relative to the most recent scan, and  $\tau_{AW}$  is an aging time constant (typically two minutes).

#### 2.1.3.4. Data Archive

Various levels of data generated by the real-time lidar system are archived for later processing. The labeled power spectra are saved to disk in a time-stamped file name only when the operator has selected the "SAVE" feature of the GUI, which is generally any time a vortex is being measured. This data also includes records which identify the end of a scan. This task is performed by the *lidarServer* software module. Spectrum maximum velocities, ambient wind peak locations, zero Doppler peak locations, scan mirror, focus and declination positions and times are saved by the *vortex\_archive* software module, packaged as one record for each scan. The *vortex\_archive* module also stores records when new spectrum files are being saved, records chronologicalizing the *scan crosswind profiles* and the *composite crosswind profiles*, and vortex position and motion information.

#### 2.1.3.5. Scan Selection

The lidar system is an entirely closed-loop system. Only after the last scan has been analyzed for vortices does the lidar system determine the parameters of the next scan. This process is referred to in this document as *scan selection*, and occurs in the *datahub* software processing module. There are currently only three possible scanning modes: *wind profile update*, *vortex acquisition*, and *vortex tracking*. *Wind profile update* scanning follows a preprogrammed sequence of scan angles and focus ranges, is invoked by the lidar operator pushing the "UPDATE WIND" button on the GUI, and will continue through the complete scan sequence (currently six scans from 40 to 300 m focus range, 0.15 to 3.0 rad scan angle) unless interrupted by operator selection of the GUI "SAVE" button when tracking is turned on. Note that the wind profile is updated whenever a vortex is not detected, regardless of whether the lidar is in the *wind profile update* mode. This mode simply ensures that the full range of altitudes is visited by the lidar. *Vortex acquisition scanning* is used any time *wind profile update* scanning has not been selected, and either vortex tracking has not been turned on, spectra are not being saved, or a vortex has not been detected since spectra have been saved. It follows a periodic scanning sequence through a set of scans at several different focus ranges between a fixed set of scan angles. The *acquisition scanning mode* attributes are selectable by the GUI. *Vortex tracking mode* is initiated the first time a vortex is detected after the GUI has been configured so that tracking is turned on and spectra are being saved. The lidar returns to *acquisition scanning mode* as soon as spectrum saving is turned off. These scanning modes and the scenarios which invoke them are summarized in Table 1.

**Table 1**  
**Scan Mode Control Table \***

"WIND UPDATE" PUSHED	"SAVE" PUSHED	TRACKING ON	VORTEX DETECTED	RESULTING SCAN MODE
F	F	F	F	ACQUISITION
F	F	F	T	ACQUISITION
F	F	T	F	ACQUISITION
F	F	T	T	ACQUISITION
F	T	F	F	ACQUISITION
F	T	F	T	ACQUISITION
F	T	T	F	ACQUISITION
F	T	T	T	VORTEX TRACKING
T	F	F	F	WIND UPDATE
T	F	F	T	WIND UPDATE
T	F	T	F	WIND UPDATE
T	F	T	T	WIND UPDATE
T	T	F	F	WIND UPDATE
T	T	F	T	WIND UPDATE
T	T	T	F	ACQUISITION
T	T	T	T	VORTEX TRACKING

\* The notation T indicates that the condition at the top of the column is true, while F indicates false.

Once *vortex tracking mode* has been initiated, separate routines determine the scan mirror angles and the focus range for the next scan. The focus range for scan  $k+1$  is determined first since that range is used in determining how far in angle outside the vortex needs to be scanned. For single vortex tracking, the vortex ranges and lidar focus ranges are compared for the last two scans to determine whether the vortex has been bracketed by the last two scans. The term *bracketing*, as used here, refers to one of the last two scans focused farther away than the vortex range, while the other scan was focused closer than the estimated vortex range. If this is the case, the next lidar focus range,  $F_{k+1}$ , is chosen to be the extrapolated vortex range at the next scan time ( $R_{k+1}$ ). Otherwise, the next scan is chosen with the hope of bracketing the vortex for the next range estimation. This can be expressed formally as

$$\begin{aligned}
 F_{k+1} &= R_{k+1} \text{ if } (F_k - R_k) * (F_{k-1} - R_{k-1}) < 0 \\
 &= R_{k+1} - F_{\text{slack}} \text{ if } (F_k - R_k) \geq 0 \text{ and } (F_{k-1} - R_{k-1}) \geq 0 \\
 &= R_{k+1} + F_{\text{slack}} \text{ if } (F_k - R_k) < 0 \text{ and } (F_{k-1} - R_{k-1}) < 0,
 \end{aligned} \tag{11}$$

where  $F_{\text{slack}}$  is a user defined constant. If the system is in the tracking mode to follow both vortices, candidate focus ranges are determined separately for each vortex, using the above analysis. If both

vortices are bracketed by recent observations, the average of the candidate focus ranges is selected for the next scan. If either vortex is bracketed but the other is not, the candidate focus range of the other vortex is selected. Otherwise, if neither vortex is bracketed, a simple analysis is performed to see whether both vortices were lost in the same range direction (i.e., both vortices are too far away relative to the recent focus ranges). If so, the largest candidate move in the proper direction is chosen. If the vortices were lost in different directions, the candidate range the farthest away from recent focus ranges is selected. The scan select algorithm automatically switches to single vortex tracking mode if the last estimated vortex ranges for the two vortices are more than  $\Delta R_{MAX}$  apart. In this instance, the vortex at the closer range is chosen. In both the single- and multiple-vortex tracking modes, the constraints  $F_{k+1} > F_{min}$  and  $F_{k+1} < F_{max}$  are imposed (typically  $F_{min} = 30$  m and  $F_{max} = 300$  m).

The scan angles for single vortex tracking are found as

$$\begin{aligned}\theta_{min} &= \Phi_{p,d} - \zeta_{slack} / F_{k+1} \\ \theta_{max} &= \Phi_{p,d} + \zeta_{slack} / F_{k+1}\end{aligned}\tag{12}$$

where  $\Phi_{p,d}$  refers to the detected vortex angle for the tracked vortex and  $\zeta_{slack}$  can be adjusted by the operator through the user interface. If no vortex was detected last sweep, then the scan angle limits for the last sweep are used. The scan angles for multiple vortex tracking are

$$\theta_{min} = \text{MIN}\{ \Phi_p, \Phi_d \} - \zeta_{slack} / F_{k+1}\tag{13}$$

$$\theta_{max} = \text{MAX}\{ \Phi_p, \Phi_d \} + \zeta_{slack} / F_{k+1}.\tag{14}$$

For both single- and multiple-vortex tracking, the constraints  $\theta_{min} \geq 0$ ,  $\theta_{max} \leq \pi$ , and  $\theta_{max} - \theta_{min} \geq \Delta\theta_{MAX}$  are imposed. Additionally, any time multiple tracking is selected and the vortices are detected more than  $\Delta\Phi_{MAX}$ , the algorithm automatically reverts to single-vortex tracking mode, where the vortex selected to track is the vortex at the closest range.

#### 2.1.3.6. Motor Control Interface

The lidar workstations communicate with the motor controller through a serial port. The motor control interface acts to communicate motor movement function calls to the motor controller and read and parse text messages made by the motor controller. These functions are contained in the *mc* software module. This module also communicates the focus and declination positions to the *lidar-Server* process after parsing these positions out of the motor controller text output. The motor controller is programmed to accept function calls of scan mirror motion at a constant focus range or focus range movement at a constant scan angle. Parameters indicating absolute or relative scan angle and focus range positions and scan speed are determined by the *datahub* software module and passed to the motor controller by the *mc* process.

#### 2.1.3.7. Data Display

The lidar operator has the option of generating several types of real-time data displays. The *plot\_spectra.pro* software module plots a real-time display of labeled power spectra as a color-coded amplitude display. An example of the spectra plots (shown as a gray scale image) presented to



the operators is shown in Figure 7. Each spectrum is a line of color-coded pixels oriented vertically. Vertical lines which are entirely black are intended to indicate the end of a scan. The color scale is linear, so that the large wind and zero Doppler peaks are usually shown in white, indicating that the amplitudes of these areas of the signal have saturated the color scale. The ranges of the color scale have been chosen for the easiest discrimination of vortices.

Running displays of the composite crosswind profiles, vortex range, angle, and 5–15 m average circulation are also optionally available to the operator. Vortex range, angle and circulation plots are reset each time a new spectrum file is saved. These plots are generated by the *wv\_uipilot.pro* software module.

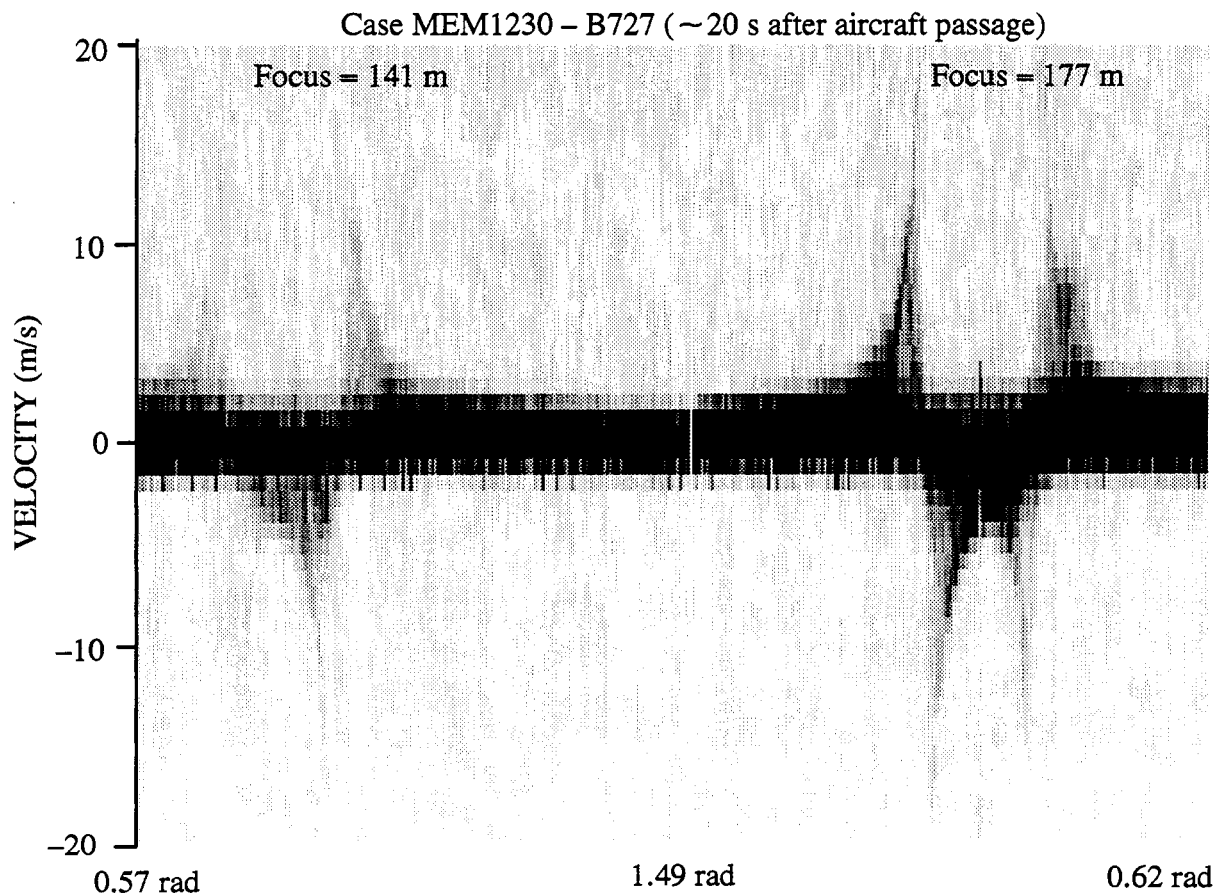


Figure 7. Sample color-coded spectrum display.

#### 2.1.3.8. Graphical User Interface (GUI)

The lidar operator has the ability to select a range of processing parameters through a graphical user interface (GUI). The GUI is shown in Figure 8. When not actively scanning the laser, the operator could adjust the number of averages and number of frequency samples ( $n$ ) used in constructing the Doppler spectra received by the workstation. The operator could also set the acquisition mode scanning parameters, including the number of scans, range of angles and ranges, and scan mirror velocity of the scan pattern. Several plotting options could be selectively toggled. Tracking criteria indicating which vortex to track, the tracking scan mirror velocity, the angle and range slacks, and

the detection convolution threshold ( $T_{CONV}$ ) could be set. The tracking could also optionally be tuned for specialized scanning purposes. The "SAVE" button not only invokes archiving of the spectral data to disk but also activates vortex tracking. This was the button used to indicate to the system that an aircraft was about to fly over the truck. The "UPDATE WIND" button could be used to initiate a scanning mode which ensured that all altitudes from the surface to 300 m were visited by the lidar scanning. This was generally used to update the wind profile in between tracking vortices. The "START SCAN" and "STOP SCAN" buttons initiate or deactivate movement of the motors for lidar scanning. The "NOT COMPUTE" button is useful in instructing the algorithms to ignore the current spectra being ingested by the workstations. The primary reason for this button is to prevent corrupted data from being inserted into the wind profiles or archived data files which were collected during active adjustment of lidar system optics or electronics.

### Wake Vortex Lidar User Interface (MIT/LI)

#### COLLECTION

# Spectrum Averages

# Spectrum Pts

Scan Mirror Acquisition Velocity (degrees/s)

ANALYSIS PLOTS

☐ Vortex Position

☐ Vortex Circulation

☐ Crosswind Profile

Track ☒ IRIV ☒ PASS ☒ BOTH

Scan Mirror Tracking Velocity (degrees/s)

Conv. thresh

Track angle slack

Track range slack

Tracking ☒ OFF ☒ ON

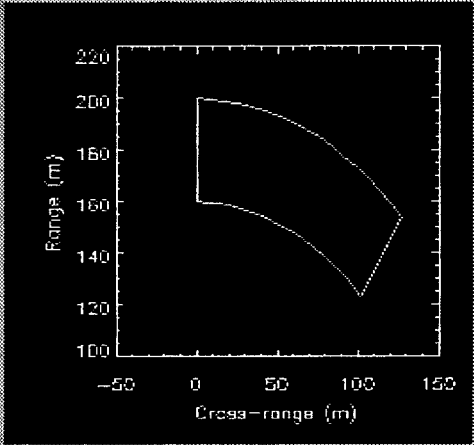
Acquisition

Start range  Stop Range

Start Angle  Stop Angle

# of sweeps  Declination Angle

View looking toward airport runway



☒ NOT SAVE   ☒ SAVE      ☒ NOT COMPUTE   ☒ COMPUTE

STATUS

Figure 8. Lidar software graphical user interface (GUI).

## 2.1.4. Alignment and Calibration Procedures

### 2.1.4.1. Primary Optical Bench Alignment

The primary optical bench alignment is performed only after major relocations of the lidar or after the system has been dismantled for upgrade. This alignment procedure involves the correct positioning of the off-axis parabolic primary mirror and the variable focus translation stage. The basic procedure is to use a Twyman–Green interferometer to locate the optical axis of the parabolic mirror and position the variable focus stage parallel to this axis with the use of a tilt-sensitive interferometer. For this process, 632 nm radiation from HeNe lasers are used, and then the final alignment is transferred over to the 10.6 micron CO<sub>2</sub> beam.

As part of this alignment process, the focal range calibration and lidar response function calibration are performed. The distance from the parabolic mirror at which the transmitted lidar beam comes to a focus is controlled by moving the focusing optics which are mounted on a translation stage. The first step in the focal range calibration is to generate predictions of the focal distance from the parabolic mirror versus focusing lens position using a ray-tracing computer code. These predictions were then fit to an equation of the form:

$$\text{focus} = A/(B - x) + C, \quad (15)$$

where A, B, and C are fit parameters and x is the relative position of the focusing lens. The actual focal range is then measured by moving the focus lens assembly to various positions and then physically measuring the location of the laser focus from the truck and adding the extra distance to the parabola. These data were then used to determine the offset parameter, B, in the above equation, keeping the theoretical fit values for A and C. The value of the B parameter, so obtained, varied by 6.7 percent from the first 11/94 Memphis fielding to the second 8/95 fielding.

The lidar response function was measured during the 8/95 Memphis fielding at a range of 70 m from the lidar by measuring the system response to a fixed target. Even though the target was fixed, the backscattered signal was significantly greater than the normal zero-Doppler signal from the system optics. Optical attenuation was required in front of the detector to ensure that the detector output was linear and that the amplified detector signal did not saturate the analog-to-digital-converter. The peak zero-Doppler signal was then measured for an averaged waveform as a function of the laser focus location. The difference in focal distances between the half-maximum peak signals was then taken as the width of the lidar range response function at 70 m. This value was within experimental error of the theoretical value of 2.73 m.

### 2.1.4.2. Daily Optical Alignment

The daily adjustment of the lidar alignment included “tweaking” the optical components and verifying the position of the focusing optics and scan mirror. Tweaking the optical component involves verifying that the CO<sub>2</sub> beam is going through the optical axis of the variable focus system and that it is centered on the parabolic mirror, as well as checking that the backscattered beam and the local oscillator beams each are centered on the detector. The final optical adjustment tweaks the backscattered beam on the detector to optimize the signal from the ambient wind.

The daily focus lens and scan mirror calibrations are performed automatically by having the computer system do a fine position search for fixed hardware markers in both systems. These markers define very precise locations for the scan mirror angle and translation stage position and are accu-

rate to within 0.04 degrees and 10 microns, respectively. Early testing demonstrated that the laser focal location was reasonably constant with respect to focusing optics position, so the external focus location is typically not checked on a daily basis. The marker position on the scan mirror is set to the vertical position relative to the roof of the truck, with an accuracy of about  $\pm 1$  degree. This would represent a systematic angle offset that would be common to all the data over a given push (after which the scan mirror is removed from its housing for shipping). The main source of error in the scan angle, however, is related to the repeatability of the leveling of the lidar truck after each change in location around the airport. This leveling is performed by centering level indicators near the rear corners of the truck, and the error associated with this process is estimated to be about  $\pm 3$  degrees. This error would be common to all data collected during the time that the lidar truck was positioned in one location and would vary once the lidar truck was relocated.

#### 2.1.4.3. Operation in Low Visibility and Rain

Table 2 shows the theoretically calculated power signal-to-noise for the lidar return from a vortex at a range of 300 m for various atmospheric conditions. The lidar should have no difficulty in operating in moderate fog (500 m visibility) since the increase in backscatter more than overcomes the increased attenuation. The lowest signal returns in the table are for the 25 mm/hr rain conditions. This represents fairly heavy rain, in which case, unlike the fog, the increased scattering from the rain is not assumed to contribute to the backscattered signal but only to the attenuation. This is because most of the larger raindrops cannot be assumed to have reached the full velocity of the vortex during the time which they fall through. The effect of the rain, therefore, will be to reduce the signal through attenuation and to add another feature to the measured spectra at lower velocities. Nevertheless, rain at this level should not pose a problem for lidar operation from return signal considerations.

**Table 2**  
**Theoretically Calculated Power Signal-to-Noise for the Lidar Return**  
**from a Vortex at 300 m Range for Various Atmospheric Conditions**

ATMOSPHERIC MODEL	$\kappa(\text{km}^{-1})$	$\beta_{\pi}(\text{m}^{-1}\text{sr}^{-1}) (\times 10^{-8})$	(S/N) <sub>p</sub> (dB)
Urban Aerosol	0.21	2.1	17
Haze (98% relative humidity)	0.61	4.1	19
25 mm/hr Rain	2.85	4.1	13
Moderate Fog (500m Vis.)	1.96	62.9	27

There are operational considerations to lidar data collection in rain, however. The lidar cannot operate in conditions where the scan mirror is actively being covered with raindrops. In order to avoid this, the scan mirror can be tilted forward to move the lidar beam down as much as 45 degrees. A cover is then placed directly over the scan mirror which shields it from rain falling directly down and from behind. The scan mirror can then continue to direct the lidar beam towards the vortex and collect data. The limitations on this are that the rain cannot be falling from in front of the cover, a condition normally fulfilled if the planes are landing upwind and the lidar truck is positioned to face the direction of aircraft motion, and the wind cannot be gusting in different directions too heavily to blow water onto the scan mirror, anyway. With the scan mirror tilted down, the beam scanning profile will define a cone with a 45-degree half angle and axis parallel to the ground. Measurements

during both the 12/94 and 8/95 deployments in Memphis were in very dry conditions, and to date the lidar has not been operated in moderate to heavy rain conditions.

#### 2.1.4.4. System Sensitivity to Vibration

When the lidar is operating the lasers and all the optics, except for a fixed turning flat and the scan mirror, are all connected to a floated four-foot by six-foot optical bench. This achieves a great deal of vibration isolation, so data can be collected even when aircraft are passing close overhead. Since the variable focus stage is also located on the optical bench, however, vibrations caused by changing the lidar focus are not as well isolated and the lidar performance degrades when the focus is being varied. For this reason, data is typically not collected during the period that the focus is varied and for a 0.25 second settling period afterward. The scan sequence thus consists of scanning the lidar beam in angle across a vortex, moving the focus position, and then scanning the beam back across the vortex. As it turns out, this is the optimum scanning strategy for determining the vortex strength.

#### 2.1.4.5. Accuracy of Spectrum Time and Scan Angle Labels

The process by which data is collected by the lidar involves first collecting enough data points with the analog-to-digital converter to calculate the number of spectra to average, then the spectra themselves are calculated by performing FFT calculations on the data, after which the power spectra are calculated and averaged. Following this, the computer checks the scan angle from the encoder and the system time for the scan angle labels and spectrum times, respectively. With the data collection parameters used for the 8/95 Memphis fielding, the latency between the beginning of data collection and the time and angle stamping of the spectra was typically less than 2 ms. This means that the time stamp precision was less than 2 ms and, assuming an average scan rate of 60 degrees/second, the scan angle label precision was less than 0.12 degrees. The time stamp accuracy, as defined relative to the aircraft passage, was dominated by the total system time uncertainty with respect to aircraft passage, which was on the order of two seconds. Correspondingly, the scan angle accuracy was dominated by the absolute truck position angle as discussed earlier.

#### 2.1.4.6. Wind Profile minimum measurable Wind Velocity

If the position of the wind signal peak is used, then the minimum measurable ambient wind velocity would be limited by the half-width of the zero-Doppler peak. This has been measured to have an average value of 0.94 spectral bins which, for the 8/95 Memphis fielding parameters, corresponds to 0.75 m/s.

## **2.2. Vortex Data Processing**

### **2.2.1. Vortex Position Estimation**

The vortex angle is found using the real-time technique discussed in section 2.1.3.2. Each angle is verified and, if necessary, corrected by manual examination of the maximum velocities for each lidar scan. This is done to ensure the best possible data for distribution. Improvements in the angle localization routines to reduce the number of missed or false detections will reduce the need for this manual intervention. An example of the results of manual angle editing is shown in Figure 9.

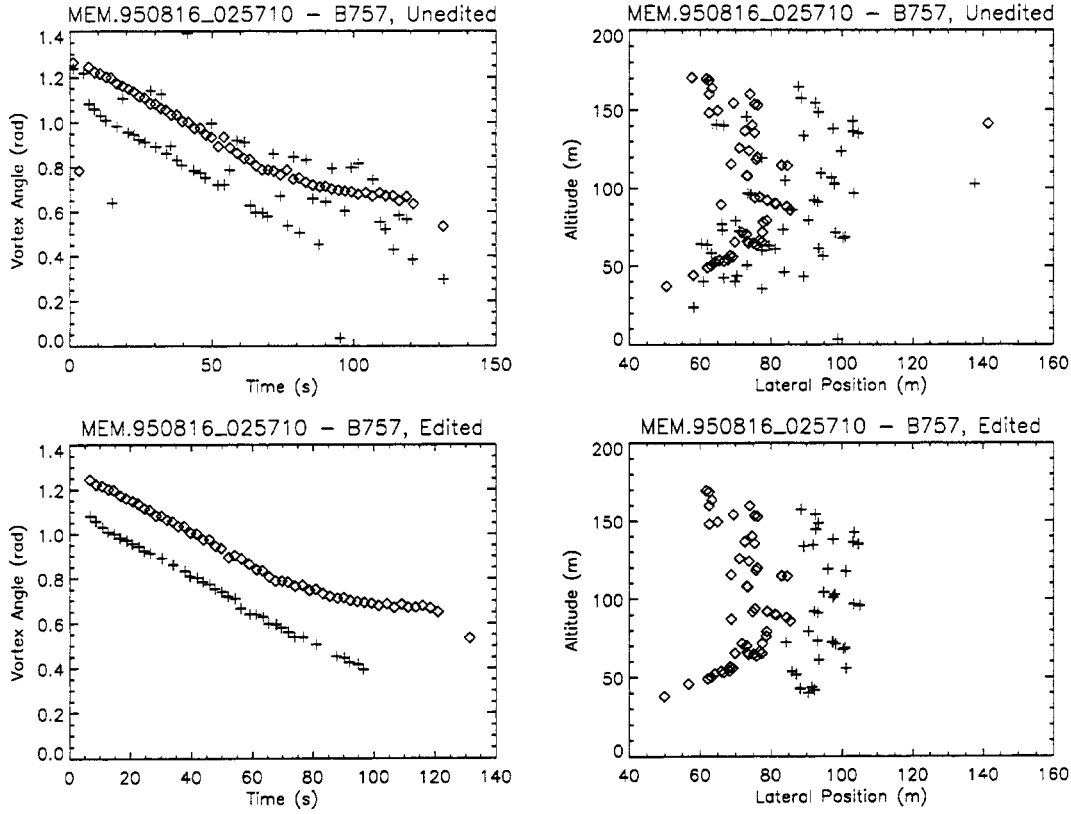


Figure 9. Effect of manual angle editing on detected vortex angles and resulting tracks for MEM case 1252.

Vortex ranges are computed differently than in real-time, using the technique developed by Salamitou (Salamitou, et al., 1995; Salamitou, et al., 1997). This technique uses much more information from each spectrum in the range estimation. Basically, the integrated spectral amplitudes across a set of angles centered on a vortex are shown analytically to follow a cubic relationship to the Doppler velocity being integrated, for a line vortex whose tangential velocity drops off as  $1/r$  outside the core. The range estimation technique integrates across the angle for several spectral velocity bins which are not just noise and are not in the vortex core. It further integrates these sums by cubically weighting them by their Doppler velocity. These weighted sums across angle and velocity are weighted and are analyzed at three successive focus ranges. These sums are analytically related to the circulation strength of the vortex. A cost function is minimized for the vortex range and range rate. This cost function minimizes the interscan difference in the angle/velocity spectrum sums, weighted by the lidar range response function (a function of vortex range, vortex range rate, and focus range). Model studies have shown improved accuracy and resistance to artifact over the real-time method described in section 2.1.3.2. Future data collections will use this technique (Salamitou, 1995; Salamitou, 1997).

Vortex angle error is very small when compared to possible estimation error due to vortex range. The angle estimation error is scaled to the range  $[0.0, 0.01]$  radians based on the maximum absolute convolution value ( $\Lambda$ ) found in the angle estimation procedure. The range estimation is taken as the half-width of the minimum of the cost function  $J$ . These range and angle errors are converted to Car-

tesian space and are entered in the distributed data files. The angle error is heuristically accurate in an absolute sense, but the range error is only a relative error metric. It is best to use these numbers as a relative measure of position estimation accuracy when comparing two sets of measurements, or when comparing portions of a vortex track. Whenever examining data and trying to understand the trustworthiness of the measurements, there are many factors which may be important. Some of the heuristics which may be commonly applied are:

1. Angle estimation has difficulty detecting two vortices which are at or near the same angle.
2. Range estimation assumes constant circulation over the last three detected scans.
3. Range estimation is easier when the last three detected scans have "focal diversity." In general, if the three scans are the same distance from the vortex each time, they provide redundant information and result in inaccurate range estimates. It is important that the three focus ranges be at relatively different ranges from the vortex since the range estimation relies on different responses as a function of range from the vortex.
4. Range estimate may be affected by the influence of a neighboring vortex. Range estimation involves integrating velocity spectra across a set of angles. As in circulation estimation, the vortex range estimate can be affected by the influences of the neighboring vortex on the velocity spectrum. Vortex position estimations from modeled data showed that this generally tends to bias the range estimates of the two vortices toward one another. This dependance has not been confirmed with actual data when range estimation sensitivity to the extent of angular integration is examined.
5. Range estimate can be biased by the focus ranges chosen by the tracking algorithm. The ability of the range estimation algorithm to extrapolate beyond the set of focus ranges at which measurements are taken is a function the focal diversity just discussed, as well as the distance of extrapolation necessary. When conditions are not appropriate for extrapolation, the range estimate can be biased by the focus ranges that were chosen by the tracking algorithm.
6. The first few range estimates for a vortex tend to be the most variable.
7. Range estimation accuracy is a function of the range gate size at the focus ranges. That is, range estimates far away should be less accurate than ranges estimates at closer range gates.

These are guidelines for understanding the data, and in some cases are the result of heuristics generated by the conformity of the data to our expectations of vortex behavior. In other cases, particularly in some of the range estimation influences, the trends have been noted in simulations of the lidar data with the post-processing vortex location algorithm.

### **2.2.2. Circulation Definition and Basic Calculation**

The circulation,  $\Gamma$ , of a rotational flow is given by the line integral of the flow velocity about a closed contour encompassing the center of the flow:

$$\Gamma = \oint \vec{V} \cdot d\vec{l} \quad (16)$$



Since coherent lidar systems measure only the line-of-sight (LOS) vortex velocity, calculation of a circulation requires the assumption that the flow of a vortex is circularly symmetric (Figure 10). Under these circumstances, the circulation within a circular contour of radius  $r$ , oriented about the center of a vortex, is given by  $2\pi r V_{\text{los}}(r)$ . If the tangential velocity of wake vortices is further assumed to decrease as  $1/r$  outside some central core region and the vortex axis of rotation is perpendicular to the lidar beam, then the circulation becomes constant in radius. The circulation can therefore be approximated as an average over the  $r$ -weighted LOS velocity outside the central core of a vortex:

$$\Gamma \approx \frac{2\pi}{N} \sum_{i=1}^N r_i V_i \quad (17)$$

where the  $V_i$  are individual tangential velocity measurements along the LOS of the lidar at corresponding radial distances,  $r_i$ , from the vortex center. The sum in equation (17) is typically defined over a radius region whose minimum exceeds the radius of the core (where the core is functionally defined as the region where the tangential velocity versus radius significantly departs from a  $1/r$  behavior) and whose maximum radius is limited by the minimum velocity which can be measured and attributed to the vortex flow. Equation (17) defines the basis by which all the circulations presented in this memo have been calculated.

The next step in estimating the circulation is to consider the relationship between the vortex LOS tangential velocity and the lidar generated velocity spectra. These spectra can be thought of as the histogram of the LOS velocity profile, weighted by the lidar range response function. For a uniform lidar response function, it can be shown theoretically (Constant, et al., 1994; Salamitou, et al., 1997) that the spectral amplitude per unit velocity interval diverges for backscatter from the region where the lidar beam is tangent to the vortex flow. This means that there will always be a peak in the lidar spectrum corresponding the tangential LOS velocity, and theoretically, the high velocity side of the peak will have infinite slope and terminate at the tangential velocity. Even with a nonuniform lidar range response function, the lidar spectrum will diverge at the LOS vortex tangential velocity. However, if the lidar focus is far from the vortex, then the area under the peak will diminish and eventually the peak will be lost in the noise. A plot of a theoretically generated spectra is shown in Figure 11. For this case, lidar parameters corresponding to the actual lidar system were assumed, with the theoretical vortex 100 m from the lidar and the lidar focus at the same range. As can be seen from the figure, there is a well defined peak at the LOS vortex tangential velocity. If the simulation had infinite velocity resolution, then the amplitude of the peak would go to infinity, although the integral under the peak would still be finite. It can be seen, therefore, that the position of the maximum spectral signal is representative of the tangential velocity and the circulation should be calculated from it.

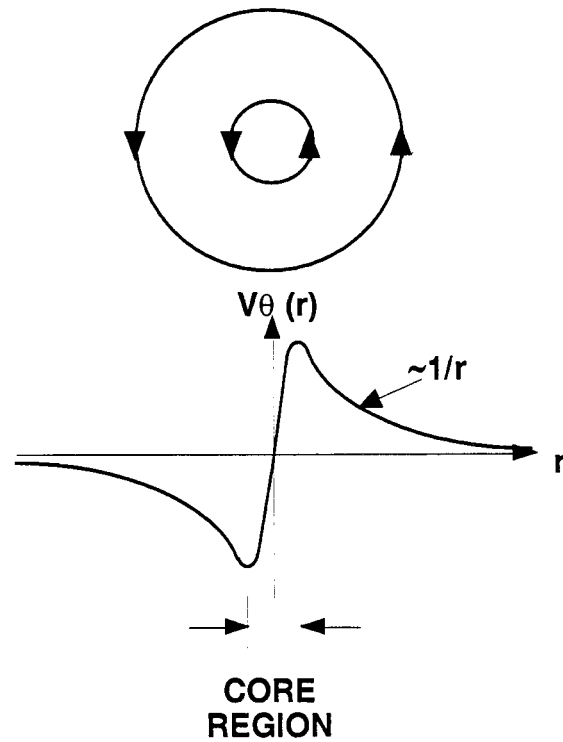


Figure 10. Assumed circularly symmetric flow field of a wake vortex, showing the radial dependence of the tangential velocity. Outside of a central core region, this velocity decreases as  $1/r$ , where  $r$  is the radial distance from the center of the vortex.

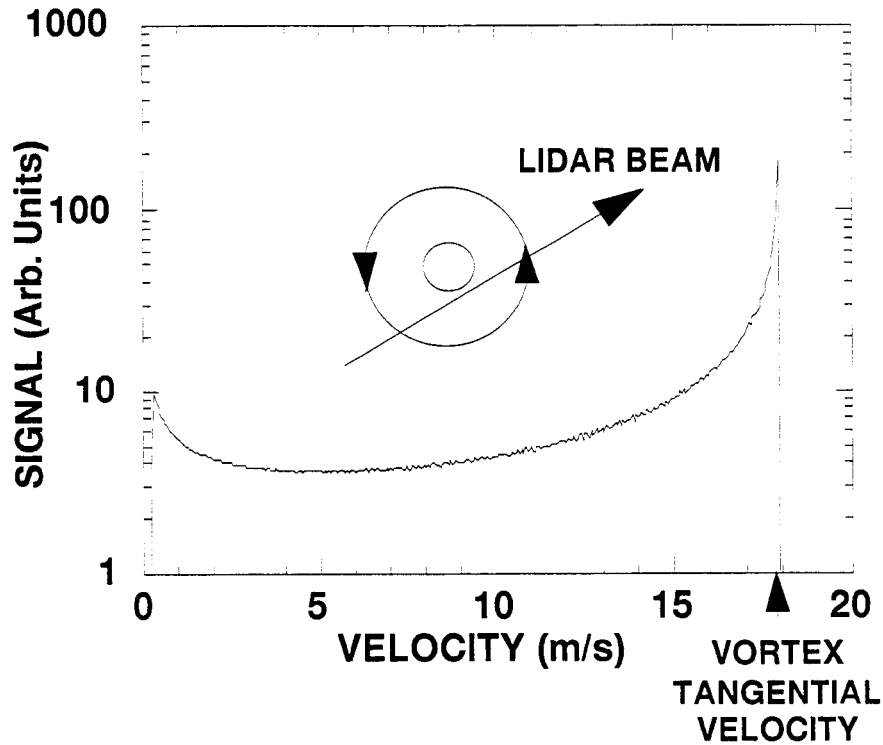


Figure 11. Theoretical spectra corresponding to a lidar beam focused on a vortex, with the beam passing 7 m from the center of the vortex. The maximum velocity in the spectra corresponds to the LOS velocity where the lidar beam is tangent to the vortex.

One test that can be applied to the circulation results is to compare the initial vortex circulations with a simple model. According to this, the newly generated vortex circulation, before it has had a chance to decay but after the vortex is fully formed, should be given by:

$$\Gamma_0 = \frac{4g}{\pi} \frac{W}{\rho V_{TAS} b} \quad (18)$$

where  $W$  is the aircraft weight,  $\rho$  is the ambient air density,  $V_{TAS}$  is the airspeed of the aircraft, and  $b$  is the wingspan. The factor of  $4/\pi$  comes from the approximation of elliptical loading along the wings. The initial circulation values from equation (18) have agreed reasonably well with previous vortex measurements (Page, et al., 1991; Hannon and Thomson, 1994). The results of equation (18), suitably modified to take into consideration the effect of the velocity field of the neighboring vortex as discussed below, will be compared with circulation calculations.

#### 2.2.2.1. Effect of Neighboring Vortex on Circulation Estimation

When determining the vortex circulation from the lidar measured LOS velocities, the effect of the ambient wind must be considered. Both of the generated vortices will move with the ambient wind, so any measured LOS velocity will actually be the sum of the LOS vortex velocity and the LOS ambient wind velocity. If the ambient wind field is uniform, then its effect can approximately be ignored if vortex tangential velocity measurements are made at equal distances on either side of the vortex core and the corresponding circulations are averaged together according to equation (17). This is because the LOS contribution of the ambient wind will add to the vortex velocity on one side of the core and subtract from the vortex velocity on the other side of the core. Upon summing the contributions from both sides, the ambient wind contribution cancels.

Another similar contribution to the vortex tangential velocity comes from the counter-rotating neighboring vortex. In this case, the LOS vortex velocity is the sum of the vortex tangential velocity and the velocity from the opposite-sign neighbor vortex. Unlike the ambient wind case, however, the velocity field from the neighboring vortex is not uniform, going as  $1/r$ , and its contribution to the LOS velocity is a strong function of the vortex pair separation and the relative angle the lidar beam makes with the line joining the centers of the two vortices. Added complications can develop in instances where one vortex is stronger than the other. This effect is too variable to correct for under arbitrary conditions. However, by looking at a couple of simple cases, an understanding of the magnitude and nature of the contribution can be gleaned. To this end, an analytical expression is first derived for the relative change in the estimated circulation due to the neighboring vortex in the case where the lidar is looking vertically upward at the vortex pair (i.e., the lidar beam is perpendicular to the line connecting the center of the vortices), assuming that the vortices are of equal strength. A numerical calculation is then performed for the more general case where the lidar looks at an arbitrary angle relative to the vortex pair orientation, again assuming that the vortex strengths are equal.

#### 2.2.2.2. Analytical Solution for Lidar Looking Vertically at Vortices

The tangential velocity outside the central core of a vortex in the presence of the counter-rotating neighboring vortex along the line joining the two vortices can be approximated as (see Figure 12):

$$V(r) = \frac{\Gamma}{2\pi r} + \frac{\Gamma}{2\pi(r_s - r)} \quad (19)$$

where the  $r = 0$  origin is located at the core of the left or port (looking in the direction of the aircraft motion) vortex,  $\Gamma$  is the actual circulation of both vortices, and  $r_s$  is the separation between the vortices. The circulation can be estimated from averaging the product of the tangential velocity and the corresponding radius over some range of radii:

$$\Gamma \approx \langle \Gamma \rangle = \frac{1}{2(r_b - r_a)} \int_{r \leq |r| \leq r_b} 2\pi r V(r) dr \quad (20)$$

where  $r_a$  and  $r_b$  are the minimum and maximum of the radius range over which to average the circulation, and the factor of 2 in the denominator comes from the fact that the average is over positive and negative  $r$ . Written out explicitly, the integral is of the form:

$$\langle \Gamma \rangle = \frac{\Gamma}{2(r_b - r_a)} \left[ \int_{r_a}^{r_b} \left( \frac{1}{r} + \frac{1}{r_s - r} \right) r dr + \int_{r_a}^{r_b} \left( \frac{1}{r} - \frac{1}{r_s + r} \right) r dr \right] \quad (21)$$

where the two terms in the brackets are the circulation contributions from the  $r > 0$  and  $r < 0$  regions, respectively. Equation (21) can be evaluated to give:

$$\frac{\langle \Gamma \rangle}{\Gamma} = \frac{1}{2\left(\frac{r_b}{r_s} - \frac{r_a}{r_s}\right)} \ln \left[ \frac{1 + \frac{r_b}{r_s}}{1 - \frac{r_b}{r_s}} \cdot \frac{1 - \frac{r_a}{r_s}}{1 + \frac{r_a}{r_s}} \right] \quad (22)$$

where the estimated circulation has been normalized by the actual circulation of the circularly symmetric vortices. One of the interesting things to note about equation (22) is that it is only a function of  $r_a/r_s$  and  $r_b/r_s$ . This means that if the inner and outer limits of integration for the circulation are scaled according to aircraft wingspan, then the relative increase in circulation will be constant. Figure 13 shows a plot of equation (22) over the range of  $25\text{m} \leq r_s \leq 50\text{m}$ , for several different values of  $r_a$  and  $r_b$ . As can be seen from the plot, the further from the core that the averaging radius extends and the smaller the wingspan of the generating aircraft, the larger the effect.

#### 2.2.2.3. Numerical Solution for Lidar Looking at Vortex Pair from an Arbitrary Angle

In this case, the vortices are above and off to the side of the lidar, with an average scanning angle from the lidar to the vortices of  $\theta$ . The vortices are again assumed to be of equal strength and at the same altitude. Figure 14(a) shows the lidar scanning geometry. If the range from the lidar to the vortices is much greater than their separation, the angle the lidar beam makes with the line connecting vortices,  $\theta$  in the figure, is approximately constant as the vortices are being scanned and the geometry can be reduced to that shown in Figure 14(b). The assumption is also made that the lidar range response function width is large compared with the vortex separation, so the observed maximum LOS velocity can come from either vortex. This assumption would be valid for vortices separated by 25 m, for example, at ranges greater than about 200 m. If the vortices are significantly closer to the lidar, then the LOS maximum velocity is strongly determined by which vortex is closest to the lidar focus.

The vortex velocity field used for these calculations has two regimes: solid body rotation within the core radius and a  $1/r$  velocity decrease outside the core. Thus,  $V_\theta(r) = Ar$  ( $r \leq 1$ ) and  $V_\theta(r) =$

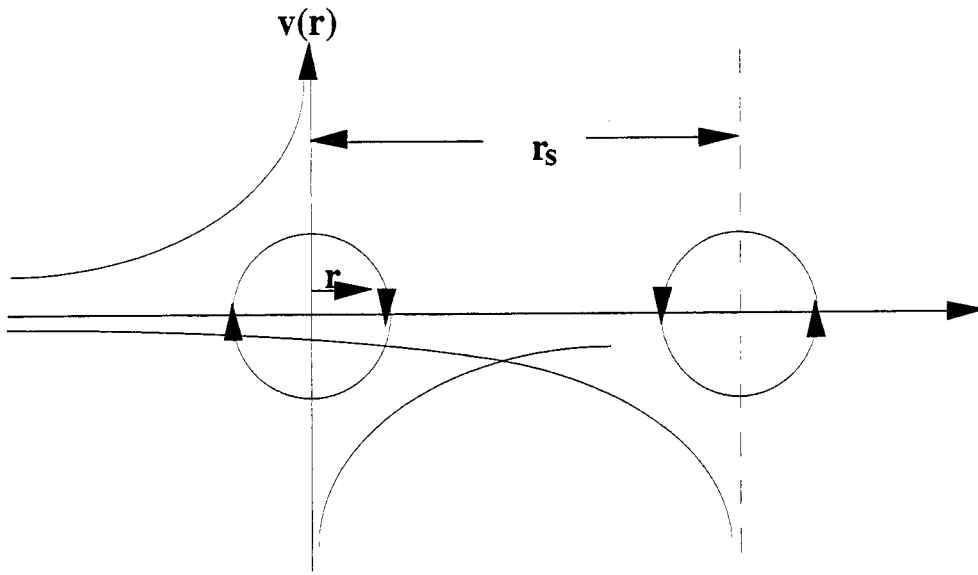


Figure 12. Geometry for circulation estimation in the presence of the neighboring vortex, lidar looking straight up at vortex.

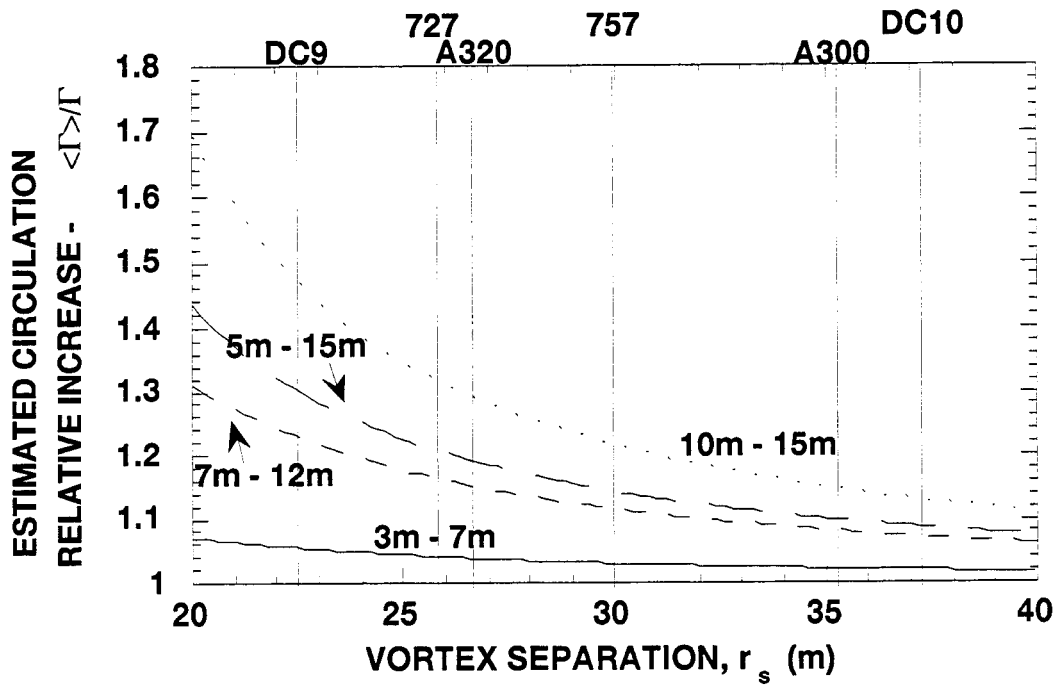


Figure 13. Relative circulation versus vortex pair separation for various radius averaging regimes, calculated from Equation (22). Also shown are the nominal vortex separations for various aircraft, assuming elliptical loading.

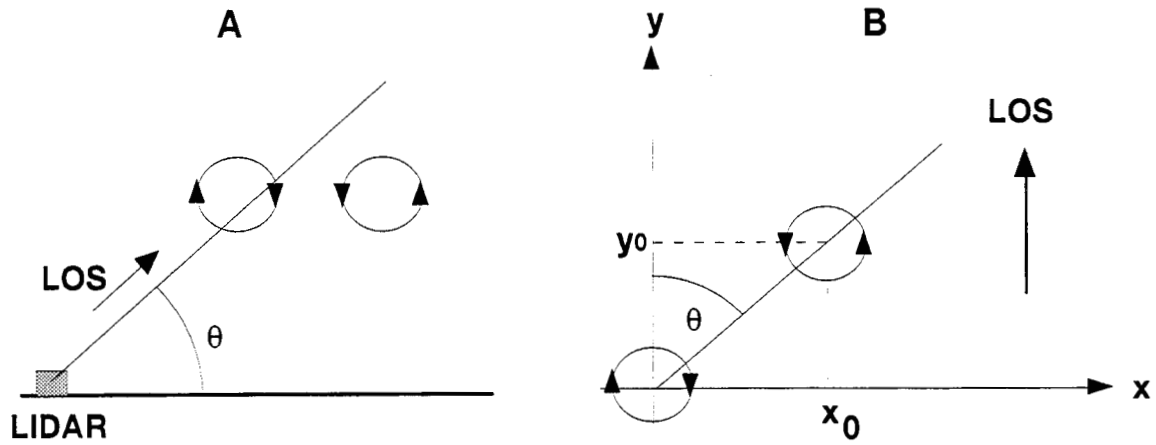


Figure 14. (a) Diagram showing geometry of lidar scanning a pair of vortices with azimuth angle  $\theta$ . (b) Geometry used for numerical calculation of circulation. The assumption is made that the range from the lidar to the vortices is much greater than the vortex pair separation, so  $\theta$  is constant over the scan.

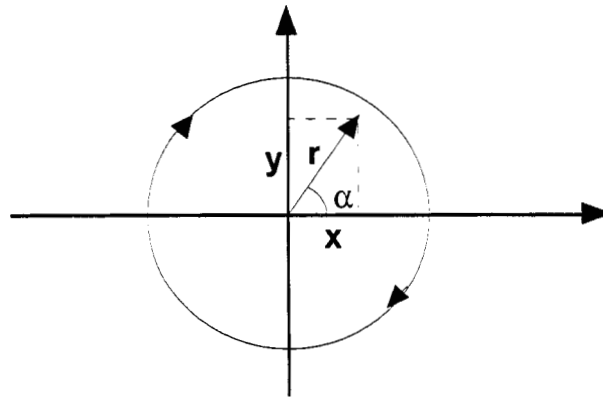


Figure 15. Coordinate system definition for numerical calculation of Figure 14.

$A/r$  ( $r > 1$ ), where the core radius has been arbitrarily chosen to be 1. The y, or LOS, component of the velocity at a point  $(x,y)$  or  $(r,a)$  in the vortex located at the origin can then be written as (see Figure 15):

$$\begin{aligned} V_y &= -\frac{A}{r} \cos \alpha = \frac{-Ax}{x^2 + y^2} \quad (x^2 + y^2 > 1) \\ &= -Ar \cos \alpha = -Ax \quad (x^2 + y^2 \leq 1) \end{aligned} \quad (23)$$

where  $(r, \alpha)$  and  $(x,y)$  are the polar and Cartesian coordinates, respectively, and upward moving velocities are positive and downward moving velocities are negative. The two equations correspond to the y velocity components outside and inside the vortex core, respectively. If the second vortex is located at  $x_0, y_0$  then the y component of the velocity field due to both vortices is given by:

$$V_{y(x,y)} = A \left[ \frac{(x-x_0)}{(x-x_0)^2 + (y-y_0)^2} - \frac{x}{x^2 + y^2} \right] \quad (x^2 + y^2 > 1; (x-x_0)^2 + (y-y_0)^2 > 1) \quad (24)(a)$$

$$A \left[ \frac{(x-x_0)}{(x-x_0)^2 + (y-y_0)^2} - x \right] \quad (x^2 + y^2 \leq 1; (x-x_0)^2 + (y-y_0)^2 > 1) \quad (24)(b)$$

$$A \left[ (x - x_0) - \frac{x}{x^2 + y^2} \right] \quad (x^2 + y^2 > 1; (x-x_0)^2 + (y-y_0)^2 \leq 1) \quad (24)(c)$$

where the three equations correspond to the regions of space that are, respectively, outside both vortex core regions, within the core of the vortex at the origin and outside the core of the vortex at  $(x_0, y_0)$ , and outside the core of the vortex at the origin and inside the core of the vortex at  $(x_0, y_0)$ . It is assumed that the vortex pair never overlap in space, so there never is a region that is within both vortex cores simultaneously. The opposite sign for the contribution from the second vortex comes from its opposite circulation, and the  $x_0$  and  $y_0$  offsets can be written in terms of the vortex pair separation,  $b$ , as:

$$\begin{aligned} x_0 &= b \sin \theta \\ y_0 &= b \cos \theta \end{aligned} \quad (25)$$

The “lidar measured” circulation of the vortex at the origin is then calculated by evaluating equation (17) over a chosen radius regime. The tangential velocity at each point is taken as the maximum LOS velocity along the y direction, which is given by the maximum of equations (24) for the appropriate region of space. In other words, the maximum LOS velocity corresponding to a lidar beam passing parallel to the y axis in Figure 14(b) and not entering the core region of either vortex would be given by the maximum of equation (24)(a) over the lidar path. If the beam passes through the core region of one of the vortices, then the maximum value over the beam path is still used, except equations (24)(b) and (24)(c) are used for whichever core region the beam passes through.

Figure 16 shows plots of the normalized estimated circulation, calculated from equations (24)(a), (b), and (c) as a function of the aspect angle,  $\theta$  (where aspect angle is  $0^\circ$  at the horizon and  $90^\circ$  at the zenith). In Figure 16(a), the relative circulation is shown for various radius averaging re-

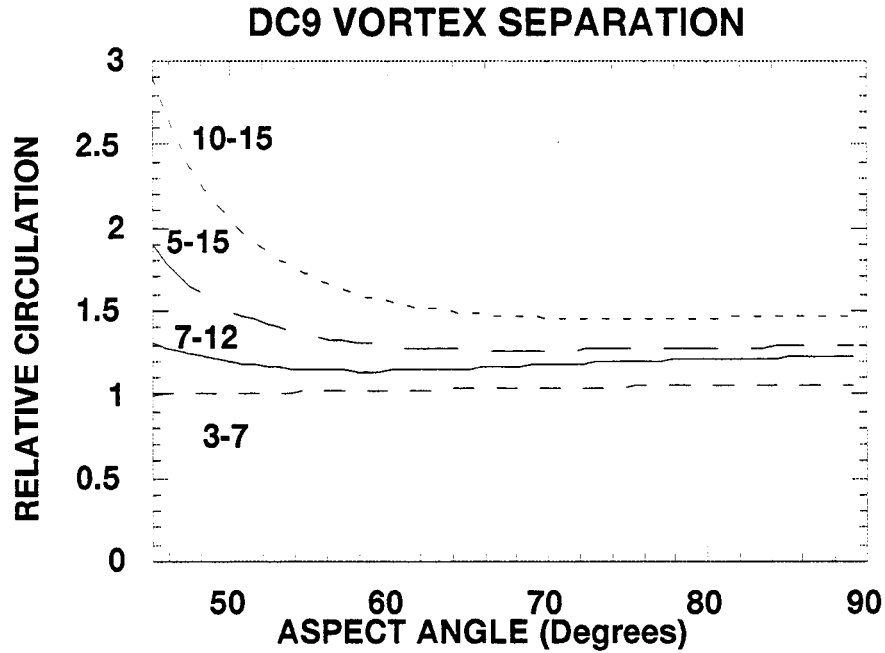


Figure 16(a). Relative circulation increase due to second vortex versus angle between lidar LOS and line connecting vortices. Results shown for various radii averaging ranges, all curves are for 22.4 m vortex separation (DC9).

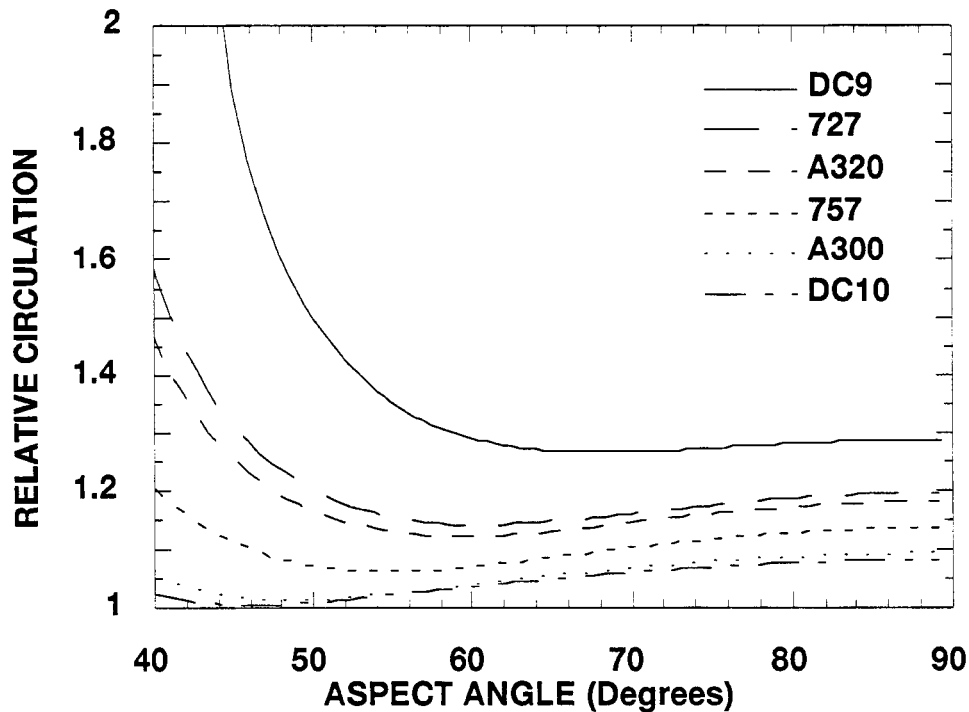


Figure 16(b). Same as Figure 16(a) except the radius averaging range is 5 m – 15 m for each curve and the vortex separations for each curve correspond to the aircraft shown.



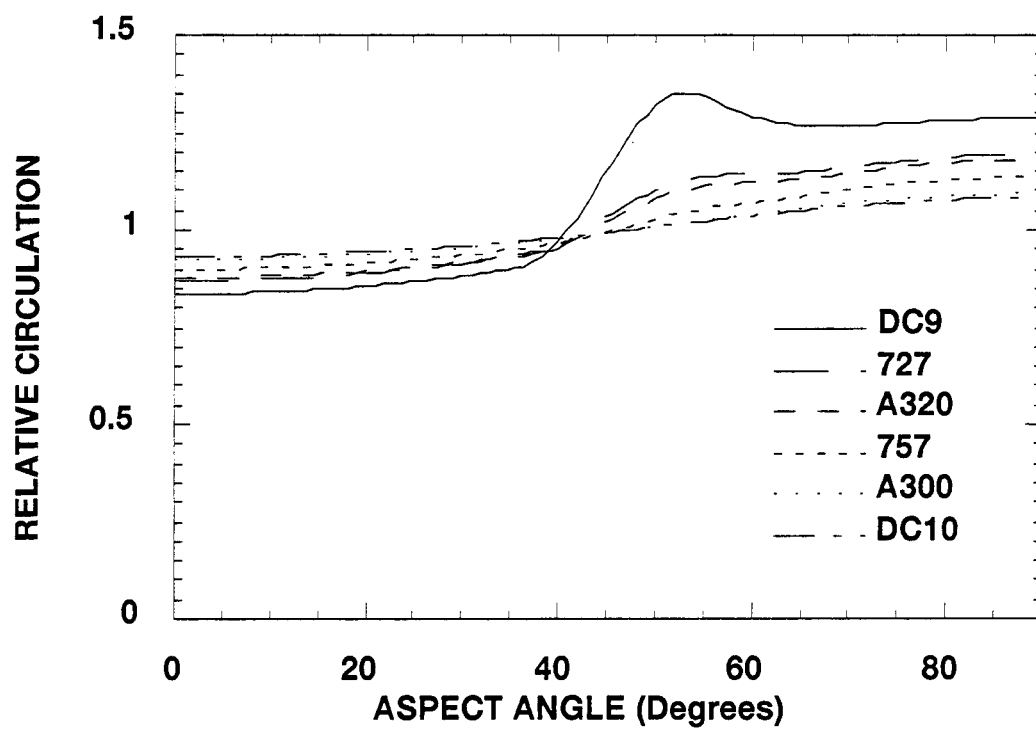


Figure 16(c). Same as Figure 16(b) except the circulation is calculated with only maximum velocities out to 12 m beyond the primary vortex.

gimes, all corresponding to a nominal DC9 vortex separation. In Figure 16(b), the relative circulation is calculated for various vortex separations, all corresponding to a radius averaging regime of 5–15 m. As can be seen from the plots, as the aspect angle is decreased from 90° the normalized estimated circulation at first decreases and then begins to increase as the LOS of the lidar begins to pick up the higher velocities of the second vortex. The magnitude of the deviation of the relative circulation from unity is a strong function of the averaging radius regime and the vortex separation, the effect being reduced at small radii and larger vortex separations.

The results in Figure 16(a) and Figure 16(b) are not representative of measurements in cases where the range to the vortex pair is short enough that the range gate of the lidar is small compared with the vortex separation ( $R \leq 100$  m). In this case, depending on which vortex the lidar is focused on, the signal will be much stronger for that vortex than for the neighboring one, and the maximum velocity in the spectra, depending on the noise level, may just be indicative of the vortex in focus. This situation is approximated in Figure 16(c). In this case, the LOS velocity that went into the circulation calculation from equations (24) is evaluated only out to 12 m in the  $y$  – direction (the primary vortex is at  $y = 0$  and the counter-rotating vortex is at  $y = y_0$ ). This distance is always smaller than the vortex pair separation, so the LOS velocities are more indicative of the vortex at the origin. The arbitrary cutoff of 12 m is roughly representative of a vortex pair range of 100 m, being equal to twice the width of the lidar response function. The actual cutoff distance for a particular range, however, is strongly determined by the signal-to-noise and may extend further. Thus, Figure 16(c) only qualitatively represents the expected results for vortices at shorter ranges. As can be seen from the figure, at lower aspect angles the circulation is actually underestimated due to the opposite direction of the flow from the other vortex.

### 2.2.3. Vortex Tangential Velocity Determination

Now that systematic contributions to the circulation estimate from the presence of the neighboring vortex have been investigated, it is time to consider sensor-dependent effects in determining the tangential velocity and how these in turn affect the circulation determination. As was discussed in the first section, the maximum velocity in the spectrum should be representative of the vortex velocity tangent to the LOS of the lidar. This is true only in the infinite spectral resolution case, however. In practice, the measured spectra can be thought of as the theoretical spectra with shot noise and speckle noise added, then convolved with the system spectral point-spread function. In this case, the maximum velocity must be defined in terms of a noise threshold and will generally be an overestimate of the true tangential velocity due to the system spectral spreading. This section first estimates the velocity spectral spreading due to the windowing function applied to the lidar time series data and then compares that with the measured spreading of the zero-Doppler peaks of the spectra. An algorithm is then described which estimates the true vortex tangential velocity from the maximum velocity in the spectra and the relative amplitude of the spectra in the vicinity of the maximum velocity.

#### 2.2.3.1. Spectral Spreading Due to Time Series Windowing

The process by which lidar spectra are measured and calculated involves the digitization of the amplified and filtered analog signal from the detector followed by the application of an amplitude window function and then the calculation of the FFT. The window function used in the wake vortex lidar is the Hanning window and has the functional form:

$$s(t) = \frac{1}{2} \left[ \cos\left(\frac{2\pi t}{T}\right) + 1 \right] \quad (26)$$

where the windowed time series extends from  $-T/2$  to  $T/2$ . The discrete Fourier transform of equation (26) is given by:

$$s(\alpha) = \frac{\sin(\pi\alpha)}{2} \left[ \frac{1}{\sin(\pi\alpha/T)} - \frac{1}{2 \sin(\frac{\pi}{T}(\alpha - 1))} - \frac{1}{2 \sin(\frac{\pi}{T}(\alpha + 1))} \right] \quad (27)$$

where  $\alpha=fT$  is the relative frequency (spectral bin number). Figure 17(a) shows a plot of equation (26) and in Figure 17(b) is a plot of the square of equation (27), normalized to unity at  $\alpha=0$ . Figure 17(b) also includes a plot of a Gaussian function with full width at half maximum (FWHM) matched to equation (27). As can be seen from the figure, the square of equation (27) is very comparable to the Gaussian shape. This comparison is important because a Gaussian function will be used to estimate the spectral broadening. Since the actual spectra stored to disk are the averaged power spectra from the FFTs, the point spread function of the system is approximately equal to the square of equation (27). This is not exact because the action of squaring the FFTs to generate power spectra is a nonlinear process and so, strictly speaking, the system response cannot be represented by a point spread function. However, a single frequency input to the system will result in a peak of minimum width shown in Figure 17(b). The FWHM of the square of equation (27) can be solved for numerically and is found to be about 1.44 spectral bins. This can now be compared with the width of the zero-Doppler peaks of the lidar generated spectra.

#### 2.2.3.2. Measured Spectral Spreading from Zero-Doppler Peaks

All the velocity spectra generated by the lidar have a peak very near 10 MHz, which corresponds to zero velocity. The origin of this peak is the backscatter of the laser from the system focusing and scanning optics. This zero-Doppler peak is useful to compare with the predicted response from equation (27) because it is the result of the system response to a target at a known and constant velocity ( $V = 0$ ). Therefore, as long as the zero-Doppler signal was not saturating the system (which was generally the case), the width of the generated spectral peak is a good indication of the approximate point spread function of the system. Figure 18 shows the result of averaging the zero-Doppler peaks of 20 representative lidar spectra in which no vortex signal was present and ambient winds were light. Also shown is a fit to a Gaussian function, whose FWHM was 1.88 spectral bins. This is about 30 percent larger than the expected width of 1.44 spectral bins from the signal windowing alone, and the excess spreading may be due to frequency jitter of the master oscillator and local oscillator lasers or due to frequency jitter of the synthesizer controlling the analog-to-digital converter.

Fits have been performed to the zero-Doppler peaks averaged over the first 20 spectra for all the files corresponding to several aircraft push times. This includes over 50 percent of the data collected during the 8/95 collection period as well as some of the data collected during the 12/94 collection period. The results indicate that in almost all cases where the zero-Doppler peak is clearly resolvable, the fit parameters are consistent with the width shown in Figure 18. This is even the case for fitted data from 12/94, where the spectral resolution was 20 cm/s instead of the 80 cm/s velocity bin size for the 8/95 data. One of the properties of equation (27) is that the peak is the same number of bins wide, independent of the total number of spectral bins, and this property is corroborated by the fits to the 12/94 data. These results would indicate that the spectral broadening has remained constant for all the data collected by the lidar and any algorithm that compensates for the broadening would not need to re-measure the width of the zero-Doppler peak for each file.

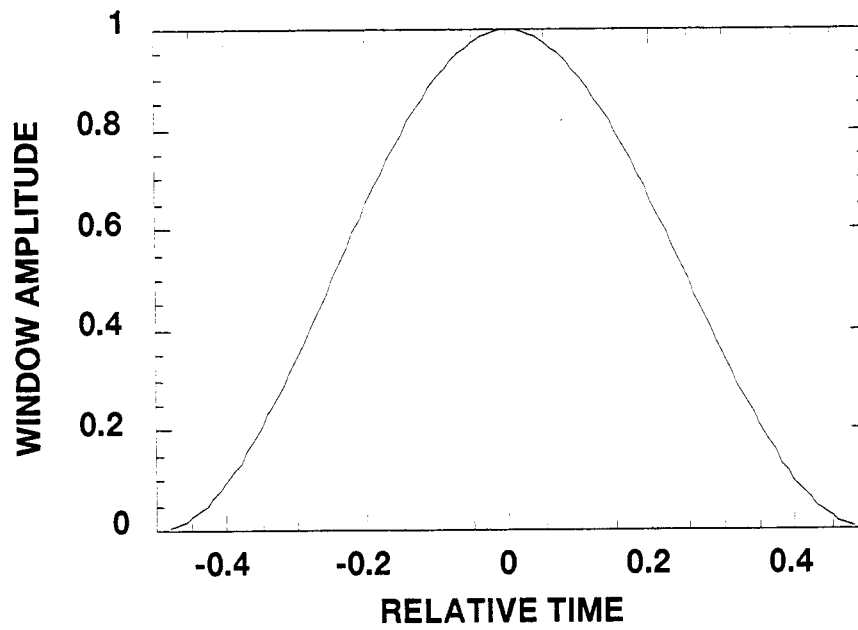


Figure 17(a). Hanning window function from equation (26).

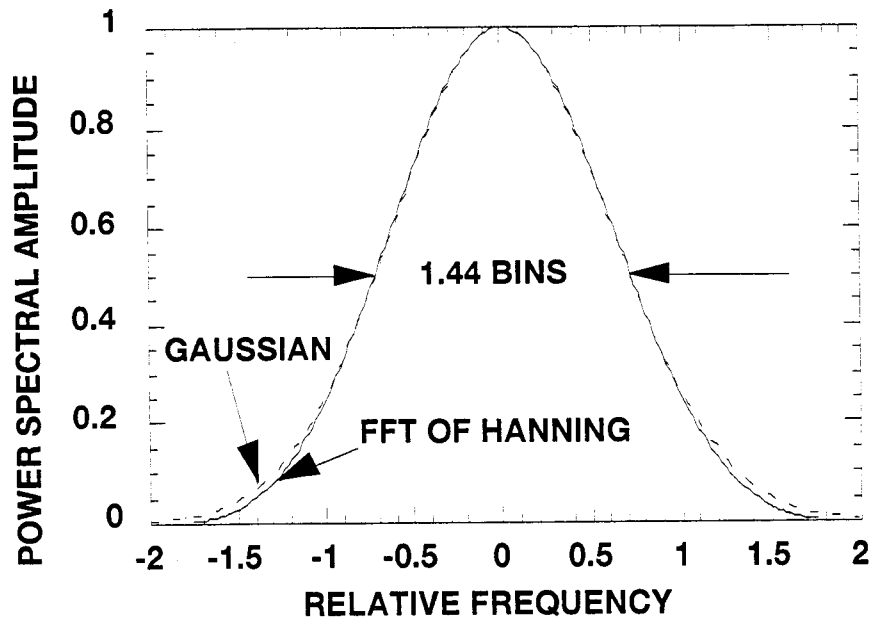


Figure 17(b). The corresponding power spectra of the Hanning window (solid line) and Gaussian profile (dashed line) versus the relative frequency in spectral bins.

#### 2.2.3.3. Proposed Algorithm for Extracting Vortex Tangential Velocities:

Three potential algorithms will now be considered for estimating the vortex tangential velocities and the advantages and disadvantages of each will be discussed. It will then be demonstrated why one of the algorithms is the preferred one for velocity estimation.

The first algorithm considered is the maximum velocity algorithm. This is the simplest algorithm and involves extracting the velocity from each spectra that corresponds to the maximum velocity bin whose amplitude is greater than a pre-determined threshold. This threshold is typically defined as a set number of standard deviations (usually 6) above the average value for each bin, where the average and standard deviation statistics are determined from the first 100 or so spectra in each data file, which are typically collected before the aircraft passes overhead. The primary justification for using the maximum velocity is that it is identically equal to the vortex tangential velocity in the case of infinite spectral resolution. The drawback to this algorithm is that it does not take into account the spectral spreading discussed above, and as a result the calculated circulations tend to be higher than the expected values from equation (17) by as much as 40 percent.

A second potential algorithm for estimating the tangential velocity is the peak velocity algorithm. This algorithm has been used to analyze lidar data collected during the Idaho Falls campaign [1] and involves starting at the maximum velocity bin, as described above, and stepping down in velocity until a velocity bin is reached whose amplitude is less than that of the next highest velocity bin. The velocity corresponding to the higher amplitude bin is then taken as the estimate. In cases of a well defined peak near the maximum velocity, this algorithm works well in picking out its location. The results from this algorithm begin to fail when the peak is not well defined, in which case small bin-to-bin amplitude fluctuations can have a significant effect on which velocity is chosen. This algorithm, as well as the maximum velocity algorithm, also suffer from difficulty when the vortex peak begins to merge into the wind or zero-Doppler peaks. Under these conditions, the maximum velocity algorithm output will saturate at the upper end of the wind or zero-Doppler peak, while the peak velocity algorithm output will fall quickly to the highest point of the zero-Doppler or the ambient wind peak.

The third algorithm for estimating the maximum velocity is the modified maximum velocity algorithm. This algorithm operates in two regimes: one where the vortex peak is resolvable from the wind and zero-Doppler peaks, and one where it is not. In the case where the vortex peak is resolved from the wind peak, the modified maximum velocity algorithm uses as inputs the maximum velocity and the spectral bin amplitudes of the maximum velocity bin and the peak velocity bin, where the maximum and peak velocities are determined by the previously described algorithms. The modified maximum velocity is then determined from the following relation:

$$V_{mmv} = V_{mv} - \Delta V \sqrt{\ln\left(\frac{a_{pv}}{a_{mv}}\right)} \quad (28)$$

where  $V_{mv}$  is the maximum velocity,  $a_{pv}$  and  $a_{mv}$  are the amplitudes corresponding to the peak and maximum velocities, respectively,  $\Delta V$  is the 1/e half-width of the best Gaussian fit to the zero-Doppler peaks from Figure 18 and is equal to 1.13 velocity bins, and  $V_{mmv}$  is the result. Equation (28) calculates the equivalent spread of a Gaussian which has an amplitude  $a_{mv}$  at  $V_{mv}$  and a peak amplitude of  $a_{pv}$ . This velocity spread is then subtracted from the maximum velocity,  $V_{mv}$ . The 1/e width of the Gaussian is given by previous fits to the zero-Doppler peaks. In the case where the vortex peak

is not resolvable from the zero-Doppler or wind peak, the amplitude  $a_{pv}$  is chosen as the bin amplitude four velocity bins down from the maximum velocity bin. The exact choice of bin is somewhat arbitrary and based on the observation that the maximum separation between the maximum velocity and peak velocity was typically less than or equal to four spectral bins. The decision to use the amplitude four bins over is made when the difference in locations of maximum and peak velocities is greater than four spectral bins, which almost always indicates that the vortex peak has merged into the zero-Doppler or wind peak.

An example of the results from each of these algorithms for a scan through a B727 vortex is shown in Figure 19. The pluses correspond to the maximum velocities, the x's correspond to the peak velocities, and the bullets correspond to the modified maximum velocities. Considering the velocities on the negative side of the core, it can be seen from the figure that the peak velocities fall to a constant near-zero value at about  $R = -10$  m, while the maximum velocities plateau a little further out at  $R = -12$  m. Beyond this region is where the vortex peak has merged into the zero-Doppler peak and is shown in Figure 20(a), which corresponds to the dotted line labeled "A" in Figure 19. At these distances from the vortex core, the peak velocity becomes the peak value of the zero-Doppler peak while the maximum velocity is at the upper edge of the zero-Doppler peak. The modified maximum velocity, on the other hand, has a smooth, although not necessarily  $1/r$ , transition to zero velocity in this region.

Results closer to the vortex core where the vortex signal is resolvable from the zero-Doppler peak are shown by Figure 20(b) and Figure 20(c), which also correspond to the B and C labeled dotted lines in Figure 19. The point to note is that even though the radial locations B and C in Figure 19 are close together, the corresponding vortex signals in the spectra are significantly different. In the spectra in Figure 20(b) the vortex signal is more uniform than in Figure 20(c). These differences are primarily a result of speckle effects and the result is that the exact location of the peak of the vortex signal can fluctuate. This also can be seen in Figure 19 as greater fluctuations in the peak velocities. The maximum and modified maximum velocities both appear less susceptible to these fluctuations; but of the two, the modified maximum velocity is a better indicator of the tangential vortex velocity because it compensates for the spectral spreading. Also, the distance between the maximum velocity and peak velocity bins in Figure 20(a) and Figure 20(c) are four spectral bins. This is consistent with the maximum observed for most spectra and is the reason for the upper limit of four spectral bins difference between the maximum velocity bin and the velocity bin used for calculating the modified maximum velocity.

One of the disadvantages of the modified maximum velocity algorithm is that the velocities returned for cases where the vortex peak has merged into the zero-Doppler peak are only an approximation and may have errors. Another disadvantage is that the modified maximum velocity algorithm does not take into consideration spectral spreading due to velocity turbulence within the vortex. Nevertheless, it represents a good compromise between the maximum velocity and peak velocity algorithms. The maximum velocity algorithm is more robust, yet systematically overestimates the tangential velocity because it does not include the effects of spectral spreading. Alternatively, the peak velocity algorithm has the potential to provide accurate velocity estimates; however, it is prone to greater fluctuations due to noise and speckle effects. For these reasons, the modified maximum velocity algorithm will be used to calculate vortex circulations from the lidar data.

#### 2.2.4. Selected Circulation Results

This section presents samples of circulations calculated with the modified maximum velocity algorithm on the 8/95 lidar data. Since actual truth measurements for vortex circulations are not

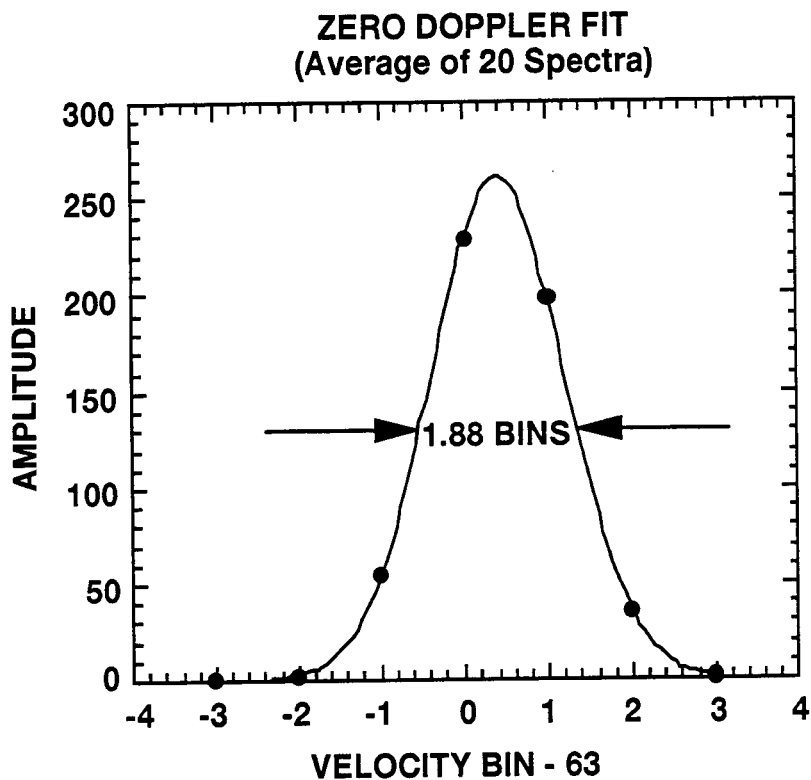


Figure 18. Zero-Doppler peak averaged over 20 spectra (points) with Gaussian fit (solid line).

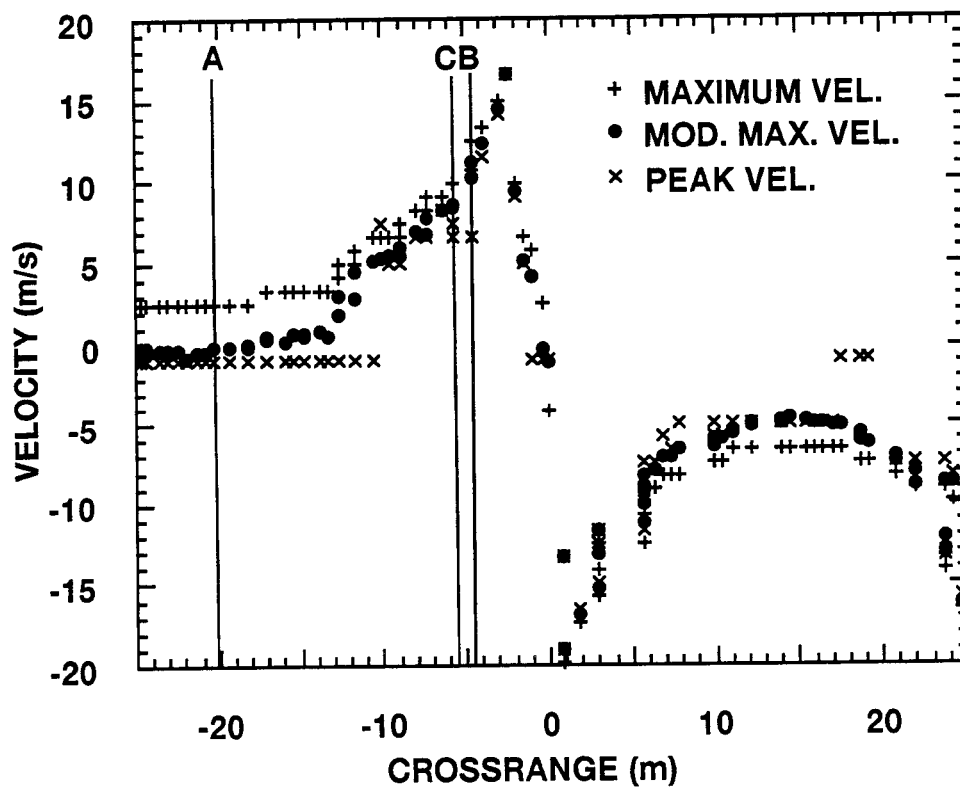


Figure 19. Velocity versus cross range for a scan through a B727 vortex comparing the results for the three velocity estimation algorithms considered. The dashed lines show the location of spectra plotted in the next figure.

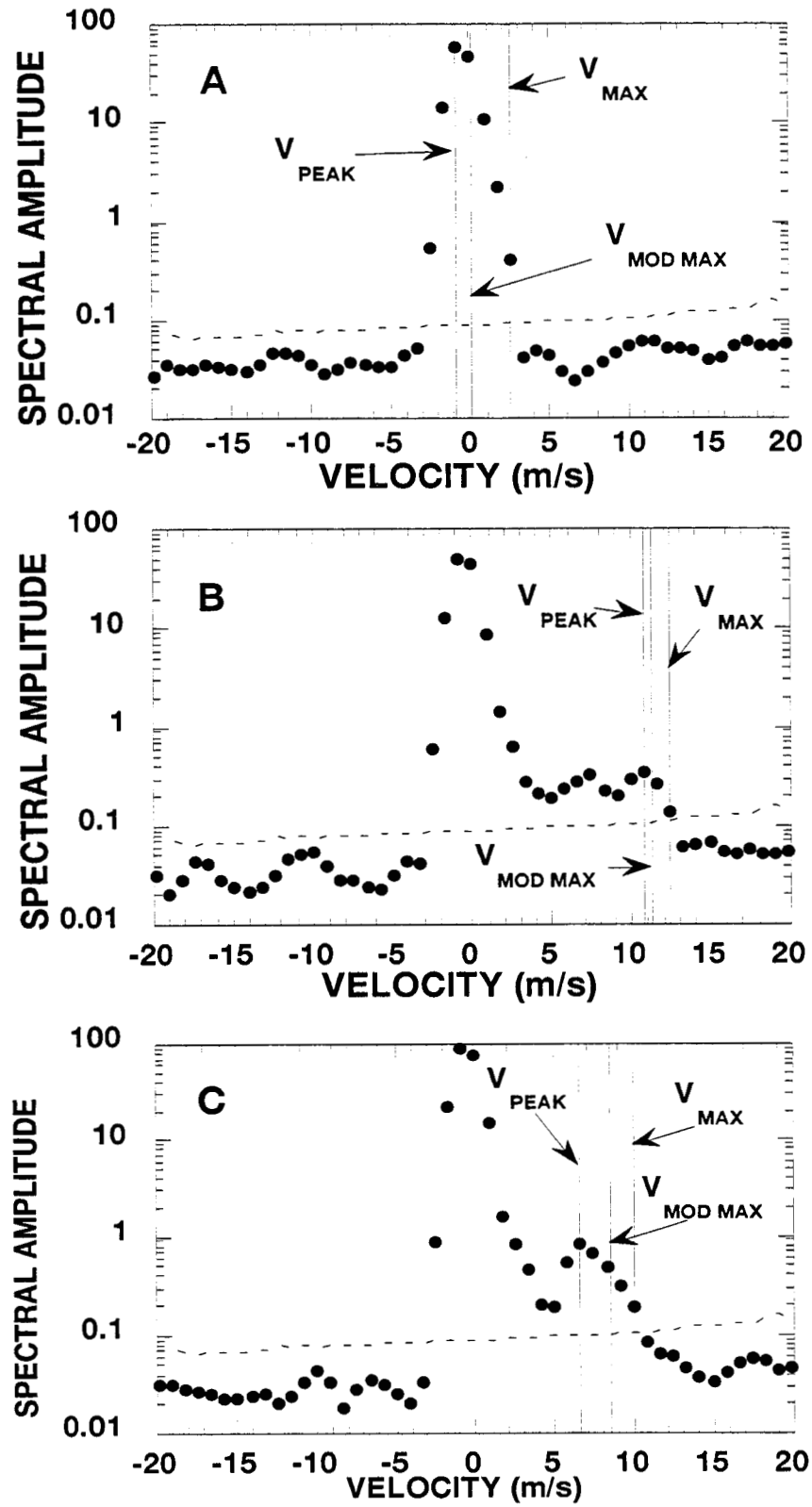


Figure 20. Plots of individual spectra corresponding to the location as shown in Figure 17. (A)  $R = -20$  m from the vortex core; (B)  $R = -5$  m; (C)  $R = -5.6$  m. The dashed line is the threshold and the solid lines represent the velocities returned by the various algorithms.



available, the primary method used to evaluate the efficacy of the results is to compare them with the initial circulations calculated from equation (18), taking into consideration the effect of the neighboring vortex over the radius region in which the circulation is calculated. These comparisons are first made for individual, representative, aircraft cases and then for circulation data averaged over entire pushes.

The first such comparison is shown in Figure 21 and Figure 22. These figures show plots of the circulation normalized to the expected initial values, from equation (18), versus time (solid points) for six different aircraft types which encompass a range of wing spans. Each of these circulations were calculated from data collected at the Memphis National Guard Armory from aircraft landing on runway 36R during the FedEx or evening times when the vortices tended to be longer lived. The date and time of the data collection (GMT) are shown for each of the plots. The circulations were calculated with the modified maximum velocity algorithm over a 5 to 15 m radius averaging range. Included on each of the plots is the prediction from equations (24) of the relative circulation from the influence of the neighboring vortex (solid lines). In order to calculate these predictions versus time, the vortices were assumed not to decay and to descend straight down at a velocity given by  $2C_0/\pi^2b$ , where  $C_0$  is the initial circulation from equation (18) and  $b$  is the aircraft wing span (the factor of  $2/\pi^2$  comes from the definition of the circulation, equation (18), and assuming elliptical loading). The initial position of the vortices was taken as that measured by the lidar after which the vortices were assumed to uniformly descend. This allowed an aspect angle to be calculated versus time from which the predicted theoretical circulations (see Figure 16) could be gleaned. As in Figure 16(c), the lidar was only assumed to be sensitive to velocities up to 12 m beyond the range of the measured vortex for the maximum LOS velocity determination. This would be appropriate for the shorter ranges to the vortices which usually occur as they descend towards the lidar. At these reduced ranges ( $R \leq 130$  m) the effect of the second vortex is to reduce the measured normalized circulations to below unity. In the case where the vortices separate and the influence of the neighboring vortex goes to zero, however, the theoretical prediction would tend to unity. Since the exact shape of the theoretical predictions are strongly dependent on the actual vortex separation and the region over which the LOS velocities are calculated, these results should only serve as guides as to the magnitude of the effect of the neighboring vortex on the circulation estimations.

As can be seen from the plots in Figure 21 and Figure 22, the initial normalized circulations agree very well with the predictions in almost all the cases. In the DC9 and A320 cases, the measurements agree with the theoretical predictions for all the measurement times, suggesting that the observed decay may be primarily due to the effect of the neighboring vortex. For the other planes, however, the measured circulations decrease faster than the theory, suggesting that actual vortex decay is being observed.

Circulation results averaged over entire aircraft pushes are shown in Figure 23 and Figure 24. The plots in these figures show the normalized circulation versus time for all the aircraft of a given type whose vortices were measured during a particular landing push. The circulations were calculated for each aircraft, then normalized to the theoretical initial values from equation (18). The resulting normalized circulations versus time for each aircraft type were then combined and smoothed with a five-point running average. The results for two separate pushes are plotted for each aircraft type. The circulations include data from two FedEx pushes, an evening and a noon push. The solid lines on the plots represent the expected values of the normalized circulations, considering the effect of the neighboring vortex, if the lidar is looking straight up at the vortices. Since the initial aspect angle was slightly different for each individual aircraft, the theoretical circulations of the form

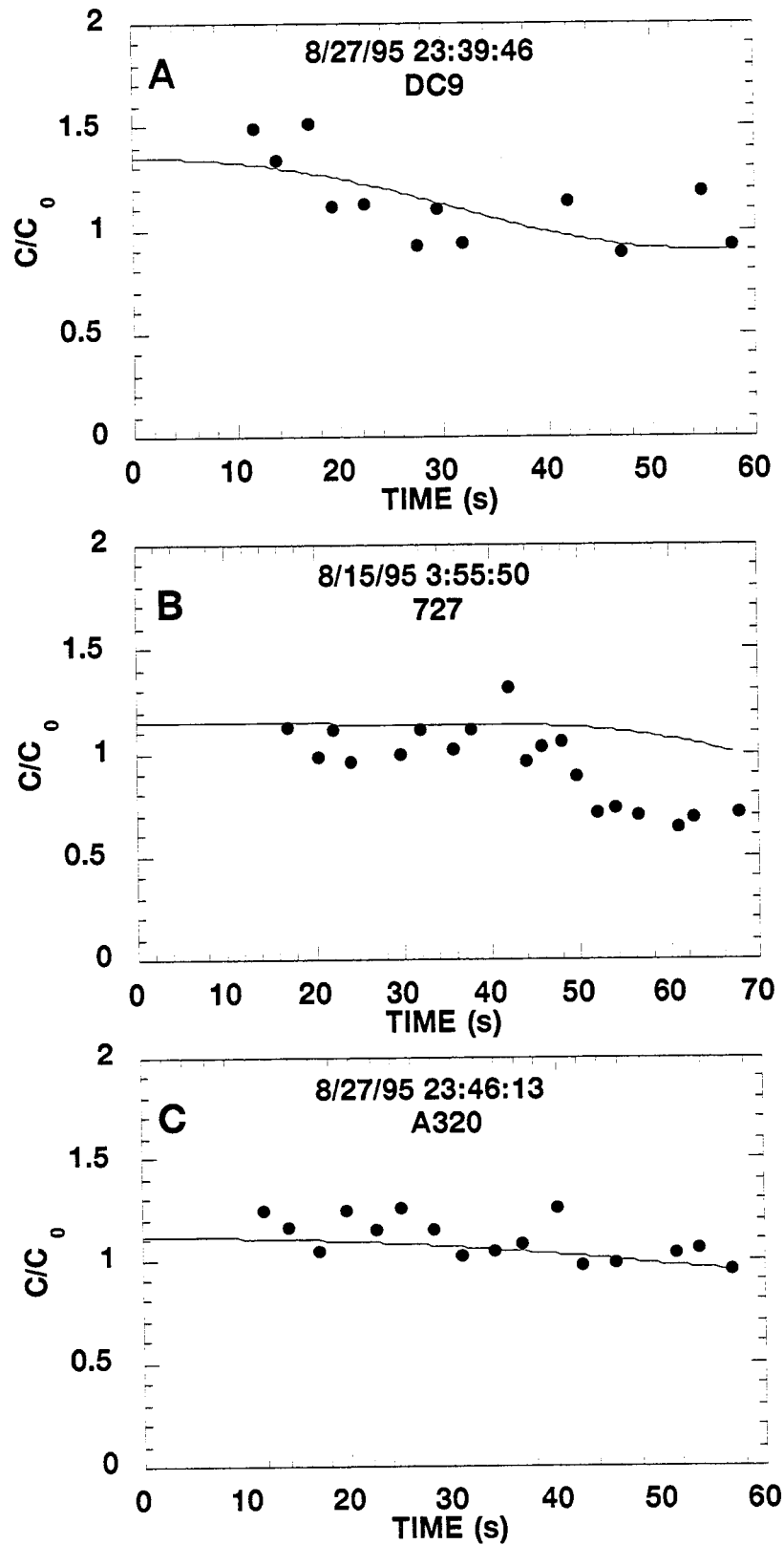


Figure 21. Circulation normalized to the initial theoretical value versus time for several representative aircraft (points) along with theoretical predictions, assuming only the effect of the neighboring vortex and uniform descent (solid lines). (A) DC9, (B) 727, (C) A320.

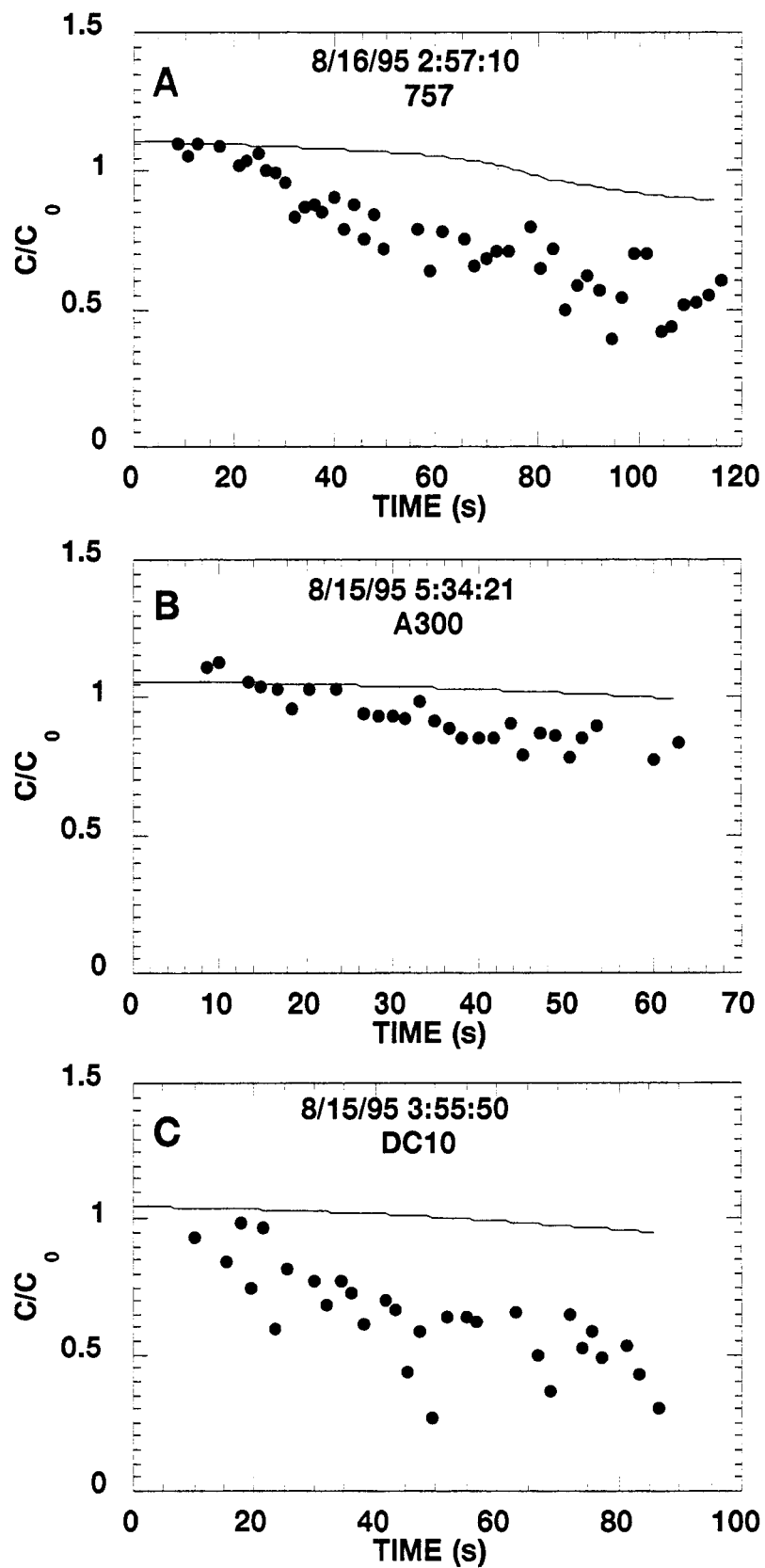


Figure 22. Same as Figure 21 except for different aircraft. (A) 757, (B) A300, (C) DC10.

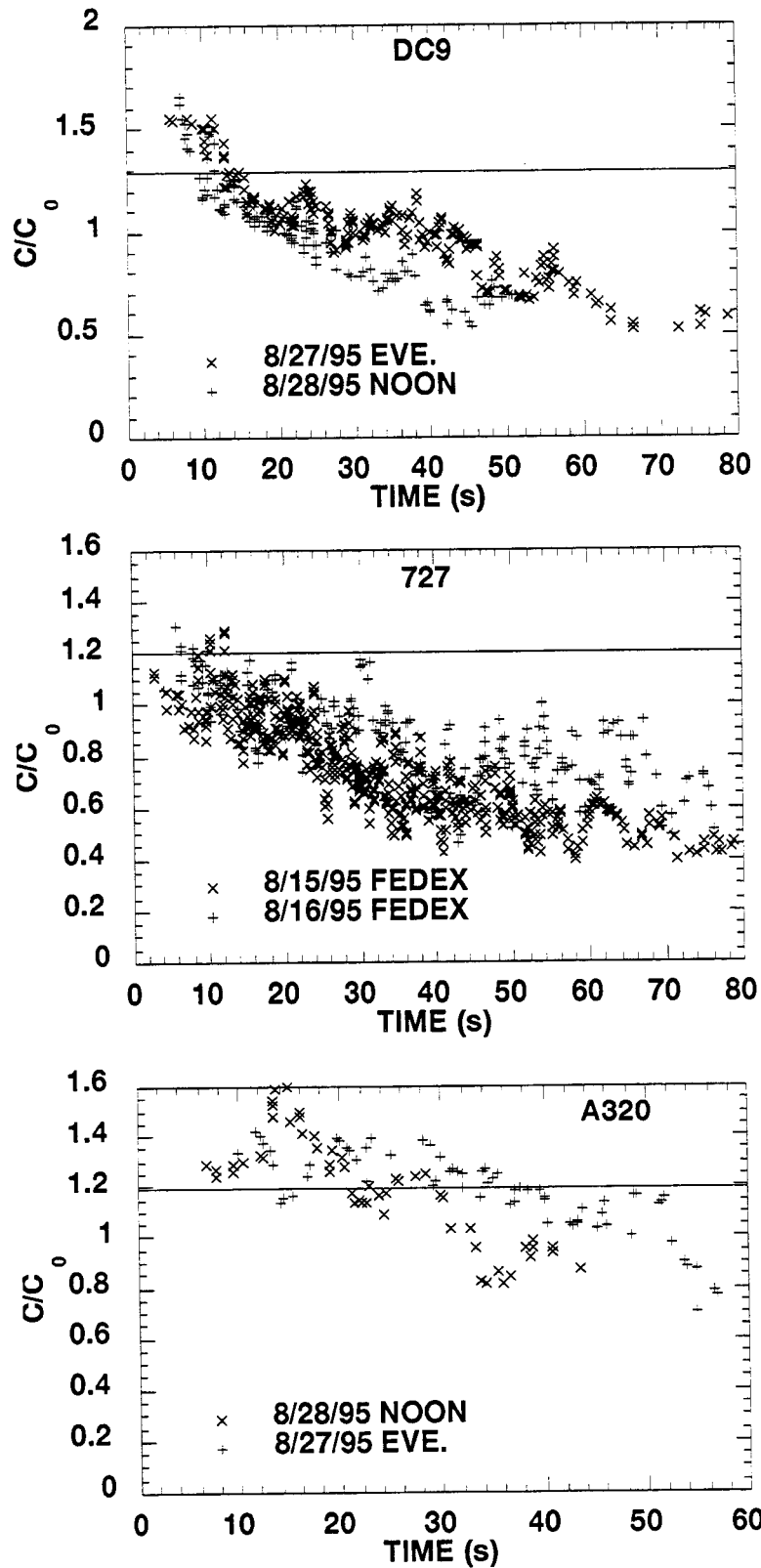


Figure 23. Normalized circulation versus time for DC9, 727, and A320 aircraft over an entire push. Each of the aircraft circulations are individually normalized and the combined data is smoothed with a five-point running average.

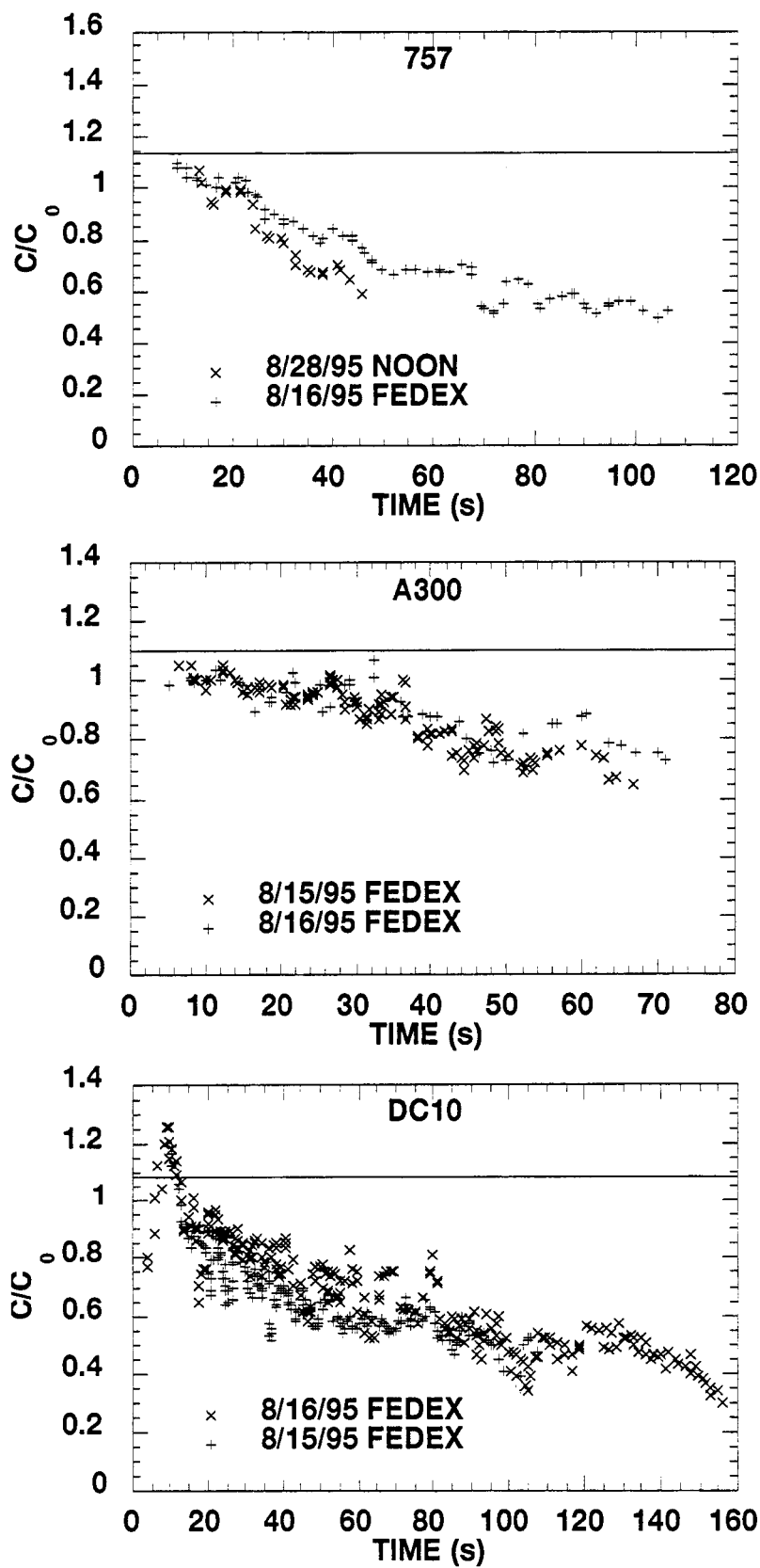


Figure 24. Same as Figure 23 except 757, A300, and DC10 aircraft data are shown.

shown in Figure 21 and Figure 22 would also be different for each. So, a single theoretical value for the 90° aspect angle is used for the comparison. All the circulations were calculated over the 5 to 15 m radius averaging region. The plane counts corresponding to the data in Figure 23 and Figure 24 are: 48–727’s, 15–DC10’s, and 8–A300’s for the 8/15/95 Fedex push; 16–727’s, 2–757’s, 9–DC10’s, and 3–A300’s for the 8/16/95 Fedex push; 21–DC9’s, and 6–A320’s for the 8/27/95 evening push; 20–DC9’s, 7–A320’s, and 2–757’s for the 8/28/95 noon push.

The initial circulations in Figure 23 and Figure 24 generally show very good agreement with the predictions. In most cases, the center of the distributions for the initial normalized circulations are within 10 percent of the predicted values. The initial DC9 and A320 circulations are higher than expected, while those of the A300 aircraft seem to be somewhat lower. The steep decrease in initial circulations of the DC10 aircraft may be due to vortex roll-up, but closer examination of the raw spectra needs to be made to confirm this. The systematic difference in vortex decay observed between the noon and evening pushes for the DC9, A320, and 757 data is presumably due to the higher turbulence levels causing more rapid vortex decay near midday than during the evening.

The calculated circulations in Figure 21, Figure 22, Figure 23, and Figure 24 were all performed over a 5–15 m radius averaging region. The size of all the effects considered will also be affected by the choice of this region. Generally, the effect of the neighboring vortex and, to first order, the differences between the various algorithms for estimating tangential velocities, will be less as the size of the averaging region is reduced and moved closer to the vortex core. The main reason for extending the averaging region outward is the better statistics achieved by averaging more data points. This comes at the cost of greater systematic effects, however.

### **2.2.5. Synopsis of Circulation Calculation Procedure**

This section details the procedure used for calculating the circulations presented in the previous section and in the released circulation data. The inputs to the calculations include the raw spectral files and the vortex position estimates, as determined by the vortex tracking algorithm and described in section 2.2.1. Before the final circulations are calculated, each file is screened manually to determine which lidar scans contain data of sufficiently high quality for accurate circulation calculations. These scans are then flagged and the final calculations are performed on only these scans. The circulation normalizations are performed using aircraft beacon and flight data for the airspeed and weight. The released circulation data is not normalized. The algorithm output includes the circulation values from equation (17), calculated over a set of radius regions, each 1 m wide, centered at 1 m intervals out to 20 m on each side of the vortex core. The circulation calculation procedure is as follows:

1. The first 100 spectra in the raw spectral file are used to calculate the average value and standard deviation of the signal in each velocity bin. These typically represent the spectral output in the absence of a vortex signal.
2. The maximum velocity bin of each spectra in the file whose amplitude is greater than six standard deviations above the average value is extracted.
3. The maximum velocities are sorted according to lidar scans (a lidar scan corresponds to a continuous motion of the scan mirror with the system set at a constant focus position). The maximum velocity versus scan angle data for each scan is then convolved with a matched filter. The filter full width is 30 data points and the functional form is given by:  $1/(\text{data point number} - \text{midpoint number})$  where the data points are numbered from 0 to 29.

4. The peaks of the convolution of the maximum velocities versus angle with the matched filter are taken as the initial guesses for the vortex angular locations. The port and starboard vortices are discriminated by the sign of the convolution peak.
5. The vortex range estimate for each scan is read from the vortex tracking file (generated previously with the tracking algorithm) and a cross range is calculated relative to the vortex core given by the product of the vortex range and the relative angle from the core (as determined from the peak of the convolution in 4.).
6. For each scan, the modified maximum velocities are then calculated, according to the algorithm as outlined, from the raw spectra corresponding to cross range values within 25 m on either side of the vortex core. These velocities are calculated twice for each spectra: once for the positive velocities and once for the negative velocities.
7. The modified maximum velocities versus cross range for each scan are then assembled by taking the positive velocities on one side of the core and the negative velocities on the other side of the core. Which sides of the core contain the positive or negative modified maximum velocities depends on the sign of the vortex considered.
8. The modified maximum velocity versus cross range for each scan is then fit to a Lamb vortex model, using a standard gradient search technique nonlinear-least-squares curvefit routine. The fit parameters include the cross range position of the core, the width of the core region, and the vortex velocity at the core radius. Only the cross range position of the core from the fit is used. This parameter is used to adjust the cross range so the center of the vortex is more accurately located at the zero cross range position. This adjustment is typically less than 1 m.
9. The circulation is then calculated according to equation (17) at 1 m cross range intervals extending from -20m to +20m, with each interval 1m in width. There are typically 1 to 3 velocity points per cross range interval, depending on vortex range.

#### 2.2.6. Circulation Computation Summary

The goal of this section has been to present a detailed discussion of the calculation of the circulation from CW lidar data and some of the systematic effects that influence it. One of the largest systematic influences comes from the velocity field of the neighboring vortex. This effect has been estimated for the case where the lidar looks straight up at the vortex pair by assuming that the velocity field from both vortices decreases as  $1/r$  and then deriving a formula for the relative increase in circulation when averaging over a given radius range. The analysis has been extended to the case where the lidar looks at an arbitrary angle at the vortex pair by assuming that the pair separation remains constant. For instances where the width of the lidar response function is greater than the vortex separation, as occurs at greater ranges, the results indicate that the calculated circulation actually increases as the viewing angle decreases, as the velocities near the core of the neighboring vortex are confused with those of the primary vortex. In the shorter-range cases where the response function width is much smaller than the vortex pair separation, the effect of the neighboring vortex can actually be to diminish the estimated circulation as the vortices descend. These two extremes represent the limiting behavior for the influence of the neighboring vortex on circulation estimation. A more accurate calculation of the circulation over- or under-estimate would require a detailed knowledge of the actual lidar scanning with regard to the vortex position. This simplified model is useful, however, in setting bounds on the size of the effect as long as the region over which it is valid is understood.

Another factor influencing the circulations calculated from the lidar data is the procedure by which the tangential vortex velocities are estimated from the lidar spectra. In this case, the spectral spreading, as primarily determined by the time series windowing function, must be taken into consideration. An algorithm has been developed which approximates the point spread function of the power spectra as a Gaussian function, whose width is determined from fits of the zero-Doppler peak. The spectral spreading is then calculated from the amplitude of the high velocity spectral peaks and subtracted from the maximum spectral velocities to estimate the vortex velocities. The results from this algorithm for the initial vortex circulations agree well with the expected values when the effect of the neighboring vortex is taken into consideration. This algorithm subsequently will be used to process all the lidar data for vortex circulations.

The previous section includes a detailed procedure for the calculation of circulations from each raw spectral file. This is primarily given for completeness and to show how the modified maximum velocity algorithm fits into the vortex data extraction protocol for determining which data are used for actual circulation calculations.



### 3. METEOROLOGICAL DATA COLLECTION AND PROCESSING

The meteorological site at Memphis International Airport is located at 35.029167 north and 89.981111 west. The site is located 1700 feet south of the Airport Surface Detection Equipment (ASDE) tower and 2600 feet north of the ASR-9 radar. This site was chosen based upon the considerations of placing a 150-foot-tall tower in the middle of an airport environment. Fortunately, the site location is ideal for meteorological instrumentation and is within close proximity to the primary lidar sites described earlier.

Figure 25 shows the location of the various sensor systems and their orientation to one another. The site is located on the south side of the Memphis airport between the two primary north-south runways. The 150-foot tower is located at the north end of the site, approximately 200 feet south of the access road and 500 feet north of the building containing the computer equipment. The runway 36R extended centerline is located 1600 feet to the east of the 150-foot tower; runway 36L centerline is located 1800 feet west of the tower.

At the southern end of the meteorological site is the profiler/RASS, Sodar, and a 12-foot by 14-foot building (commonly referred to as the "shed"). The profiler/RASS is located 75 feet south of the shed, and the Sodar is located 75 feet east of the shed. This orientation was chosen due to limitations in the distance from the computer equipment to the profiler and the Sodar. The shed houses all of the computer equipment necessary to run the profiler/RASS, Sodar, tower hardware, and commu-

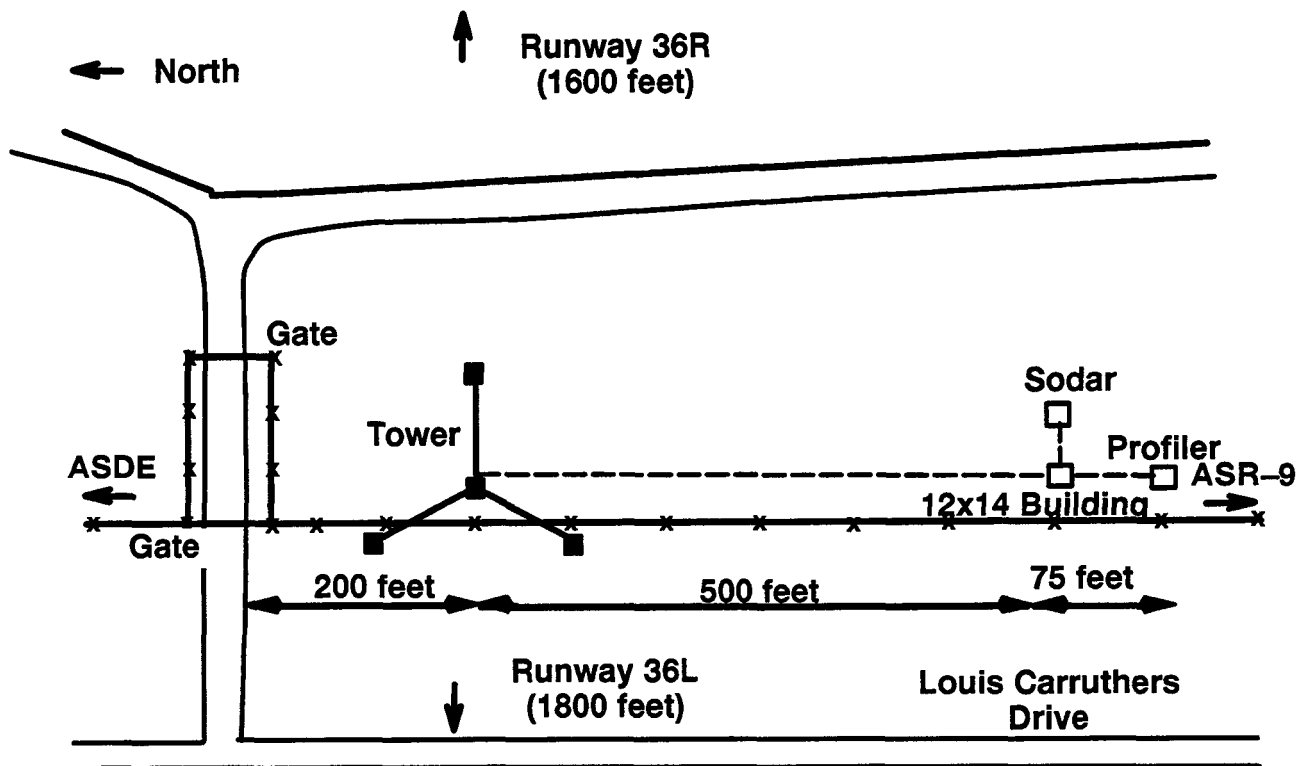


Figure 25. Memphis airport meteorological site.

nications equipment. The shed also was used to house the radiosonde computer equipment; all balloon launches occurred within a few meters of the building.

### 3.1. Instrumented Tower

The meteorological tower is equipped with three different types of sensor packages. The first package, known as a SAVPAK, measures the standard atmospheric variables at a 1 Hz rate. The second, a FLUXPAK, uses a 10 Hz sonic anemometer to measure the atmospheric fluxes. The final tower-mounted package is the barometer. Figure 26 shows the locations of these packages on the tower and variables measured by each package.

The SAVPAK measures four standard atmospheric variables: temperature, relative humidity (RH), wind speed and direction. This is done using two sensors manufactured by R.M. Young of Traverse City, Michigan. The first is the Temperature /Relative Humidity sensor, model 41372C, with the Gill Aspirated Radiation Shield model 43410. The temperature measurement is in degrees Celsius, and the humidity output is in percent. The second instrument is the Wind Monitor-AQ, model 05305. The wind speed is measured in meters per second, with the wind direction given from 0–360 degrees.

The temperature sensor uses a 1000 ohm platinum resistance vs. temperature device (RTD) manufactured by R.M. Young. It has a measurement range of  $-50$  to  $50^{\circ}\text{C}$ , with an accuracy of  $0.3^{\circ}\text{C}$ . Sensor output is an analog signal between 0 and 1 volts. Conversion of the analog output is done within the processing software. The humidity is measured with a Vaisala Intercap element, with a measurement range of 0–100 percent RH. It has an accuracy of two percent from 0 to 90 percent RH, and three percent from 90 to 100 percent RH. The sensor has an operating range of  $-10$  to  $60^{\circ}\text{C}$  and a stability of  $\pm 2$  percent in two years. It produces an analog signal between 0–1 volts that is converted within the processing software. Calibration also can be performed on this instrument in a controlled environment.

The Gill Aspirated Temperature Shield consists of a horizontally-oriented hollow tube and a 24VAC blower mounted on one end, with the sensor on the opposite end. The blower constantly pulls the ambient air across the sensor and down the hollow tube to the blower. The shield employs a downward facing intake tube surrounded by a canopy that minimizes the direct and indirect radiation. The sensor mounts vertically in the center of the intake tube.

The Wind Monitor-AQ measures wind speed using a 20 cm diameter four-blade helicoid propeller carbon fiber thermoplastic. It has a range of 0.4 to 40 m/s, with a gust survival of 45 m/s. The sensor output is an AC sine wave signal produced by a rotating magnet on the propeller shaft. A Wind Sensor Interface, also supplied by R.M. Young, converts the signal into an analog output of 0–1 volts. Wind speed accuracy is reported to be within two percent. The analog signal is converted to meters per second in the processing software.

Wind direction is measured using a balanced vane made of Styrofoam, with a turning radius of 48.3 cm. This lightweight design allows for a rapid response to wind direction changes. The sensor has a  $360^{\circ}$  mechanical range, with a  $5^{\circ}$  electrical opening at  $355^{\circ}$ . The sensor uses a precision conductive plastic potentiometer, 10K ohm resistance, to generate the analog signal of 0–1 volts. Wind direction accuracy is reported to be within one degree. The Wind Sensor Interface, mentioned previously, converts the 12VDC input power to an excitation input.

Each Wind Monitor-AQ is mounted on a one-inch diameter, vertically-oriented pipe at the specified tower heights. The pipe is mounted 36 inches off the tower by using another one-inch-dia-

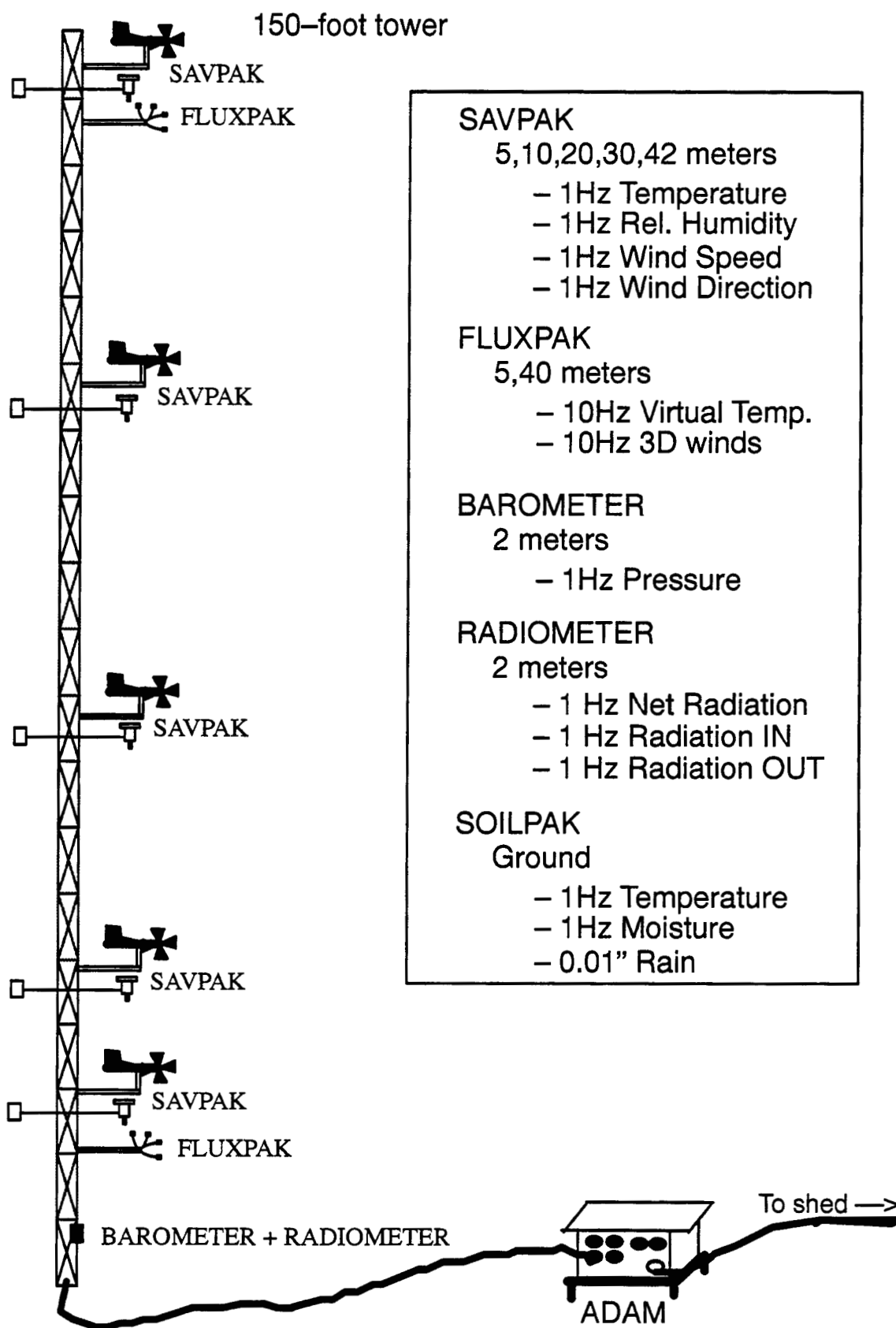


Figure 26. 150-foot instrumented tower.

ter pipe. Each mounting structure is on the southwest side of the tower. Figure 27 shows a top view of the tower and the orientation of the wind sensors. Disruption of the ambient wind is possible from the tower with winds between  $20^\circ$  and  $70^\circ$ .

Alignment is performed on each sensor using the R.M. Young Vane Angle Fixture – Tower Mount Model 18212. First, an alignment ring is secured to the pipe, then the Vane Angle Fixture, and finally the sensor. The vane angle fixture consists of a large compass that will hold the sensor aligned in one fixed direction. Using a known point on the horizon, the sensor can be visually aligned. Finally, a comparison of the known angle and the measured angle is performed. Realignment is performed if the difference is not within threshold.

The FLUXPAK uses a sonic anemometer to measure the three-axis component of the winds and the virtual temperature at a 10 Hz. rate. The sonic anemometer used was manufactured by Applied Technologies, Inc. of Boulder, CO. The sensor transmits and receives a sonic signal along a fixed orthogonal direction, and from this determines the component of the wind. It also determines the sonic temperature of the measured winds from the vertical sonic measurements. The sonic has a measurement range of  $\pm 15$  m/s for the three-axis winds and a range of  $-20$  to  $50^\circ\text{C}$  for the temperature. The wind accuracy is  $\pm 0.05$  m/s and  $\pm 0.05^\circ\text{C}$  for the sonic temperature. The absolute temperature accuracy is  $\pm 2^\circ\text{C}$ . Data output is a serial RS-232C compatible format that is easily interpreted in the processing software.

At the base of the 150-foot tower is a barometer. The barometer is a PTA427 model from Vaisala. It has a measurement range of 800–1100 millibars, with an accuracy of 0.15 millibars. The unit is

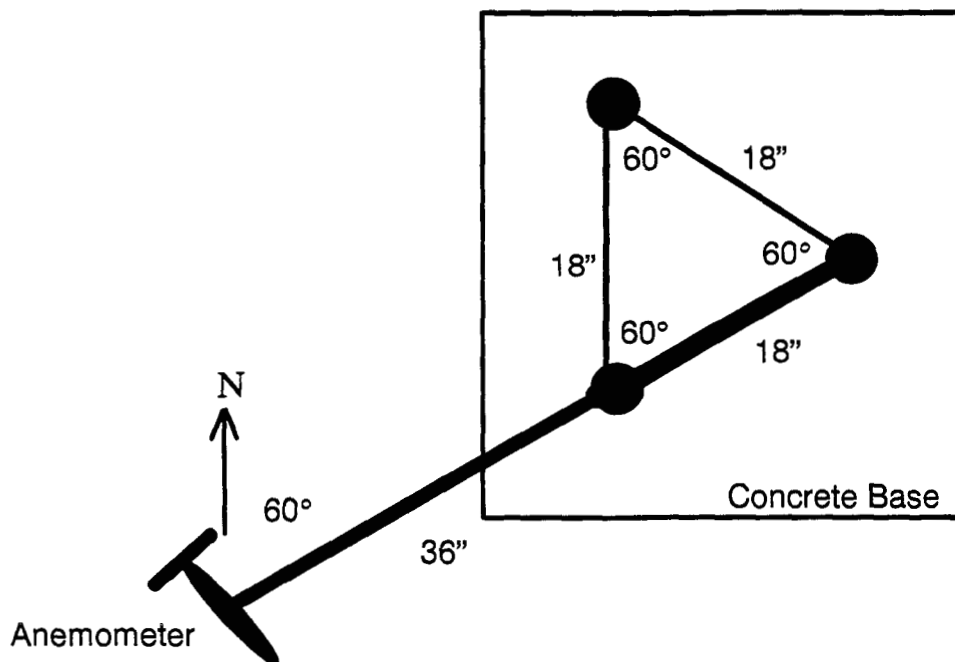


Figure 27. Orientation of Wind Monitor to tower structure.

contained within a weatherproof housing that does provide a pressure fitting for ventilation into the ambient air. The unit produces a 0–5VDC signal that is converted to millibars in post-processing.

### **3.2. Profiler/RASS**

The profiler is a remote sensing Doppler radar capable of determining the wind speed and direction for several different altitudes. The profiler is a 915 MHz system with a four-beam phased array antenna. The unit is manufactured by Radian Corporation of Boulder, CO. The RASS option on the profiler is capable of providing the virtual temperature, and operates at 2000 Hz.

The profiler has a range of parameters that the user may specify for operations. The minimum measurement height parameter was set to 145 meters, and the maximum measurement height was set to 4,881 meters. The profiler was operated with a vertical resolution of 97 meters at a 700 ns pulse. The profiler has a wind speed accuracy of 1 m/s and a wind direction accuracy of 10 degrees. Time averaging of 25 minutes was performed every half hour, allowing a five-minute gap for RASS operations.

The RASS parameters also can be controlled by the operator. For the installation in Memphis, the parameters were set to a minimum height of 127 meters, with a vertical resolution of 105 meters. The maximum height allowed was 1,492 meters. The temperature accuracy of the RASS is reported to be 1°C. The RASS was operated with a five-minute averaging time, performed at the end of each 25-minute wind sampling period.

### **3.3. Sodar**

A sodar provides time-averaged horizontal wind vector and the vertical wind speed. It also provides a measure of the wind variability. The sodar was located 75 feet east of the shed, and the data cables were placed inside a buried conduit for protection. The PC performing the time averaging was located inside the shed, and a serial line was provided from the PC to a Sun workstation.

During the 1994 deployment, a Remtech PA2 sodar was used to measure the winds from 20 meters to 400 meters at a frequency of 2250 Hz. The time-averaging was operated at 10 minutes, with a 20 meter vertical increment. The Remtech PA2 sodar appeared to have performed well, even within the high noise environment of the airport. There also appeared to be very little interference between the sodar and the RASS mentioned earlier.

During the 1995 deployment, an Aerovironment Inc. M2000 sodar was used to measure the winds aloft. Throughout the deployment, the frequency, as well as the operating parameters of the sodar were modified to try and optimize the sodars performance. During the latter half of the deployment, the sodar was operated at a frequency of 2300Hz. The vertical resolution was 20 meters from 40 meters to 500 meters above ground level. The Aerovironment sodar also operated at a 10 minute averaging period. The Aeroenvironment sodar did not appear to perform as well as the PA2 in 1994. Also, the M2000 was adversely affected by the Radian RASS. All data collected during RASS measurement periods should be discarded.

### **3.4. Balloon-LORAN System**

During the deployment, a LORAN CLASS balloon sounding system owned by the University of Massachusetts at Lowell, Meteorology Department, was used for measurements of temperature, pressure and winds. Balloons were launched daily during times of Lidar operations or during times

of significantly interesting meteorological phenomena. The radiosondes were launched from the shed at the meteorological site. Since this site was between the two primary active runways, launches needed to be closely coordinated with air traffic personnel. Typically, balloons were launched five to ten minutes prior to the beginning of the arrival push. Then, another launch occurred five to ten minutes after the arrival push. Special launches were coordinated with air traffic during the non-peak periods to observe meteorological phenomena or coincide with the OV-10 operations.

The CLASS sounding system consists of a disposable Vaisala RS80 sonde which is attached to a 200-gram balloon, a receiver located in the shed, a LORAN-C NORTHSTAR 800 processor, a Vaisala PP-11 processor, and a 386PC. The sonde contains a LORAN receiver that receives a signal from the LORAN system. The LORAN signal, along with an encoded signal from the meteorological sensors, is transmitted back to the shed where another receiver takes the signals and splits them into two components: one to the LORAN processor (position information) and one to the Vaisala processor (meteorological information). The Vaisala processor converts the input signal into temperature, humidity, and pressure and passes that along to the 386PC. The LORAN processor converts the signal it receives into latitude and longitude and sends it to the PC. The PC logs all the data onto disk for post processing. Typically, the PC will produce a data point every two seconds.

The final step is to post process all of the archived data into a consensus file. This step is performed on the PC after the balloon has exploded and the sonde begins to descend to earth. The two-second data from the temperature, pressure, and humidity data sources is averaged into 10-second intervals. The vertical resolution of these intervals depends upon the amount of helium loaded into the balloon. Typically, the data has a 50-meter resolution. Finally, the latitude and longitude information is used to determine the movement of the balloon, thus estimating the winds. These data points are averaged over a 60-second interval. The first reported wind measurement is at 300 meters altitude.

### **3.5. Miscellaneous Sensors**

At the base of the tower were located several instruments to determine the soil characteristics as well as the solar radiation and rainfall. Since all of these instruments were connected to a Campbell Scientific CR 10 datalogger, logging, averaging, and formatting were performed there in a similar manner. These instruments are used mostly for meteorological modeling initial state characterization. All were mounted on an aluminum frame consisting of three cornerposts with cross pieces. Figure 28 shows the location of the instruments at the tower base.

The rain gauge model TE525 was manufactured by Texas Electronics and uses a tipping-bucket mechanism of 0.01-inch increments. The accuracy is within 1.0 percent at two inches per hour or less. It can operate at temperatures from 0°C to 50°C. The instrument produces an electronic pulse each time the bucket tips. The Campbell CR10 counts the pulses in a one-minute period and then sends a format ASCII text line to the serial port.

The radiometer, located at the southern post of the mounting frame, is a THRDS7 model from Radiation Energy Balance Systems (REBS) of Boulder, CO. The THRDS7 contains two high-output, 30-junction thermopiles with nominal resistances of 2 ohms each. It generates a millivolt output proportional to the temperature gradient across them. One thermopile is mounted on the top, the other on the bottom. A temperature sensor is located within the core of the sensor. A radiometer ventilator is used to continuously blow air across the sensor. The ventilator consists of a 12 Vdc blower that is mounted on the bottom side of a hollow tube. Without the ventilator, dew can build up on the radiometer, preventing accurate measurements.

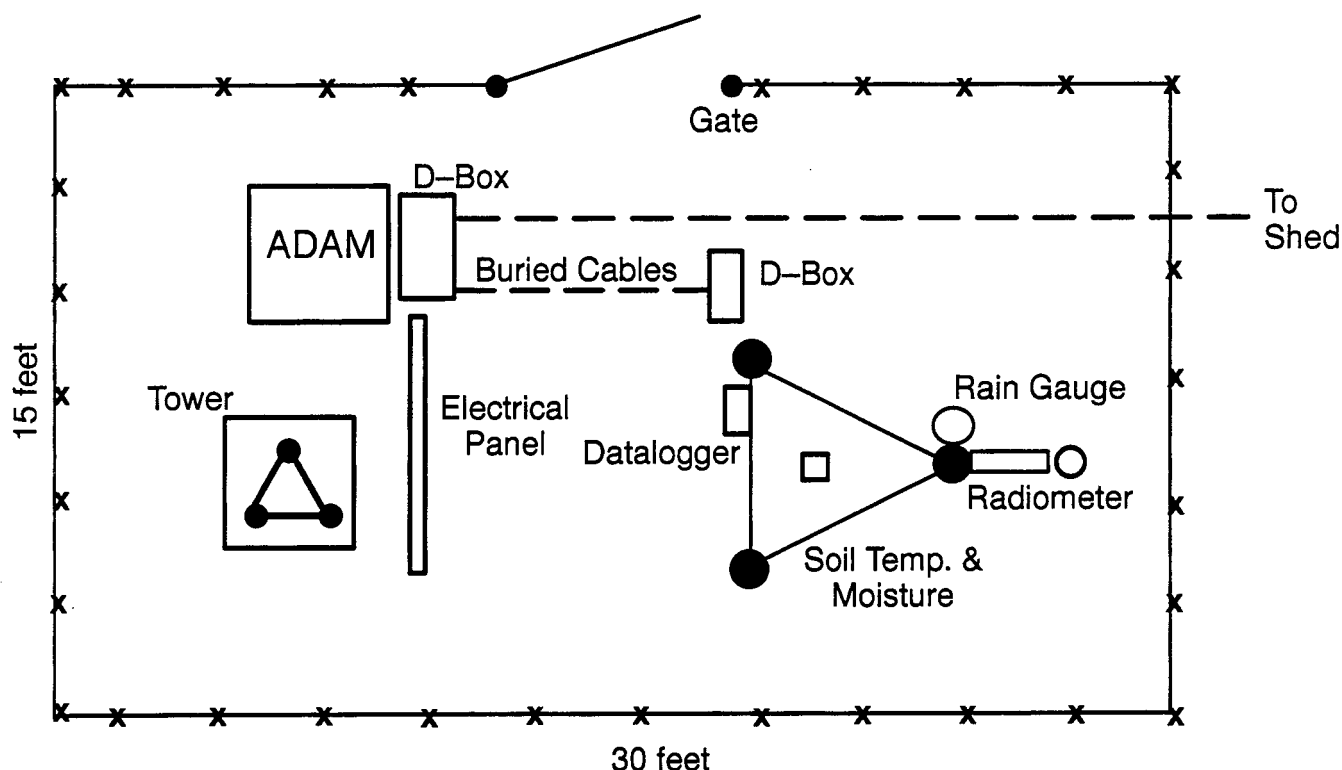


Figure 28. Tower site layout & soil sensors.

The total hemispherical radiation can be computed from the thermopile voltages and the inner air temperature of the core. The incoming radiation is computed by looking at the top hemisphere of the sensor, and the outgoing radiation is computed by looking at the bottom hemisphere. From the incoming and outgoing radiation, the net radiation can be calculated.

The soil characteristics are determined by two sensors, also manufactured by REBS: the soil temperature probe STP-1 and the soil moisture probe SMP-2. The STP-1 is a platinum-resistance temperature probe with a nominal resistance of 100 ohms. It has an accuracy of  $0.05^{\circ}\text{C}$ . The instrument was buried at a depth of 10 cm in the soil. The soil moisture probe consists of two square pieces of stainless steel screen mesh separated by a fiberglass wrapping. The resistance between the two mesh pieces is a function of the fiberglass's moisture content. The resistance ratio measured from the sensor can be converted to weight percent soil water (percentage of water in the soil by weight) using a known polynomial equation whose coefficients depend on the soil type. The soil at the research site in Memphis is a silty clay loam.

### 3.6. Computer Systems

The computer resources required to process, collect, and archive the meteorological data are in four separate locations on the system. The first is the Aster Data Acquisition Module (ADAM), running software to process the data from the 150-foot tower. This software is primarily in C code and was written by the ASTER program at NCAR. The second is the Campbell Scientific CR10 datalogger. The CR10 runs software that process the soil data. This software is Campbell Scientific property and is called by a script written by Lincoln personnel. The third the Sun Sparc 5 workstation located in the shed. Software on the Sparc station collects data from the various data sources and archives it

to disk. The Sparc also communicates with another Sparc station located at the ITWS office. This allows transfer of the data to Lexington and NASA locations.

### **3.6.1. ASTER Data Acquisition Module (ADAM)**

The ADAM, built by the National Center for Atmospheric Research (NCAR), is a weatherproof housing that contains all of the hardware necessary to collect, process, and transmit the data for 48 analog signals and 16 serial connections. It contains a solid-state cooling unit to maintain an acceptable internal temperature. It communicates via a fiber optic link to the Sun workstation located in the shed 500 feet south of the tower.

A series of analog-to-digital boards within the ADAM sample the input sources at a 1 Hz or 20 Hz rate. The sampling rate is controlled by the user by inserting different filter boards. The signal, once converted to a digital signal, is passed along a backplane to a Matrix board. The Matrix board, which contains an Ethernet interface card, reads the data and sends it out on the Ethernet card. In a similar fashion, an Ironics board located on the backplane reads the serial data and sends it to the Matrix board for transmission on the Ethernet interface.

The ADAM, located at the base of the 150-foot tower, receives the signal from the following sensors:

- Five Temperature/Relative Humidity sensors located at 5, 10, 20, 30, and 44 meters
- Five Wind Monitor-AQ sensors located at 5, 10, 20, 30, and 44 meters
- Two Sonic Anemometers located at 5 and 40 meters
- One Krypton Hygrometer located at 5 meters
- One Barometer located at 2 meters

### **3.6.2. Campbell Scientific Datalogger**

A Campbell Scientific CR10 datalogger is located on the aluminum mounting frame on the south side of the 150-foot tower. The datalogger contains the software and electronics provided by Campbell Scientific. A script programmed in the CR10 data language performs a series of functions that the user can instruct the datalogger to perform. At the tower site, the datalogger is instructed to read the input data sources. Then, the datalogger performs the equations necessary to convert the data from its analog input to a digital signal. Next, the datalogger averages the data over a one-minute period, except in the case of the rain gauge, where the datalogger counts the number of input pulses over a one-minute period. Finally, the output data is sent to a serial port for transmission to a display or data reader.

### **3.6.3. Sun SPARC5 Workstation at Shed**

A Sun Sparc5 workstation located in the shed building performs most of the calculations that supply the data in its final format (see Figure 29). The workstation also performs the communications between the ADAM, Campbell CR10 datalogger, Profiler, Sodar, and the Sparc station at the ITWS site. Most of the software was coded by Lincoln Laboratory, although some was provided by NCAR for use with the ADAM communications and processing. The software can be divided into three types: ADAM software, data collection software, and data averaging software.

The ADAM software provides the communications to the ADAM Matrix board, the archiving function of the raw sensor data, and the sampling of the data. The SAVPAK averaging is computed



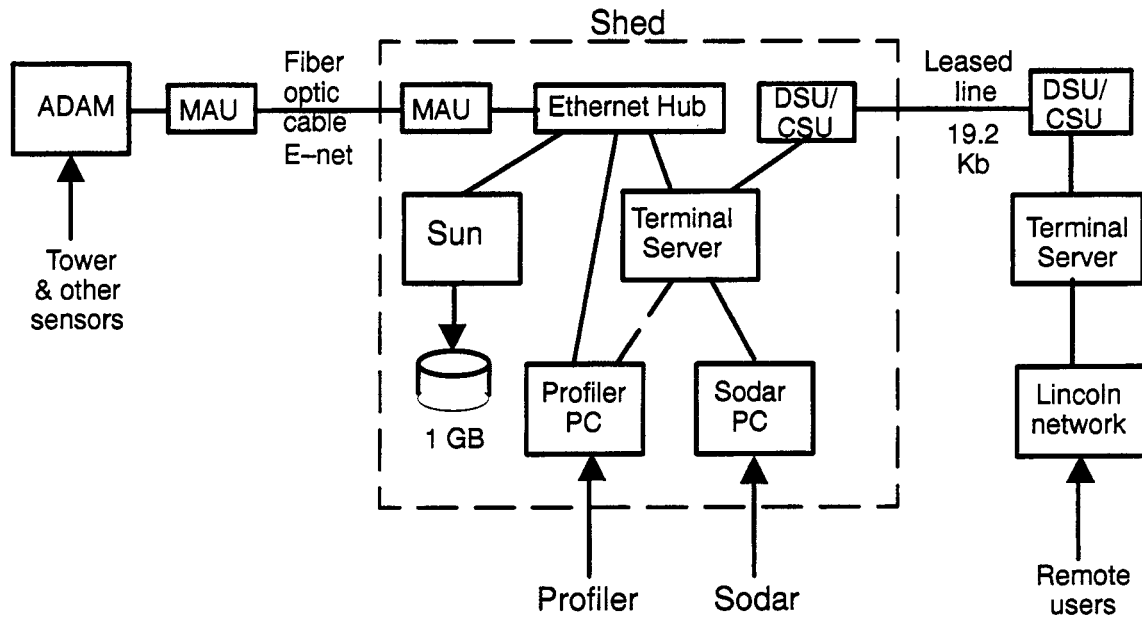


Figure 29. Meteorological data collection computer system.

by sampling all of the data points at a 1 Hz rate and dividing by the number of sample points. Output from this process is an ASCII-formatted printout to the standard display. The sampling time is controllable by the user; for the Memphis experiment, a 60-second sampling was used. The flux data is computed by using the covariance equations.

The data collection software was written by Lincoln Laboratory personnel. It reads the formatted ASCII data provided by the sensors, archives the data, performs a quality check, calibrates the data, and then converts it to an internal Lincoln data format. Each data source requires its own data collection software. Five different pieces of software were written: *profiler\_server*, *sodar\_server*, *savpak\_server*, *fluxpak\_server*, and *campbell\_server*.

The *profiler\_server* reads the serial data from the 386PC processing the profiler/RASS data. The *profiler\_server* must first determine the type of data it is receiving (i.e., profiler or RASS) and translate to a common data format. It also writes the data to an ASCII file for reprocessing. The profiler data provides wind speed and direction for altitudes incrementing from 145 meters to 4,881 meters in 97-meter increments. The east-west and north-south components of the wind are diagnosed from the speed and direction. The RASS provides virtual temperature data from 127 meters to 1,492 meters in 97-meter increments. The translated data is written to a stream for other processes to read. A subprocess reads the profiler data and determines the pressure at each altitude using the surface pressure from the barometer and a standard atmospheric assumption. This subprocess also calculates the virtual potential temperature from the virtual temperature and the pressure. Quality assurance is performed to be sure the wind speed is between 0 and 50 m/s, the wind direction between 0 and 360 degrees, and the virtual temperature between -25 and 50 degrees Celsius.

The *sodar\_server* reads the serial line data from the Sodar. This data is received once every ten minutes and contains the Sodar wind speed and direction for altitudes incrementing from 20 meters to 400 meters in 20 meter steps. The *sodar\_server* writes an ASCII file for reprocessing of the Sodar serial line and writes a data stream containing the wind speed and direction as well as the east-west

and north-south wind components, which are derived from the speed and direction. Quality assurance is performed to be sure the wind speed is between 0 and 50 m/s, the wind direction between 0 and 360 degrees, and the vertical wind component between -10 and 10 m/s.

The `savpak_server` reads the ASCII-formatted data from the standard output of the ADAM processes. First, the ASCII data is written to an ASCII file for later reprocessing. Then from the ASCII data, the altitude, temperature, relative humidity, east-west and north-south wind components are placed in the Lincoln internal format. The pressure at two meters is also read in the ASCII format and held within the Lincoln format. Then the dew point is determined from the temperature and relative humidity, and the wind direction and speed are determined from the east-west and north-south wind components. Next, the pressure at each sensor package is determined by using the surface pressure and the standard atmosphere assumption. Finally, the virtual temperature and virtual potential temperature are determined by using the ambient temperature, dew point and pressure. All of the data are sent on a data stream for reading by other processes. Quality assurance is performed to be sure the wind speed is between 0 and 50 m/s, the wind direction between 0 and 360 degrees, the ambient temperature between -50 and 50 degrees C, the relative humidity between 0 and 100 percent, and the pressure between 800 and 100 millibars.

The `fluxpak_server` reads the ASCII formatted data from the standard output of the ADAM processes and converts the covariance output into the fluxes. Like the other servers, the `fluxpak_server` writes the data to an ASCII format for later processing and then writes the data to a data stream for reading by other processes. Quality assurance is performed to be sure the flux values are between -5 and 5.

The `campbell_server` reads the serial line data from the Campbell Scientific CR10 datalogger. This data is written once every minute and contains the radiometer, rain gauge, and soil sensor data. Again, the server writes the data to an ASCII file for later reprocessing. In this process, the radiometer data is in millivolts, so it must convert the data into something that is useful for meteorological analysis. The formulas applied are provided by REBS, with the final output being the total hemispherical radiation incoming, total hemispherical radiation outgoing, and the net radiation. For the rain gauge and the soil data, the process interprets the ASCII data and writes it into Lincoln internal format. The final step is to write the data to a data stream. Quality assurance is performed to be sure the soil temperature is between -50 and 50 degrees C, the soil moisture between 0 and 100 percent, the rain rate no greater than three inches per hour, and the radiation values between -100 and 1000 Watts per meter cubed.

The data averaging software reads the data from the `savpak_server` and the `campbell_server` to compute the five- and 15-minute averages. This simple process does a running average of the one-minute data. Output is a stream of data for reading by other processes.

#### **3.6.4. Sun SPARC5 Workstation at Lincoln Memphis Office**

The Sun Sparc5 workstation at the Lincoln Memphis office performs the communications with the workstation in the shed and archives the data to disk. The software operating on this workstation is an archiving utility coded by Lincoln Laboratory personnel for use with the ITWS program. The software reads several streams of data being transmitted from the shed workstation and writes it to disk. At the end of each day, a new file is opened and the closed file is compressed and transmitted to the Lincoln Laboratory computer system located in Lexington, MA.

### 3.7. Alignment and Calibration

Calibration of the R.M. Young platinum RTD was performed to improve its accuracy by using an ice bath and a higher-precision temperature sensor. Calibration of the sensors was performed before the fall deployment using the Soil Temperature Probe STP-1 (described in section 3.5.) as the instrument of truth. Each of the R.M. Young sensors was sealed and placed within the ice bath in close proximity to the STP-1. Once both sensors settled to near the freezing point, a series of one-minute averages, from each sensor, was recorded. After ten minutes, the difference between the STP-1 and the R.M. Young sensor was computed, and the error was applied as the calibration factor.

Alignment is performed on the R.M. young Wind Monitor-AQ using the R.M. Young Vane Angle Fixture – Tower Mount Model 18212. First, an alignment ring is secured to the pipe, then the Vane Angle Fixture, and finally the sensor. The vane angle fixture consists of a large compass that will hold the sensor aligned in one fixed direction. Using a known point on the horizon, the sensor can be aligned visually. Finally, a comparison of the known angle and the measured angle is performed. Realignment is performed if the difference is not within threshold.

### 3.8. Sensor Limitations

Limitations in the data exist depending upon the sensor, sensor alignment, wind direction, and weather. No data was removed from the database, based upon these known limitations. The acceptance or rejection of data based upon known limitations or analysis is left up to the user.

Data collected from the R.M. Young Wind Monitor-AQ (SAVPAK variables 15–18 wind speed, wind direction, u component, v\_component) is suspect when the wind is blowing from the northeast (roughly 30 to 70 degrees). This is due to blockage that can occur from the tower structure. During times of strong winds, this appears to be less of a problem.

Data collected from the 20-meter R.M. Young Temperature sensor on rare occasions appears to drop over one degree Celsius. Although rare, this does warrant close inspection of the 20-meter sensor to the 30- and 10-meter sensor data. It is recommended that this data be discarded if discrepancies occur.

Data from the ATI sonic anemometer (all FLUXPAK data) is questionable during times of heavy rainfall. If significant blockage of the beam occurs when raindrops are present, the data can become corrupt, or very few data points are used to compute the averages. Also, wind speeds in excess of 12 m/s are questionable from the ATI due to the sensors limitation of 15 m/s maximum wind velocity for each of the wind components.

Data from the profiler/RASS and sodar and are questionable during times of heavy rainfall. Whenever rainfall is present, analysis with other sensors should be performed to validate the quality of the data.

The close proximity of the sodar antenna and the RASS sound horns was a concern during the Memphis 1995 deployment. During 1994 the sodar appeared to have no difficulty during times of RASS operations. However, during 1995 confidence in sodar data is greatly diminished during periods of RASS activity. Users should compare sodar times with RASS times to help determine the confidence to be placed in 1995 sodar data. The data times are labeled with the beginning of the averaging period of each sensor and the frequency of operation.

Balloon-LORAN system wind measurements were typically widely scattered. Even considering the short averaging times of these wind reports, the correlation with other sensors was generally weak, and the balloon-LORAN system wind measurements are considered highly suspect.

Data from the total hemispherical radiometer can become corrupted in the early morning due to condensation on the windshield of the sensor. The ventilator attached to the sensor helps reduce the occurrence of this problem. However, during mornings of heavy dew formation, condensation can still occur on the instrument.

Finally, errors in atmospheric pressure from the PTA427 can occur in the early morning due to rapid heating within the weather-tight enclosure. A ventilation tube attached to the sensor helps minimize this effect; however, data analysis has shown this does occur in summer when rapid heating occurs.

### 3.9. Meteorological Processing

The data processing software reads the formatted ASCII data provided by the sensors, archives the data, performs a quality check, and calibrates the data. Each data source requires its own data collection software. Three different pieces of software were written: `savpak_server`, `fluxpak_server`, and `campbell_server`.

The `savpak_server` reads the ASCII-formatted data from the standard output of the ADAM processes. First, the ASCII data is written to an ASCII file for later reprocessing. The variables provided by the ADAM are 60-second averages of the 1 Hz data for temperature, relative humidity, wind speed, and wind direction. The pressure at two meters is read and held within the software. Then dew point is determined from the temperature and relative humidity, and the wind direction and speed are determined from the east-west and north-south wind components. Next, the pressure at each sensor package is determined by using the surface pressure and the standard atmosphere assumption. Finally, the virtual temperature and virtual potential temperature are determined by using the ambient temperature, dew point and pressure. Quality assurance is performed to be sure the wind speed is between 0 and 50 m/s, the wind direction between 0 and 360 degrees, the ambient temperature between -50 and 50 degrees C, the relative humidity between 0 and 100 percent, and the pressure between 800 and 1200 millibars.

The `fluxpak_server` reads the ASCII-formatted data from the standard output of the ADAM processes and converts the covariance output into the fluxes. Like the other servers, the `fluxpak_server` writes the data to an ASCII format for later processing.

The covariances are computed within the ADAM using equation (29). The averaging used for this data set was one minute. The  $x$  and  $y$  variables in equation NO TAG, can be replaced with the any of the variables measured by the sonic anemometer. This includes the east-west wind ( $u$ ), the north-south wind ( $v$ ), and vertical wind ( $w$ ), or the virtual temperature ( $T$ ). The  $t$  variable in the equation represents the instantaneous measurement of the variable.

$$\begin{aligned} x'y' &= \overline{(X' * Y')} & \text{where:} \\ X' &= X(t) - \bar{X} \\ Y' &= Y(t) - \bar{Y} \end{aligned} \quad (29)$$

The Turbulent Kinetic Energy (TKE) is computed from the covariances using equation (30). This is performed within the `fluxpak_server` software.

$$TKE = 1/2 (u'u' + v'v' + w'w') \quad (30)$$

The `campbell_server` reads the serial line data from the Campbell Scientific CR10 datalogger. This data is written once every minute and contains the radiometer, rain gauge, and soil sensor data. Again, the server writes the data to an ASCII file for later reprocessing. In this process, the radiometer data is in millivolts, so it must convert the data into something that is useful for meteorological analysis. The formulas applied are provided by REBS, with the final output being the total hemispherical radiation incoming, total hemispherical radiation outgoing, and the net radiation. Quality assurance is performed to be sure the soil temperature is between  $-50$  and  $50$  degrees C, the soil moisture between 0 and 100 percent, the rain rate no greater than three inches per hour, and the radiation values between  $-500$  and  $2000$  Watts per meter cubed.

### 3.10. Atmospheric Profiles

To compare the atmospheric data with the wake vortex behavior, atmospheric profiles must be created from all of the available data sources. These profiles must have enough vertical resolution to demonstrate the fine scale features that may influence wake vortices. Also, the profiles must have sufficient time resolution to detect rapid changes in vortex behavior. However, it is important that artificial features are not created in the profiles that do not exist in the real atmosphere.

To accomplish this task, a truthing tool was developed with the Interactive Development Language (IDL) to display all of the available meteorological data, and allow the human truther to point-and-click at various values and create a profile. It was discovered that in order for a human truther to develop faith in the profiles he/she is creating, the truther needs to have information about the time history of the input data sources as well as information about the future changes in the atmosphere. This was complicated by the various update rates of the sensors.

Wake vortex modelers at NASA Langley Research Center determined that in order to fully understand the effects of the atmosphere on wake vortex behavior, the atmospheric variables must be resolved down to ten meters vertical resolution with a five minute update rate. With the large time averaging of the profiler/RASS, it was decided to perform time interpolation on these input data sources. A simple linear interpolation was used to estimate the parameters in between the time steps of these data sources.

The balloon-LORAN system data provided special problems for the creation of the profiles. First, the launches only occurred at the beginning and end of the data collection periods. Second, the rawindsonde reports the data in 10-second time steps, which do not correlate to fixed altitudes. Finally, the rawindsonde vertical resolution is much lower than the 10 meters required by the wake vortex modelers. Interpolation was performed to the rawindsonde data in both time and height to acquire the desired vertical resolution of 10 meters, and time resolution of five minutes. During the truthing process, the meteorologist must consider such things as averaging period of the different sensors, sensor quality and reliability, and influences of the local terrain.

There are limitations in the data available for the analyses, the display of that data to the analyst, and the resolution. There is considerable uncertainty in the profiles when input data were missing or of poor quality. In these cases, the analyst subjectively weighed the input to produce the final profile. This uncertainty is not indicated in the profile. Also, even though the vertical resolution is given at 10 meters, the input data resolution above 40 meters was considerably coarser. The net result was that frequently the profile was not able to resolve those small-scale features in the atmosphere above 40 meters that could have an impact on individual vortex behavior.



#### 4. AIRCRAFT DATA COLLECTION AND PROCESSING

Aircraft data was obtained from the Air Traffic Control (ATC) system. This data consisted of the beacon reports, obtained from the Air Surveillance Radar (ASR-9), and the flight plans, obtained from information filed by the airlines. This data was collected through a Dimensions International PC interface located in the ATC tower at the Memphis airport.

The beacon data is received from the ASR-9 radar at a four-second update rate. Each time the radar sweeps past an aircraft, the aircraft is queried. The aircraft then transmits to the radar the aircraft transponder code (a unique four-digit number for each aircraft in the airspace) as well as the altitude at which the aircraft is operating. The ASR-9 radar determines the position of the aircraft in the horizontal plane by determining the range and azimuth of the aircraft. For each 360-degree sweep of the radar, data for all of the aircraft in the terminal area are provided.

The flight plan data is received, one per aircraft, approximately one-half hour prior to the aircraft entering the terminal airspace. Each data record contains information on the transponder code, the flight id, the aircraft type, and the coordinated time of arrival at a fix (point in space). The flight id consists of the airline and flight number for the scheduled airlines, or the tail number of all general aviation aircraft. The transponder code in the flight plan can be matched with the transponder code in the beacon data to associate every aircraft in the terminal area with the type, and flight id.

The aircraft beacon and flight plan data are processed to determine the time of aircraft passage over the lidar, the ground speed, true air speed, descent rate, heading, and position with respect to the runway. Winds data from the meteorological processing are combined with the ground speed to determine the airspeed of the generating aircraft.

The algorithm begins by filtering the input beacon data by simply looking at all of the input data for each aircraft as it traverses over the lidar and determining if the beacon report is within some distance of the lidar locations. It also looks at the altitude to determine if the aircraft is out of the lidar range or if the reported altitude is below zero.

The algorithm then smooths the data about the lidar location using a regression line of 60 seconds worth of beacon flight track data. This smoothing process work is acceptable when the aircraft is on a straight flight path with a constant descent rate. Since the majority of aircraft passing over the lidar are on final approach, they will be maintaining a constant track and glide slope.

The next step is for the algorithm to determine the aircraft descent rate, ground speed, and heading by using the slope of the regression line. The position relative to the runway is also computed from the regression line using the known location of the lidar relative to the runway. Finally, the true air speed is computed using the ground speed of the aircraft and the headwind component of the wind estimated from the 42-meter tower wind sensor.

Additional data was obtained from the primary air carriers operating in Memphis. The air carriers provided information on weight and model number for each jet aircraft operated to and from the Memphis Airport. When correlated with the ATC data, the type, model, weight, airline, flight, and beacon code could be determined for which wake vortex measurements were made.





## 5. FIELD MEASUREMENTS

### 5.1. Field Deployment Sites

The 1994 field measurement program was conducted at the Memphis International Airport from November 11th through November 20th and November 30th through December 14th. Only the last two days from the 1994 deployment produced significant data and are covered here. The 1995 field measurement program was conducted at the Memphis International Airport from July 31st through August 29th. Figure 30 depicts the locations of the runways and lidar sites. Also shown is the location of the meteorological site, including the 150-foot instrumented tower situated between the parallel runways.

There were the five lidar locations used during the 1995 deployments: Armory, TANG, Tchulahoma, Winchester and 27 Threshold. The Armory site was located 3.0 km south of the 36R runway touch down zone (TDZ) at the Tennessee National Guard Armory on Holmes Road. This was therefore an out-of-ground-effect (OGE) site with aircraft passing over at nominally 150 m on approach. The TANG site, located at the Tennessee Air National Guard facility, was 1.6 km north of the runway 18L TDZ and therefore a near-ground-effect (NGE) site with the aircraft passing over at 80 m. The Tchulahoma site, located 1.0 km east of the runway 27 TDZ, was also an NGE site with the aircraft passing over at nominally 50 m. The two in-ground-effect (IGE) sites were Winchester and 27 Threshold, located at the runway 18L and runway 27 thresholds, respectively. Aircraft passed over these sites at nominally 15 m (i.e., 0.3 km from the touch down zone). Only the Armory data is given for 1994.

### 5.2. Case Lists

Wake vortex measurements were gathered for 572 aircraft for 31 traffic pushes on 21 days as summarized in Table 3. Measurements were attempted for a greater number of days, but only those pushes for which useful data was gathered are listed here. The main reason that data could not be gathered for a push was generally because landings occurred in a different runway configuration than was anticipated. Also, although measurements for over 600 aircraft were collected, only those for which reliable vortex data was gathered were retained for the final data set.

It can be seen from Table 3 that wake vortex data was gathered at a variety of sites and under a variety of atmospheric conditions. There were four different traffic pushes: morning (7:00–8:00 AM), noon (12:00–1:00 PM), evening (6:00–7:00 PM) and FedEx (11:00 PM–1:00 AM). There were five morning, nine noon, eight evening and five FedEx pushes. Generally measurements were attempted for two pushes on days when the lidar van remained in the same site or one push on days when the lidar van was moved to a different site. There were four IGE, eight NGE and fifteen OGE pushes.

Table 4 summarizes the aircraft types sorted by time of day and distance from touchdown. The aircraft types observed included B747, MD11, DC10, A300, A310, B757, A320, B727, MD80, B737, DC9, F100 and a variety of smaller aircraft. A total of 87 heavy, 394 large jets and 91 other aircraft were observed during the field measurement period.



**Table 3**  
**Memphis Wake Vortex Case List**

Date	Push	Location	Type	Time	Aircraft	Weather	Winds
12/13/94	Evening	Armory	OGE	0020-0120	15	Clear	Light & var
12/13/94	FedEx	Armory	OGE	0500-0700	44	Clear	NE 5-7kts
12/14/94	Evening	Armory	OGE	0030-0120	16	Mstly cldy	N 8kts
12/14/94	FedEx	Armory	OGE	0500-0700	28	Mstly cldy	NE 7kts
8/6/95	Evening	TANG	NGE	2150-0020	21	Ptly cldy	SE 8kts
8/7/95	Evening	TANG	NGE	2340-0020	15	Ptly cldy	SSE 5kts
8/8/95	Noon	TANG	NGE	1700-1830	17	Mstly cldy	SSW 8kts
8/8/95	Evening	TANG	OGE	2320-0040	13	Clear	SSW 6kts
8/9/95	Evening	Winchester	IGE	2150-2300	1	Mstly cldy	SE 5kts
8/10/95	Noon	Armory	OGE	1650-1710	1	Ptly cldy	W 5kts
8/10/95	Evening	Armory	OGE	2300-2350	11	Mstly cldy	Light & var
8/11/95	FedEx	Armory	OGE	0400-0600	31	Ptly cldy	Light SE
8/12/95	Morning	Armory	OGE	1220-1330	19	Clear	Calm
8/12/95	Noon	Armory	OGE	1750-1830	8	Ptly cldy	Light SW
8/15/95	FedEx	Armory	OGE	0325-0605	48	Clear	S 6kts
8/16/95	FedEx	Armory	OGE	0300-0600	52	Clear	SE 6kts
8/17/95	Noon	TANG	NGE	1900-1935	1	Ptly cldy	SE 5kts
8/18/95	Morning	Tchulahoma	NGE	1230-1310	13	Clear	Light & var
8/18/95	Noon	Tchulahoma	NGE	1700-1820	6	Ptly cldy	SE 7kts
8/19/95	Morning	Tchulahoma	NGE	1230-1310	14	Hazy	Calm
8/19/95	Noon	Tchulahoma	NGE	1630-1815	17	Hazy	Light & Var
8/23/95	Evening	Armory	OGE	2230-0015	17	Clear	NE 10kts
8/24/95	FedEx	Armory	OGE	0330-0625	41	Clear	NE 6-8kt
8/25/95	FedEx	27 Threshold	IGE	0345-0545	36	Clear	ENE 8kts
8/26/95	Morning	27 Threshold	IGE	1215-1320	10	Hazy	NNE 5kts
8/26/95	Noon	27 Threshold	IGE	1720-1810	4	Clear	ENE 11kts
8/27/95	Evening	Armory	OGE	2330-0040	16	Ptly cldy	N 10kts
8/28/95	Noon	Armory	OGE	1650-1920	16	Clear	NNE 10kts
8/28/95	Evening	Armory	OGE	2225-0030	11	Clear	NNE 10kts
8/29/95	Morning	Armory	OGE	1230-1320	10	Hazy	E 7kts
8/29/95	Noon	Armory	OGE	1650-1850	20	Ptly cldy	SE 7kts
				Total Aircraft	572		

**Table 4**  
**Memphis Aircraft Types Sorted by Traffic Push**

Date (GMT)	Push	Location	Alt (m)	DC10 MD11	A300 A310	757	A320	727	DC9 MD80	Other	Total
8/26/95	Morning	27 Thr.	15				1		7	2	10
8/18/95	Morning	Tchula.	50			1	1		5	6	13
8/19/95	Morning	Tchula.	50				1	2	4	7	14
8/12/95	Morning	Armory	150			1	2	2	10	4	19
8/29/95	Morning	Armory	150			1	1	1	6	1	10
8/26/95	Noon	27 Thr.	15			1		2	1		4
8/18/95	Noon	Tchula.	50			1		1	1	3	6
8/19/95	Noon	Tchula.	50			1	1	1	1	13	17
8/8/95	Noon	TANG	80		1	1	2	1	8	4	17
8/17/95	Noon	TANG	80					1			1
8/10/95	Noon	Armory	150		1						1
8/12/95	Noon	Armory	150				1		4	3	8
8/28/95	Noon	Armory	150			1	4	1	7	3	16
8/29/95	Noon	Armory	150				3	2	9	6	20
12/13/94	Evening	Armory	150				4	1	7	3	15
12/14/94	Evening	Armory	150				3	1	11	1	16
8/9/95	Evening	Winch.	15						1		1
8/6/95	Evening	TANG	80			1	2		13	5	21
8/7/95	Evening	TANG	80			1	3	1	10		15
8/8/95	Evening	TANG	80				2	2	6	3	13
8/10/95	Evening	Armory	150						7	4	11
8/23/95	Evening	Armory	150			1	3	1	7	5	17
8/27/95	Evening	Armory	150				3		11	2	16
8/28/95	Evening	Armory	150				1		7	3	11
12/13/94	FedEx	Armory	150	10	3			29	1	1	44
12/13/94	FedEx	Armory	150	7				20		1	28
8/25/95	FedEx	27 Thr.	15	3	1			32			36
8/11/95	FedEx	Armory	150	6	3			19		3	31
8/15/95	FedEx	Armory	150	9	8			29		2	48
8/16/95	FedEx	Armory	150	9	10	1		27		5	52
8/24/95	FedEx	Armory	150	9	7			24		1	41
				53	34	12	38	200	144	91	572

### **5.3. Hourly Weather Observations and General Comments**

During the course of the 1994 wake vortex measurement period, conditions did not change significantly. Some periods were clear, while others were cloudy, but it remained dry and winds stayed generally light out of the north and northeast. The boundary layer was stable for all of the collection times. However, this was most likely due to the fact that all of these measurements were taken after sunset.

During the 1995 collection, the weather changed very little from day to day. Conditions followed a typical summertime pattern for the Memphis area. The days were hazy, hot, and humid with generally light winds. The nighttime hours featured hazy, very warm, and muggy conditions also with light winds. Overall, winds were predominantly from the southeast through southwest until August 20th, then from the north through east for the remainder of the deployment. Strongest winds (about 12 kts) occurred during the northeast flow on August 23rd and 26th. The following is a summary of significant meteorological conditions during each aircraft push for which vortex data were collected. This includes both 1994 and 1995.

#### **941213 – Evening (00:20Z–01:20Z) – Armory**

Skies were clear with light and variable surface winds. The lack of clouds allowed for a temperature inversion to form at the surface. Inversion top was located between 44 m and 100 m. Crosswinds were light throughout the push.

#### **941213 – FedEx (05:00Z–07:00Z) – Armory**

Clear skies through most of the push. High clouds moved in late. Surface winds picked up out of the northeast at 5 knots. The top of the surface temperature inversion extended up to 200 m. The boundary layer was very stable and contained little turbulence.

#### **941214 – Evening (00:30Z–01:20Z) – Armory**

Mostly cloudy with surface winds N at 8–10 knots. Because of the clouds and wind, a strong surface temperature inversion was not able to develop. Turbulence kinetic energy (TKE) values were rather low throughout the push.

#### **941214 – FedEx (05:00Z–07:00Z) – Armory**

Mostly cloudy with surface winds northeast at 7 knots. Temperature inversion creating stable boundary layer conditions. TKE values were low throughout the entire push.

#### **950806 – Evening (21:50Z–00:20Z) – TANG**

Scattered clouds at 3500 feet yielded to clear skies by the end of the push. Winds shifted from the southwest over to south–southeast by 23:00Z. Speeds remained steady throughout the push at 10 knots.

#### **950807 – Evening (23:40Z–00:20Z) – TANG**

Scattered clouds at 3500 feet and south–southeast winds at 5 knots. Crosswind values were very light and lidar wind scans suggested no vertical shear below 100m. Very little turbulence in the boundary layer.

#### **950808 – Noon (17:00Z–18:30Z) – TANG**

Cloud coverage was broken at 2000 feet. Winds were out of the south–southwest at 8 knots. Although crosswind values were light (~2m/s), many vortices drifted over the lidar before settling

quickly to the ground. The boundary layer was close to neutral stability above 100 meters and slightly unstable below 100 meters.

**950808 – Evening (23:20Z–00:40Z) – TANG**

Winds shifted from westerly at 23:00Z to southerly by 23:50Z with speeds steady at 6 knots. As during the noon push, vortices drifted over the truck and settled to the ground quickly. Very little turbulence in the boundary layer.

**950809 – Evening (21:50Z–23:00Z) – Winchester**

Skies were mostly cloudy and winds were light southeasterly at the start of the push.

**950810 – Noon (16:50Z–17:10Z) – Armory**

Humid with scattered clouds at 2500 feet. Winds were light out of the west at 5 knots. The boundary layer was close to neutral stability above 100 meters and slightly unstable below 100 meters.

**950810 – Evening (23:00Z–23:50Z) – Armory**

Winds were virtually calm, but skies quickly became overcast and rain ceased operations early. The calculated TKE was relatively high for this time of day.

**950811 – FedEx (04:00Z–06:00Z) – Armory**

Skies were clear with light southeast winds holding close to 5 knots. Both headwinds and crosswinds were very light. TKE values were low, which indicated less turbulence. A temperature inversion caused a stable atmosphere below 250 meters.

**950812 – Morning (12:20Z–13:30Z) – Armory**

Conditions were clear and calm throughout the duration of the push. The boundary layer was very stable below 100 meters and stable above 100 meters with a temperature inversion. The lowest TKE values of the entire field experiment occurred during this period. The vortices seemed to be traveling very slowly.

**950812 – Noon (17:50Z–18:30Z) – Armory**

Scattered clouds at 4000 feet. Winds were light out of the south-southwest at 4 to 6 knots.

**950815 – FedEx (03:25Z–06:05Z) – Armory**

Skies were clear and winds were south at 6 kts. Although crosswind values were low, the vortices seemed to transport rapidly away from the lidar van. A tailwind of 5 m/s was observed. The lifetimes of the vortices seemed to grow shorter towards the end of the push. There was a strong temperature inversion with a very stable atmosphere below 100 meters with vertical wind shear.

**950816 – FedEx (03:00Z–06:00Z) – Armory**

Clear skies and southeast winds at 6 knots. Crosswinds were extremely low, creating variable vortex drift patterns. There was a strong temperature inversion with a very stable atmosphere below 100 meters.

**950817 – Noon (19:00Z–19:35Z) – TANG**

Clouds were scattered to broken at 5000 feet and winds were southeast at 5 knots. All vortices measured were generated by departing aircraft. The atmosphere was near neutral during this period.

**950818 – Morning (12:30Z–13:10Z) – Tchulahoma**

Clear skies with light and variable winds. Light crosswinds kept the vortices moving slowly towards the lidar. The surface boundary layer was extremely stable with the presence of a shallow temperature inversion in the first 100m above the ground.

**950818 – Noon (17:00Z–18:20Z) – Tchulahoma**

Clouds were scattered between 3000–5000 feet and winds remained steady out of the southeast at 7 knots. High turbulence and instability made tracking challenging due to the winds blowing the vortices quickly towards the lidar.

**950819 – Morning (12:30Z–13:10Z) – Tchulahoma**

Clear, calm, and humid. Light headwinds and crosswinds.

**950819 – Noon (16:30Z–18:15Z) – Tchulahoma**

Clear with light and variable winds. Many vortices were long-lived in these conditions. Very low TKE values suggested very little turbulence.

**950823 – Evening (22:30Z–00:15Z) – Armory**

Clear skies and steady northeast winds at 10 knots. Vortices were being blown off toward the west by a 3 m/s crosswind. A headwind of 4.71 m/s was observed. The boundary layer was almost perfectly neutral.

**950824 – FedEx (03:30Z–06:25Z) – Armory**

Clear skies with surface winds northeast at 6 to 8 knots. Crosswinds were fairly steady (3 m/s) above the surface. The vortices were vanishing rapidly.

**950825 – FedEx (03:45Z–05:45Z) – 27 Threshold**

Clear skies and northeast winds at 8 knots. Crosswinds were light, but a tailwind over 4 m/s persisted throughout the push.

**950826 – Morning (12:15Z–13:20Z) – 27 Threshold**

Hazy skies and humid conditions. Winds were north–northeast at 5 knots. There was an elevated inversion at 180 meters, but the vortices were short lived.

**950826 – Noon (17:20Z–18:10Z) – 27 Threshold**

Windy out of the northeast sustained at 12 kts. Crosswinds averaged almost 5.5 m/s along with a tailwind of 3.25 m/s. There was a substantial increase in vertical shear compared to the morning hours. This was due to a change in temperature lapse rate from unstable at 100 m where the nocturnal inversion had eroded, to stable at 400 m. Tracking was difficult in these conditions.

**950827 – Evening (23:30Z–00:40Z) – Armory**

Scattered clouds and winds decreasing from 12 knots. at the start of the push to 6 knots at the end. Moderate crosswinds at 2.5 m/s and a substantial tailwind of 5 m/s.

**950828 – Noon (16:50Z–19:20Z) – Armory**

Clear skies with north–northeast winds at 10 knots during data collection. Crosswinds were light (~1 m/s) with a moderate tailwind at 4 m/s. The boundary layer was unstable below 80 meters, with high TKE values. Above 80 meters, the boundary layer was near neutral.

**950828 – Evening (22:25Z–00:30Z) – Armory**

Similar conditions to the noon push with north–northeast winds at 10 knots, but light cross-winds.

**950829 – Morning (12:30Z–13:20Z) – Armory**

Clear skies with winds east at 7 knots. Strong vertical wind shear was present with a value of nearly 6 m/s over 160 m. As the nocturnal inversion broke down, differing lapse rates existed below 400 meters. Tracking was challenging due to these conditions.

**950829 – Noon (16:50Z–18:15Z) – Armory**

East winds shifted to the south since morning. The vertical shear diminished substantially, making for better vortex tracks. The atmosphere was unstable below 50 meters and neutral above 50 meters.



## **6. SUMMARY**

A comprehensive field measurement program has been conducted for automated collection of wake vortex, atmospheric and aircraft data in an operational airport environment. Measurements were made during December, 1994 and August, 1995 at the Memphis International Airport. Wakes were observed for 572 aircraft during 31 traffic pushes. Data was gathered at five sites at various ranges from the runway touchdown zone during morning, noon, evening and FedEx pushes. A variety of aircraft types were observed, including heavy jets, large jets, turboprops and other aircraft. Data collection and analysis techniques and general conditions during data collection have been summarized.



## APPENDIX A DATA FORMATS

This appendix provides the data formats and examples of each type of data. Section A.1 provides the summary file formats, section A.2 provides the lidar data formats, and section A.3 provides the meteorological data formats.

All time stamps refer to the beginning of the sensor averaging period.

### A.1 Coordinate Systems

Data is provided in one of three different coordinate systems; runway axis coordinate system, lidar axis coordinate system, or meteorological coordinate system.

#### A.1.1 Runway Axis Coordinate System

The origin of the runway axis coordinate system is the end of the runway. For the runway axis coordinate system, the positive x direction is towards the outer marker, while the negative x direction is down the runway. The positive y direction is towards the right (passenger side or starboard side) of the runway, while the negative y direction is towards the left (drivers side or port side) of the runway. The positive z direction is upward. Figure A-1 depicts the runway axis coordinate system.

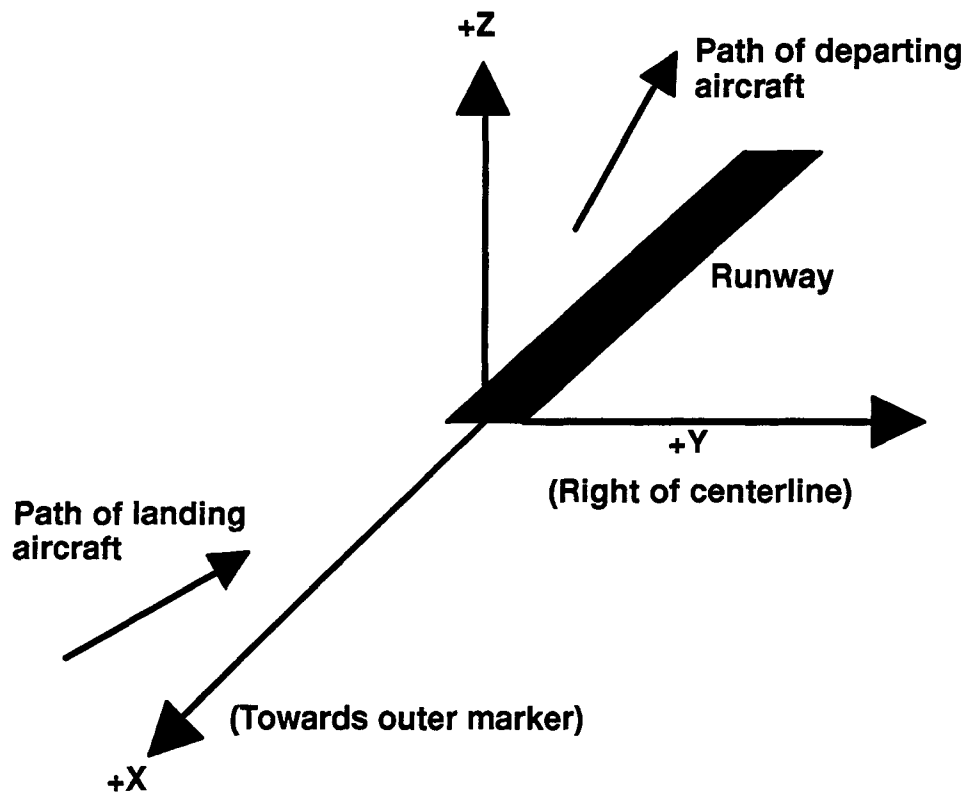


Figure A-1. Runway Axis Coordinate System.

### A.1.2 Lidar Axis Coordinate System

The origin of the lidar axis coordinate system is the ground centered under the scan mirror of the lidar truck. For the lidar axis coordinate system the positive x direction is to the right (passenger side or port side) of the lidar van, while the negative x direction is the left (driver side or starboard side). The positive y direction is towards the front of the lidar truck, with the negative y direction towards the rear of the truck. Finally, the positive z direction is upward. Figure A-2 depicts the lidar axis coordinate system.

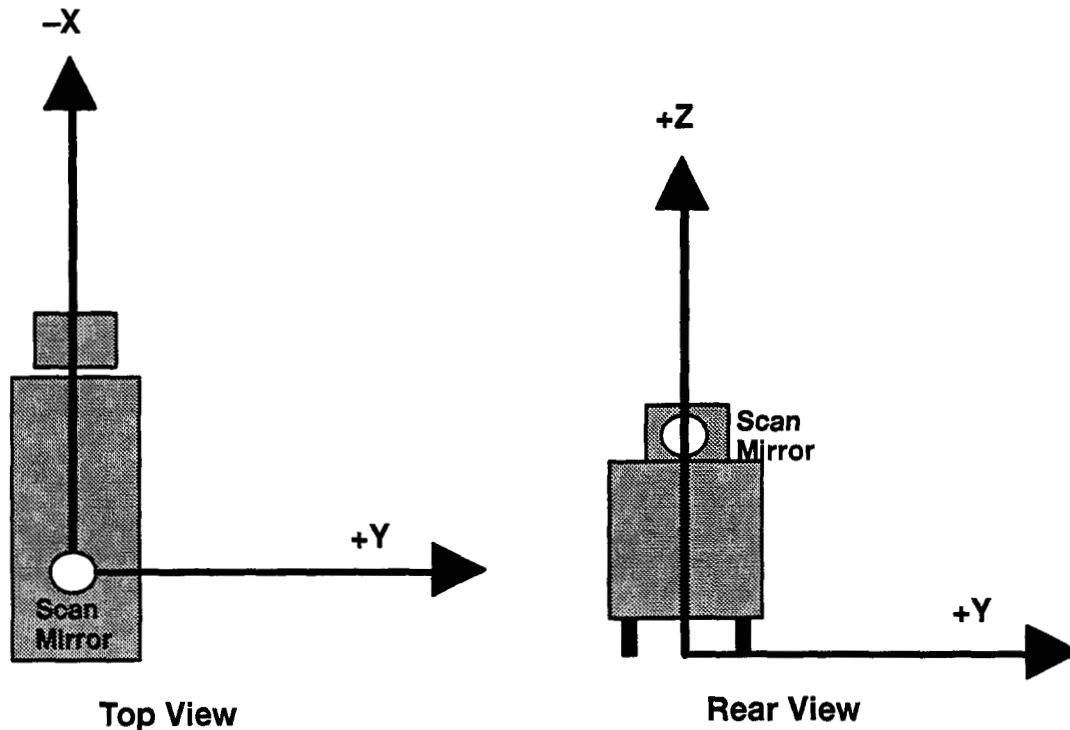


Figure A-2. Lidar Axis Coordinate System.

### A.1.3 Meteorological Axis Coordinate System

The wind data from the meteorological sensors is provided in the meteorological axis coordinate system. For the meteorological axis coordinate system, the origin is the sensor, with the wind direction aligned to true north. The u component of the wind (also known as the east-west wind component) is positive when the wind is blowing from west to east, and negative when the wind is blowing from east to west. The v component of the wind (also known as the north-south wind component), is positive when the wind is blowing from south to north, and negative from north to south.

## A.2 Summary File

The summary file consists of a variety of vortex, meteorological, and aircraft data. Each aircraft event consists of one line of data. This information provides a quick look at the high-level wake

vortex data. One file is produced for the entire data set. The format of the summary file is shown in Table A-1 and is also included as a header to the file. All aircraft position data is provided in the runway axis coordinate system.

**Table A-1  
Wake Vortex Summary File Contents**

	Parameter	Units	Comments
1	Case	N/A	Unique identifier for vortex event
2	Year	N/A	In GMT time, changes with 2400Z
3	Month	N/A	
4	Day	N/A	
5	Hour	N/A	GMT Time of aircraft passage over the Lidar, determined from beacon processes
6	Minute	N/A	
7	Second	N/A	
8	Aircraft Type	N/A	From beacon processes, major type, i.e., B727,DC9
9	Aircraft Model	N/A	From airline data, within aircraft type, i.e., 200,300
10	Aircraft Wingspan	meters	Diagnosed from the type using manufacturers data
11	Aircraft Weight	kg.	From airline data, or estimated from aircraft parameters
12	Weight Accuracy	kg.	Accuracy of weight data
13	Aircraft True Air Speed	m/s	From filtered & smoothed beacon data & winds data
14	Aircraft Ground Speed	m/s	From filtered & smoothed beacon data
15	Runway No.	N/A	Runway on which aircraft was departing or landing
16	Aircraft Climb Rate	m/s	From filtered & smoothed beacon data & winds data; positive is upward
17	Aircraft Offset	meters	From filtered & smoothed beacon data
18	Aircraft Altitude	meters	From filtered & smoothed beacon data & barometer setting
19	Lidar Site Name	N/A	Name of Lidar site at which vortex data was collected
20	Port Initial Circulation	$m^2/s$	Average of circulation values for first 20 seconds of tracking
21	Port Initial Circulation data points	N/A	Number of data points included in the 20 second average of Initial Circulation
22	Starboard Initial Circulation	$m^2/s$	Average of circulation values for first 20 seconds of tracking
23	Starboard Initial Circulation data points	N/A	Number of data points included in the 20 second average of Initial Circulation
24	Theory Circulation	$m^2/s$	Theoretical initial circulation from aircraft parameters

**Table A-1  
(Continued)**

	Parameter	Units	Comments
25	Surface Virtual Potential Temperature	degrees K	From the 10-meter tower sensor, 5-min average
26	TKE5-40	$m^2/s^2$	From the 40-meter Sonic anemometer
27	Crosswind5-10	m/s	From the 10-meter tower sensor, 5-min average
28	Headwind5-10	m/s	From the 10-meter tower sensor, 5-min average
29	Atmospheric Pressure	mb	From the 2-meter tower sensor, 5-min average.
30	Net Radiation	$W/m^2$	From the Radiometer at 2 meter, 5-min average.
31	Comments	N/A	Comments on Data Quality, etc.

### **A.2.1 Lidar Data**

There are two types of lidar data files currently provided: wake vortex circulation and location data (1 file for each vortex), and lidar crosswind data (1 file for each day). Additional data formats will be developed for such information as the velocity profile vs. distance from the core.

### **A.2.2 Wake Vortex Location and Circulation Estimates**

The format for the wake vortex location and circulation estimate data is shown in Table A-2, as is included in each file as a header. All wake vortex location data is provided in the lidar axis coordinate system.

**Table A-2**  
**Wake Vortex Location and Circulation Estimates**

Relative Time	sec	Time Since Aircraft Passage
Y-position	meters	Estimated distance of center of the vortex core laterally from the center of the lidar truck.
Relative Y-error (dely)	meters	Relative Z-location estimation error, using estimates of angle and range estimation errors. Angle estimation error is considered small compared to range estimation error. Range estimation error is given as the half-width of the range optimization cost function. This value should be related to range error, but may not be absolutely accurate.
Z-position	meters	Estimated altitude of the center of the vortex core from the ground altitude at the lidar. Transformations to polar coordinates should subtract 3.86 m from this value first, corresponding to the height of the lidar scan mirror above the ground.
Relative Z-error (delz)	meters	Relative Z-location estimation error, using estimates of angle and range estimation errors. Angle estimation error is considered small compared to range estimation error. Range estimation error is given as the half-width of the range optimization cost function. This value should be related to range error, but may not be absolutely accurate.
Vortex range deviation from lidar focus (r0)	meters	Lidar focus range – vortex range. May be useful in understanding how well focused the lidar was on the vortex for this scan. Vortices closer in focus may lead to more reliable tangential velocity estimates, particularly nearer to the vortex core.
Maximum and minimum velocity cross-range distance	meters	Cross-range distance between the most positive detectable vortex velocity and the most negative detectable vortex velocity. Should be an upper-bound on the vortex core diameter from this viewing angle.
Vortex average circulations { $\gamma(-25)$ , ..., $\gamma(25)$ }	$m^2/sec$	Average circulation estimates of the vortex, at one meter increments from the vortex core, out to 25 meters in each direction. All measurement points within 0.5 m of each estimate point is used in the averaging.

### A.3 Lidar Crosswind Files

Files are provided for each GMT calendar day, specifying estimates of wind perpendicular to the alignment of the lidar truck or approximately perpendicular to the flight path of approaching air-

craft. Each lidar crosswind file contains a commented file header, and a set of crosswind estimates. The file header contains a set of comments (comment lines are denoted by a # symbol as the first character) detailing the time of generation of the data file and the file format. The first three data lines after the initial comment lines contain information shown in Table A-3. Each subsequent line after the file header contains lidar crosswind estimates, one per line. Table A-4 details the contents of each crosswind estimate. All lidar crosswind data is provided in the lidar axis coordinate system.

**Table A-3**  
**Lidar Crosswind File Header Data**

Algorithm Version	Version of data processing algorithm used to generate this data set, indicated by a number and a following letter. The letter "P" indicates postprocessed data, while "R" indicates real-time data.
Data Format	File format number. This document describes the content of file format 1.

**Table A-4**  
**Lidar Crosswind File Estimate Data**

Start Time	Beginning time of interval used to estimate crosswind, given by 6 numbers as: years since 1900, month, day, hour, minute, seconds.
Airport	Three letter airport identifier where measurements were taken.
Site	Text identifier of lidar site. Lidar sites for Memphis deployment are discussed in Appendix B.
Averaging Time (s)	Length of time interval used to estimate mean crosswind.
Altitude (m)	Altitude above lidar ground level of estimate.
Mean Crosswind (m/s)	Average crosswind estimate.
Standard Deviation (m/s)	Standard deviation of crosswind sample points used to in mean estimate.
Number of Averaged Samples	Number of crosswind samples used in the mean and standard deviation estimates.

### A.3.1 Meteorological Data

A number of different data file formats have been defined for distribution of the meteorological data files to NASA. These consist of the SAVPAK data files, the FLUXPAK data files, the Soil data files, and the Atmospheric Profile files. Each data file format is specified below. All meteorological data is provided in the meteorological axis coordinate system.

The SAVPAK data files consist of the standard atmospheric variables measured by the five sensor packages located on the 150-foot meteorological tower. These sensors are located at 5, 10, 20, 30, and 42 (or 44) meters. The sensors directly measure the ambient temperature, relative humidity, wind speed and direction. The software included in the savpak\_server computes the virtual temperature, potential temperature, virtual potential temperature, and north-south, east-west wind components. The pressure is measured at two meters above ground level, and estimated for five tower SAVPAK locations. All data is one minute averages output every minute. The SAVPAK data format is shown in Table A-5.



The FLUXPAK data files consist of the covariance measurements at the two sonic anemometer located on the 150-foot meteorological tower. These sensors are located at 5 and 40 meters. The sensors directly measure the east-west and north-south wind component, as well as the virtual temperature. All measurements are performed at a 10Hz data rate, averaged for one minute, and output every minute. The format for the FLUXPAK data is shown in Table A-6.

The Soil data files consist of the soil measurements performed at the base of the 150-foot meteorological tower. The sensors output included in this data file are the Soil Temperature Probe (STP-1), the Soil Moisture Probe (SMP-1), the Rain Gauge (TE525), and the Total Hemispherical Radiometer (THRDS-7). The Soil Temperature Probe and the Soil Moisture Probe are located at the depth indicated in the file. The Rain Gauge and Radiometer are mounted on an aluminium structure, at a two-meter height. All data is one minute averages, output every minute. The Soil data file format is shown in Table A-7.

The Atmospheric Profile files consist of the hand truther atmospheric profiles created in post-processing by an expert meteorologist. The data output included in this data file are temperature (ambient, virtual, potential, and virtual potential), and winds (east-west and north-south component). All data is a compilation of all available data sources, output once every five minutes. The Atmospheric Profile data format is shown in Table A-8.

**Table A-5**  
**SAVPAK Data File Contents**

	Variable	Units	Description
1	Year		Date of data collection, changes with 2400Z
2	Month		
3	Day		
4	Hour		Start time of data collection
5	Minute		
6	Seconds		
7	Height	meters AGL	Height of sensor package above ground level
8	Pressure	Millibars	Pressure at sensor package height, estimated from 2-meter barometer, using Standard Atmospheric Assumption
9	Ambient Temperature	degrees C	Ambient Temperature, from R.M. Young Temperature/Relative Humidity Probe
10	Virtual Temperature	degrees C	Virtual Temperature, computed from Temperature, Dew Point, and Pressure
11	Potential Temperature	degrees K	Potential Temperature, computed from Temperature and Pressure
12	Virtual Potential Temperature	degrees K	Virtual Potential Temperature, computed from Virtual Temperature, and Pressure
13	Dew Point	degrees C	Dew Point, computed from Ambient Temperature and Relative Humidity

**Table A-5  
(Continued)**

	<b>Variable</b>	<b>Units</b>	<b>Description</b>
14	Relative Humidity	%	Relative Humidity, from R.M. Young Temperature/Relative Humidity Probe
15	Wind Speed	m/s	Wind Speed, from R.M. Young Wind Monitor AQ
16	Wind Direction	degrees	Wind Direction, from R.M. Young Wind Monitor AQ
17	U component	m/s	U Component from Wind Direction and Wind Speed
18	V component	m/s	V Component from Wind Direction and Wind Speed
19	W component	m/s	W Component, not available at current time

**Table A-6**  
**FLUXPAK Data File Contents**

	Variable	Units	Description
1	Year	N/A	Date of data collection, changes with 2400Z
2	Month	N/A	
3	Day	N/A	
4	Hour	N/A	Start time of data collection
5	Minute	N/A	
6	Seconds	N/A	
7	Height	meters AGL	Height of sensor package above ground level
	U component	m/s	East-West component of the wind
	V component	m/s	North-South component of the wind
	W component	m/s	Vertical component of the wind
	Virtual Temperature	K	Virtual Temperature as measured by the sonic anemometer
	Mxing Ratio	g/m <sup>3</sup>	Mixing Ration measured by the krypton hygrometer (not available in 95)
	u'u'	m <sup>2</sup> /s <sup>2</sup>	covariances
	u'v'	m <sup>2</sup> /s <sup>2</sup>	
	u'w'	m <sup>2</sup> /s <sup>2</sup>	
	u't'	Km/s	
	u'q'	g/m <sup>2</sup> s	
	v'v'	m <sup>2</sup> /s <sup>2</sup>	
	v'w'	m <sup>2</sup> /s <sup>2</sup>	
	v't'	Km/s	covariances
	v'q'	g/m <sup>2</sup> s	
	w'w'	m <sup>2</sup> /s <sup>2</sup>	
	w't'	Km/s	
	w'q'	g/m <sup>2</sup> s	
	t't'	K <sup>2</sup>	
	t'q'	Kg/m <sup>3</sup>	
	q'q'	g <sup>2</sup> /m <sup>6</sup>	
12	tke	m <sup>2</sup> /s <sup>2</sup>	Turbulent Kinetic Energy

**Table A-7**  
**Soil Data File Contents**

	Variable	Units	Description
1	Year		Date of data collection, changes with 2400Z
2	Month		
3	Day		
4	Hour		Start time of data collection
5	Minute		
6	Seconds		
7	Rain Period	minutes	Period for which (Rainfall) will be measured
8	Rainfall	inches	Inches of rainfall in (Rain Period)
9	Soil Depth	centime- ters	Depth of Soil Sensors from Ground Level
10	Soil Temperature	degrees C	Soil Temperature from REBS STP-1
11	Soil Moisture	Percent	Percent Water Content from REBS SMP-1
12	Total Hemi- spherical Radiation Incoming	W/m <sup>2</sup>	Incoming Radiation from REBS THRDS7
13	Total Hemi- spherical Radiation Outgoing	W/m <sup>2</sup>	Outgoing Radiation from REBS THRDS7
14	Net Radiation	W/m <sup>2</sup>	Incoming Radiation – Outgoing Radiation from REBS THRDS7

**Table A-8**  
**Atmospheric Profile File Contents**

	Variable	Units	Description
1	Month		Date of data collection, changes with 2400Z
2	Day		
3	Year		
4	Hour		Start time of data collection
5	Minute		
6	Seconds		
7	Height	meters	Height of measurement, with respect to ground
8	Ambient Temperature	degrees C	Ambient Temperature
9	Virtual Temperature	degrees C	Virtual Temperature
10	Potential Temperature	degrees C	Potential Temperature
11	Virtual Potential Temperature	Percent	Virtual Potential Temperature
12	U component	W/m <sup>2</sup>	East–West Wind Component
13	V component	W/m <sup>2</sup>	North–South Wind Component



## **APPENDIX B**

### **LIDAR SITE DESCRIPTIONS**

As described in Section 5., vortex data was collected at five different sites, representing three different scanning strategies, as described in Section 2.1.2. Surveys were performed on three of these sites by D. Mark Manning, P.E., P.L.S. of Collierville, TN. The two remaining sites, were measured by MIT Lincoln Lab personnel or estimated from airport maps. Refer to Appendix C for specific positions and altitudes of each site.

#### **B.1. Armory Site**

The Tennessee National Guard Armory is located under the approach path to runway 36R. A large open parking lot located on the northeastern side of the Armory building, offered ample space for siting the lidar van, and all of the auxiliary equipment. At the Armory site, the lidar was situated at three different locations in the parking lot. All Armory sites are shown in Figure B-1.

The armory site 1 is located on the northeast corner of the lot. The elevation of the surface at this site is 99.57 meters, the position is 35.008556N, and 89.975972W. The site is 20 meters from the northern edge of the parking lot, and 29 meters from the eastern edge of the parking lot. At the edge of the parking lot on the east side, the terrain rises on a moderate grade hill for a 2.5 meter rise. Trees located at the top of the hill were estimated to be 7-10 meters tall. This site is located 2,550 meters from the runway threshold, at an offset of 25 meters to the west.

The armory site 2 is the southern most site in the parking lot located 2600 meters from the runway threshold. The site position is 35.008111N, and 89.975917W, at an elevation of 99.98 meters mean sea level. The site is 25 meters from the eastern edge of the parking lot, and 70 meters from the northern edge of the parking lot. At the edge of the parking lot on the east side, the terrain rises on a moderate grade hill for a 2.5 meter rise. Trees located at the top of the hill were estimated to be 7-10 meters tall. The site is offset 21 meters to the west of the runway centerline. Figure B-2 shows a vertical cross section of the terrain from the site to the east.

The armory site 3 is located on the northwest corner of the parking lot. The position of the site is 35.008639W, and 89.976389N. The elevation of the site is 98.85 meters. The site is located 15 meters from the northern edge of the parking lot, 67 meters from the western edge, 30 meters from the southern edge, and 70 meters from the eastern edge. The site is 2,542 meters from the runway threshold, at a 64 meter offset to the west. To the south of the southern edge of the parking lot, is a fenced area containing parked military vehicles.

#### **B.2. TANG Site**

The Tennessee Air National Guard is located on the northern end of the airport, under the flight path of runway 18L and 36R. Large open areas of tarmac and grass field are located to the west of the TANG hangars, and aircraft parking area. At the TANG site, the lidar was located on an abandoned taxi-way just north of taxiway N. The elevation of the site is 74.35 meters mean sea level. The position is 35.067056W, and 89.975806N. The site is located 1,384 meters from runway threshold and is offset by 33 meters to the east.

#### **B.3. Tchulahoma Site**

The Department of Transportation, Volpe Center, set up a series of wind sensors, called a wind line, that measure wake turbulence of aircraft approaching runway 27. The lidar was sited near the

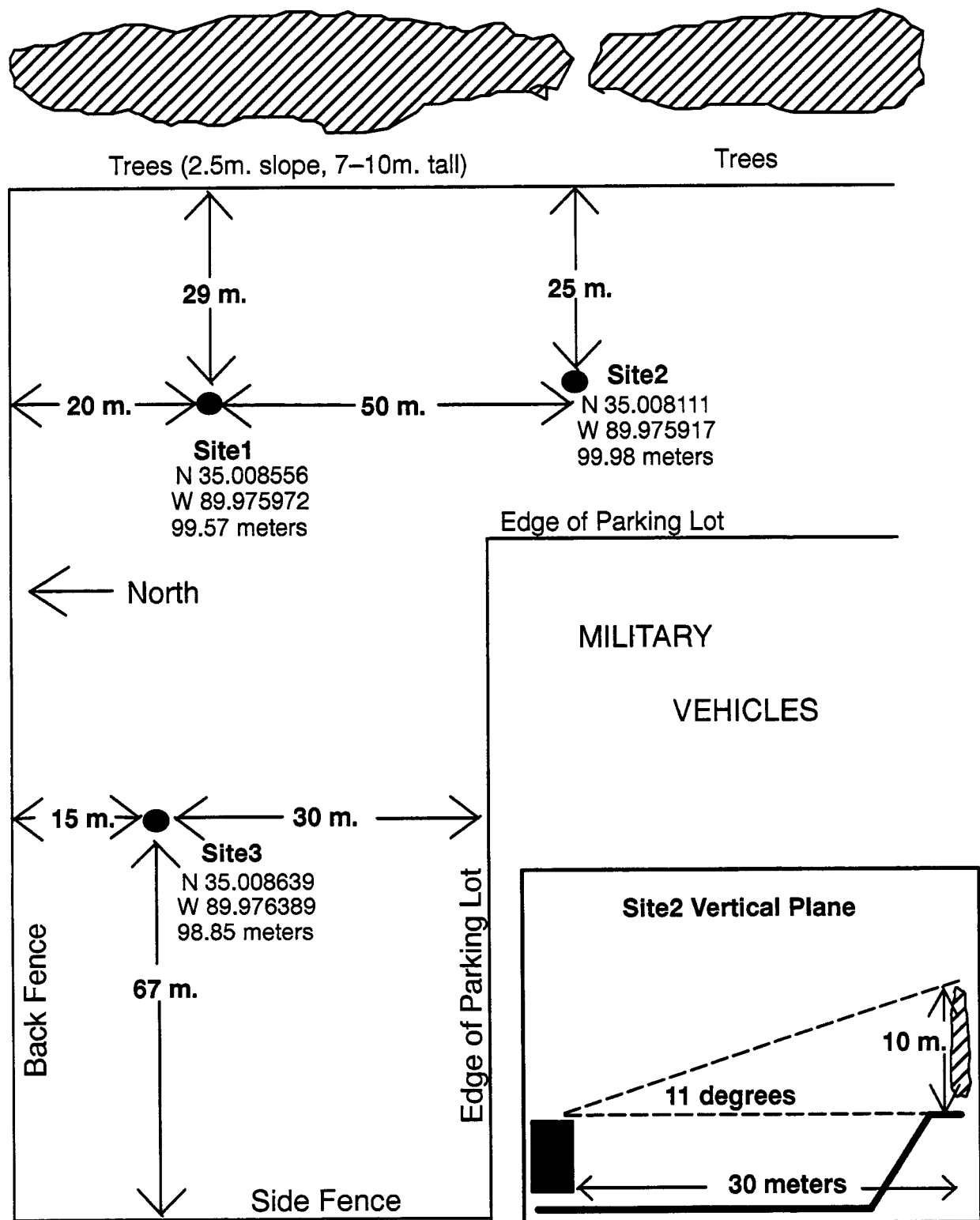


Figure B-1. Armory lidar sites.



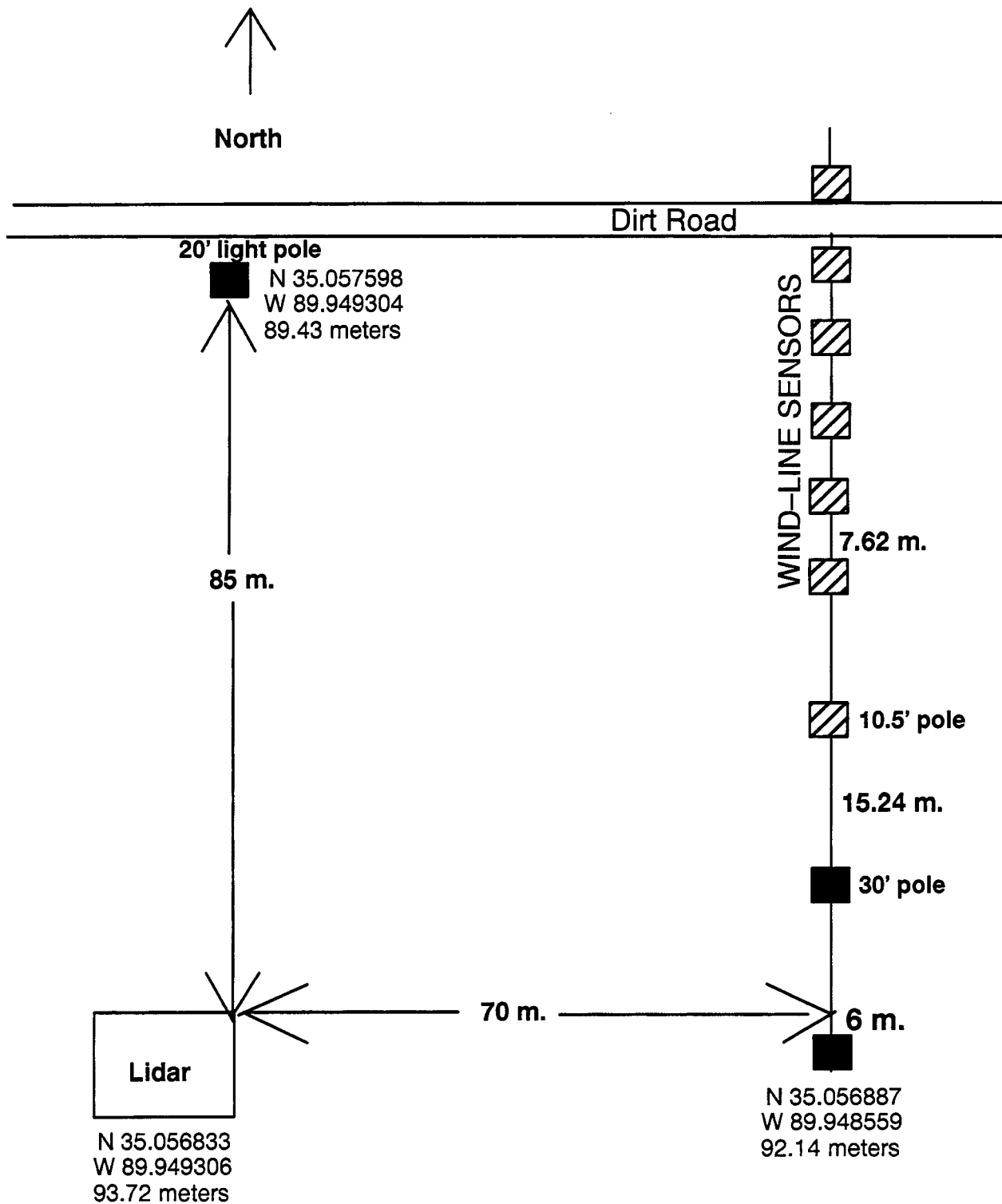
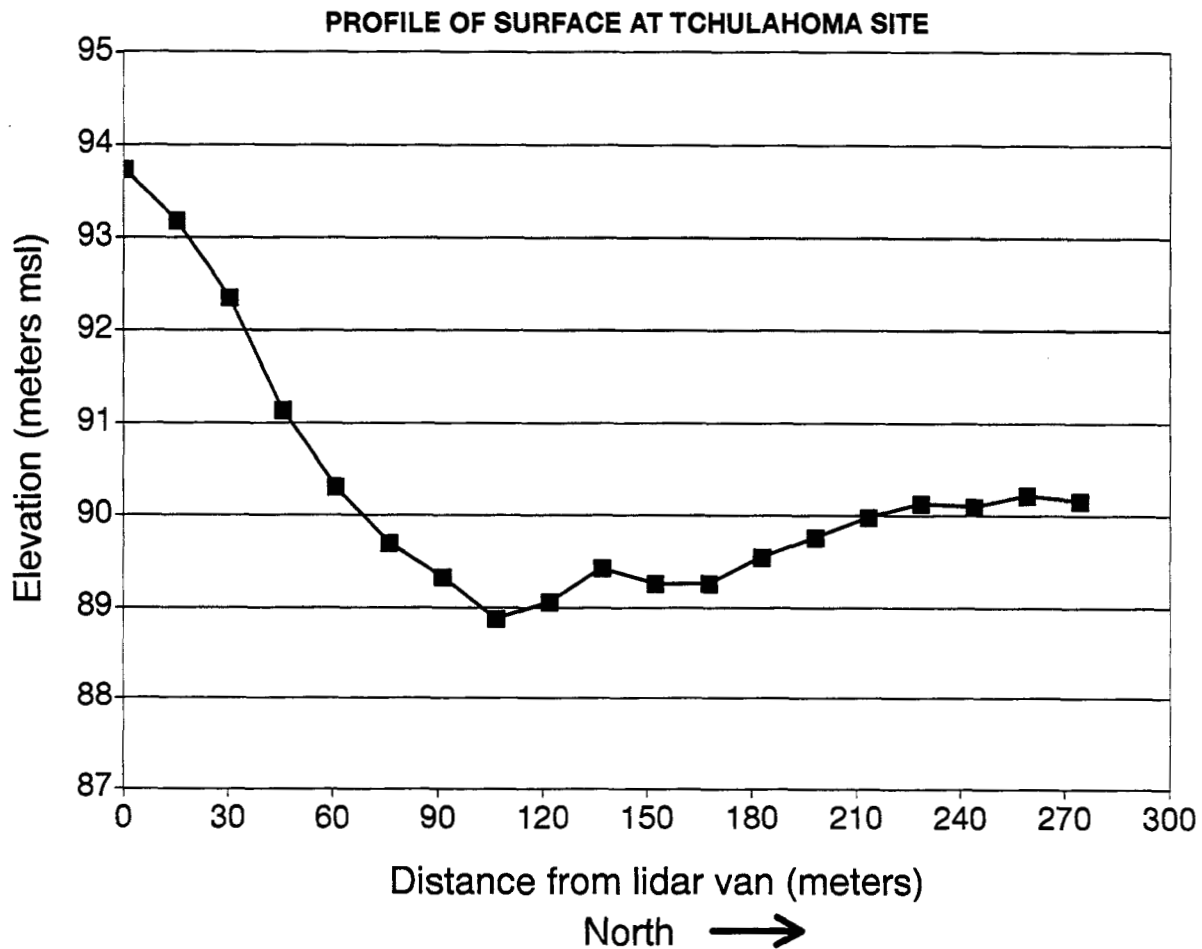


Figure B-2. Tchulahoma lidar site (plan view).

wind-line to co-measure the wake vortices. The Volpe site was on airport owned land along Tchulahoma Rd. on the east side of the airport. The Volpe wind line was 122 meters closer to the runway than the middle marker. The lidar van was 70 meters closer to the runway than the wind line. Figure B-2 shows the relation of the vortex van with the other sensors. The lidar scanned to the north at this site due to the low altitude of the aircraft. A vertical cross section of the terrain the vortices were traversing. Figure B-3 shows the profile across the approach parallel to the lidar scan. The lidar was situated at the highest point of 93.73 meters, the dirt road is at the lowest point of 88.88 meters. The lidar site position is 35.056833N, and 89.949301W. This site is 598 meters from the runway threshold and offset by 106 meters from runway centerline.



*Figure B-3. Tchulahoma lidar site (surface profile).*

#### **B.4. 27 Threshold Site**

Measurements were made at the threshold to runway 27 for making In-Ground-Effect measurements. As shown in Figure B-4, the lidar was parked along an access road to the tarmac where the Federal Express planes are parked. The lidar was 60 meters from runway threshold and offset by 135 meters. The position of this site is 35.058999N, and 89.955221W, at an elevation of 89.0 meters above mean sea level. The terrain was level, with a grassy field between the truck and the runway.

#### **B.5. Winchester Site**

The Winchester site is situated 135 meters beyond the runway threshold to 18L, at an offset of 225 meters. The elevation of this site is estimated at 81.4 meters, and the position is estimated at 35.053380N, and 89.973698W. A grassy field was between the lidar van and the runway.

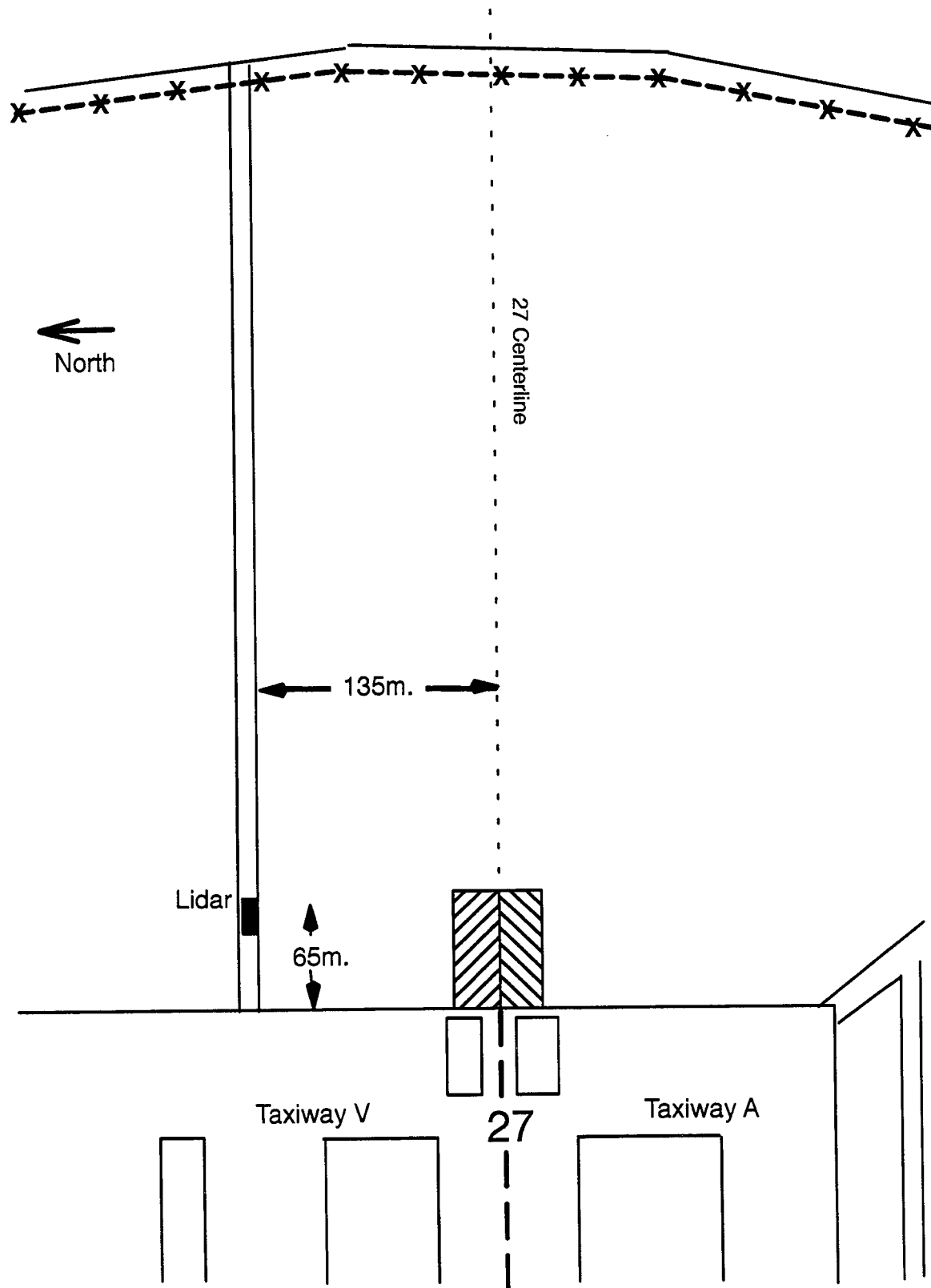


Figure B-4. Lidar sites along runway 27.

## APPENDIX C PARAMETER SETTINGS

The following tables summarize the parameter settings used during the field deployment. The lidar site parameters are in the runway axis coordinate system.

Name	Latitude	Longitude	Altitude (meters mean sea level)
150' Tower	35.029167	89.981111	97.37
Profiler/RASS	35.027589	89.981111	96.00
Sodar	35.027795	89.980862	96.00
Aircraft Surveillance Radar (ASR-9)	35.021917	89.980556	101.19
Airport Reference Point	35.045833	89.978167	101.2

Runway Name	Latitude	Longitude	Altitude (meters mean sea level)	Length (meters)	Orientation (degrees true north)
RW_18L	35.054595	89.976173	81.4	2560	179
RW_18R	35.049488	89.987443	87.5	2840	179
RW_27	35.057784	89.955881	89.0	2724	272
RW_36L	35.031520	89.986894	97.5	2840	359
RW_36R	35.031520	89.975688	101.2	2560	359
RW_9	35.058626	89.985722	77.1	2724	92

Site Name	Latitude	Longitude	Altitude (meters mean sea level)	Orientation (degrees true north)	Distance from Runway (meters)	Offset from Runway (meters)
18L_tang	35.067056	89.975806	74.35	179	1383	-57
18L_winchester	35.053380	89.973698	81.40	179	-135	-225
27_tchulahoma	35.056833	89.949301	93.72	272	601	-86
27_threshold	35.058999	89.955221	89.00	272	60	135
36R_armory_site1	35.008556	89.975972	99.56	359	2549	-70
36R_armory_site2	35.008111	89.975917	99.98	359	2599	-66
36R_armory_site3	35.008639	89.976389	99.85	359	2540	-108

<b>Aircraft ID</b>	<b>Aircraft Name</b>	<b>Wingspan (meters)</b>	<b>Maximum Arrival Weight (kilograms)</b>	<b>Maximum Departure Weight (kilograms)</b>	<b>Class</b>
AT42	Aerospatale/Aeritalia ATR-42	24.57	16,400	16,700	LARGE
B727	Boeing 727	32.92	61,236	64,400	LARGE
B737	Boeing 737	28.35	48,534	52,390	LARGE
B747	Boeing 747	59.64	285,765	351,535	HEAVY
B757	Boeing 757	38.05	89,810	104,325	LARGE
BA31	British Aerospace BAe Jetstream 31	15.85	7,080	7,350	LARGE
BE20	Beech Super King Air/Huron				SMALL
BE90	Beech King Air C90/E90	15.32	4,354	4,581	SMALL
C141					HEAVY
DC8	McDonnell Douglas DC-8	45.20			HEAVY
DC9	McDonnell Douglas DC-9	28.47	49,896	54,886	LARGE
DC10	McDonnell Douglas DC-10	50.40	182,798	263,085	HEAVY
EA30	Airbus A300	44.84	138,000	165,000	HEAVY
EA31	Airbus A310	43.89	122,000	138,600	HEAVY
EA32	Airbus A320	33.91	63,000	68,000	LARGE
FK10	Fokker 100	28.08	39,915	43,090	LARGE
FK27	Fokker Fellowship F28	29.00			LARGE
G2					LARGE
HS25	British Aerospace HS 125	15.66	10,590	12,430	LARGE
LR25	Gates Learjet 25				LARGE
MD11	McDonnell Douglas MD-11	51.66	195,048	273,521	HEAVY
MD88	McDonnell Douglas MD-88	32.87	58,060	63,503	LARGE
OV10					LARGE
SF34	SAAB/Fairchild Model 340A	21.44	12,020	12,700	LARGE

## APPENDIX D METEOROLOGICAL SENSOR CHARACTERISTICS

The meteorological data acquisition systems are listed below in Table D-1. The sensor and the parameters that the sensor measures are listed in the first two columns of the table. The next two columns, listed the measurement frequency (Data Collection Frequency) and time-averaging (Averaging Period) of the parameter. The last two columns listed the measurement range of the parameter as well as the measurement accuracy of the parameter. In some cases, this information is obtained from the sensor owner's manual, in other cases the information is obtained from discussions with the manufacturer.

**Table D-1  
Meteorological Sensor Characteristics**

Sensor	Parameter	Data Collection Frequency	Averaging Period	Range	Accuracy
R.M. Young Temp/RH sensor model 41372C	Temperature	1 Hz	1 min.	$\pm 50^{\circ}\text{C}$	$0.3^{\circ}\text{C}$
	Relative Humidity	1 Hz	1 min.	0–100%	2% 0–90% 3% 90–100%
R.M. Young Wind Monitor-AQ model 05305	Wind Speed	1 Hz	1 min.	0.4–40 m/s	2%
	Wind Direction	1 Hz	1 min.	0–360 degrees	3 degrees
Applied Technologies SWS-211/3Sx	Virtual Temperature	10 Hz	1 min.	$-20$ to $50^{\circ}\text{C}$	$0.05^{\circ}\text{C}$
	U Component	10 Hz	1 min.	$\pm 15$ m/s	0.05 m/s
	V Component	10 Hz	1 min.	$\pm 15$ m/s	0.05 m/s
	W Component	10 Hz	1 min.	$\pm 15$ m/s	0.05 m/s
Campbell Scientific Krypton Hygrometer KH-20	Mixing Ratio	20 Hz	1 min.	1–20 g/m <sup>3</sup>	0.5 g/m <sup>3</sup>
Vaisala Barometer PTA427	Pressure	1 Hz	1 min.	800–1100 mb.	0.15 mb.
Radiation Energy Balance Systems Total Hemispherical Radiometer THRDS7	Net Radiation	1 Hz	1 min.	$-1000$ – $2000$ W/m <sup>2</sup>	N/A
	Total Hemispherical Radiation Incoming	1 Hz	1 min.	$-1000$ – $2000$ W/m <sup>2</sup>	N/A
	Total Hemispherical Radiation Outgoing	1 Hz	1 min.	$-1000$ – $2000$ W/m <sup>2</sup>	N/A
Radiation Energy Balance Systems Soil Moisture Probe SMP-1	Temperature	1 Hz	1 min.	$\pm 50^{\circ}\text{C}$	$0.05^{\circ}\text{C}$

**Table D-1  
(Continued)**

Sensor	Parameter	Data Collection Frequency	Averaging Period	Range	Accuracy
Radiation Energy Balance Systems Soil Temperature Probe STP-1	Soil Moisture	1 Hz	1 min.	0-35 % Water Content	N/A
Texas Electronics Tipping Bucket Rain Gauge TE525	Rain Rate	0.01"	1 min.	0-2" /hr.	1 %
Radian Corp. LAP3000 (Profiler)	Wind Speed	N/A	25 min.	0-51m/s	1 m/s
	Wind Direction	N/A	25 min.	0-360 degrees	10 degrees
Radian Corp. RASS	Virtual Temperature	N/A	5 min.	$\pm 32^{\circ}\text{C}$	1 $^{\circ}\text{C}$
Aerovironment M2000 Sodar	Wind Speed	N/A	10 min.	0-35m/s	0.3 m/s
	Wind Direction	N/A	10 min.	0-360 degrees	5 degrees
	W Component	N/A	10 min.	$\pm 5\text{m/s}$	5 cm/s
Remtech PA2 Sodar	Wind Speed	N/A	10 min.	0-40m/s	0.2 m/s if wind speed < 6m/s otherwise, 3% of wind speed
	Wind Direction	N/A	10 min.	0-360 degrees	5 degrees
	W Component	N/A	10 min.	$\pm 4\text{m/s}$	5 cm/s
LORAN CLASS sounding system	Temperature	2 Hz.	10 sec.	$\pm 50^{\circ}\text{C}$	1 $^{\circ}\text{C}$
	Relative Humidity	2 Hz.	10 sec.	0-100 %	3 %
	Wind Speed	2 Hz.	60 sec.	0-50 m/s	1 m/s
	Wind Direction	2 Hz.	60 sec.	0-360 degrees	10 degrees
	Pressure	2 Hz.	10 sec.	50-1100 mb	1 mb.



## ACRONYMS AND ABBREVIATIONS

AC	Alternating Current
ADAM	Aster Data Acquisition Module
ASDE	Airport Surface Detection Equipment
ATC	Air Traffic Control
DC	Direct Current
DSP	Digital Signal Processor
FAA	Federal Aviation Administration
FFT	Fast Fourier Transform
FWHM	Full Width at Half Maximum
GMT	Greenwich Mean Time
GUI	Graphical User Interface
IDL	Interactive Data Language
IGE	In Ground Effect
LOS	Line of Sight
MAVSS	Monostatic Acoustic Vortex Sensing System
NASA	National Aeronautics and Space Administration
NCAR	National Center for Atmospheric Research
OGE	Out of Ground Effect
NGE	Near Ground Effect
RASS	Radio Acoustic Sounding System
REBS	Radiation Energy Balance Systems
RH	Relative Humidity
RTD	Resistance vs. Temperature Device
SHM	Shared Memory
Sodar	Sonic Radar
TCP-IP	Transmission Control Protocol-Internet Protocol
TKE	Turbulent Kinetic Energy



## GLOSSARY OF MATHEMATICAL SYMBOLS

$\Psi$	Maximum velocity of a spectrum (m/s).
$C$	Expected line-of-sight ambient wind velocity of a spectrum (m/s).
$A$	Power contained in a velocity spectral bin.
$N$	Noise floor amplitude.
$n$	Number of bins per spectrum.
$P_{fl}$	Polarity of the frequency lock between the master and local oscillators.
$f_{BW}$	Lidar system bandwidth (MHz).
$\lambda$	Wavelength of lidar (m).
$K_{zd}$	Spectral bin corresponding to zero Doppler.
$ZF$	Pseudo-altitude of lidar focus point, uncorrected for beam path inside the truck and height of scan mirror above ground (m).
$F$	Focus range of lidar (m).
$\theta$	Scan mirror angle of lidar (rad).
$X$	Vortex detection filter.
$\delta$	Direction of scanning of lidar.
$c$	Number of samples for core radius of vortex detection filter.
$p$	Number of samples for half-width of vortex detection filter.
$\varsigma$	Average cross-range resolution of spectra in a lidar scan (m).
$\Lambda$	Convolution of vortex detection filter with spectrum maximum velocities for a lidar scan.
$T_{CONV}$	Minimum absolute convolution value for a valid vortex detection.
$\Phi$	Detected vortex angle (rad).
$\Lambda_{MAX}$	Absolute convolution value at the detected vortex angle for this scan.
$VA$	Location of the wind peak of a spectrum.
$I_{cw}$	Crosswind profile vertical sampling interval (m).
$N_{aw}$	Minimum number of standard deviations above the noise floor for a valid spectrum wind peak.
$CW_{SPECT}$	Spectrum crosswind estimate (m/s).
$CW_{SCAN}$	Scan crosswind estimate (m/s).
$N_{SCAN}$	Number of spectrum crosswind estimates used in scan crosswind estimate.
$CW_{COMP}$	Composite crosswind estimate (m/s).
$\alpha$	Composite crosswind formation aging coefficient.

$T$	Age of a scan relative to the most recent scan (s).
$\tau_{AW}$	Composite crosswind formation aging time constant.
$F_{slack}$	Maximum focus range deviation from estimated vortex range (m).
$F_{min}$	Minimum focus range (m).
$F_{max}$	Maximum focus range (m).
$\theta_{min}$	The smallest scan angle for a given scan (rad).
$\theta_{max}$	The largest scan angle for a given scan (rad).
$\zeta_{slack}$	Distance in cross-range to scan around a vortex (m).
$\Delta\Phi_{MAX}$	Maximum allowed scan angle difference for the two vortices for multiple vortex tracking (rad).
$R$	Estimated vortex range (m).
$\Delta R_{MAX}$	Maximum allowed difference in range for the two vortices for multiple vortex tracking (m).
$c$	Number of samples for core radius of vortex detection filter.
$\Gamma$	Vortex Circulation ( $m^2/s$ )
$V_{los}$	Lidar line-of-sight velocity in a vortex (m/s)
$r$	Distance from the core of a vortex (m)
$V_{TAS}$	True Air Speed of an aircraft (m/s)
$W$	Aircraft weight (kg)
$b$	Aircraft wingspan (m)
$\rho$	Air density ( $kg/m^3$ )
$g$	Gravitational acceleration ( $m/s^2$ )
$r_s$	Separation distance between vortex cores
$V_{mv}$	Spectrum maximum velocity
$a_{mv}$	Spectrum amplitude at $V_{mv}$
$a_{mv}$	Spectrum amplitude at first spectrum peak below $V_{mv}$
$V_{mmv}$	Modified maximum Doppler spectrum velocity
$S$	Hanning Window function
$s$	Fourier Transform of Hanning Window function

## REFERENCES

- Burnham, D.C. (1977), "Review of Vortex Sensor Development since 1970," Proc. of the Aircraft Wake Vortex Conference, FAA-RD-77-68, Cambridge, MA.
- Campbell, S.D., Dasey, T. J., Heinrichs, R.M. and M. P. Matthews (1995), "Overview of 1994 Memphis Wake Vortex Testing Program," Proc. Sixth Conference on Aviation Weather Systems, American Meteorological Society, Boston, MA, pp. 515-520.
- Constant, G., Foord, R., Forrester, P.A., and J.M. Vaughan (1994), "Coherent laser radar and the problem of aircraft wake vortices," *J. Modern Optics*, 41(11), 2153-2173.
- Dasey, T. J., and R. Heinrichs (1995), "An Algorithm for the Recognition and Tracking of Aircraft Wake Vortices with a Continuous Wave Coherent Laser Radar," in *Coherent Laser Radar*, Vol. 19, 1995 OSA Technical Digest Series (Optical Society of America, Washington DC, 1995), 193-196.
- Evans, J.E. and J.D. Welch (1991), "Role of FAA/NWS Terminal Weather Sensors and Terminal Air Traffic Automation in Providing a Vortex Advisory Service," Aircraft Wake Vortex Conference, Washington, D.C., pp. 24-1 to 24-22.
- Greene, G.C. (1986), "An Approximate Model of Vortex Decay in the Atmosphere," *J. Aircraft*, 23, 566-573.
- Hannon, S. M. and J. A. Thomson (1994), "Aircraft wake vortex detection and measurement with a solid-state coherent laser radar," *J. Modern Optics*, 41(11), 2175-2196.
- Heinrichs, R.M, Freehart, R.E., Dasey, T.J. and Mandra, R.S. (1995), "Development and Performance of a CW Coherent Laser Radar for Detecting Wake Vortices," in *Coherent Laser Radar*, Vol. 19, 1995 OSA Technical Digest Series (Optical Society of America, Washington DC, 1995), 186-189.
- Heinrichs, R.M., Dasey, T.J., Matthews, M.P., Campbell, S.D., Freehart, R.E., Perras, G.H., and P. Salamitou (1996), "Measurements of aircraft wake vortices at Memphis International Airport with a CW CO<sub>2</sub> coherent laser radar," Proc. SPIE 10th International Aerosense Symposium, Air Traffic Control Technologies II, Vol. 2737, 122-133.
- Hinton, D.A. (1995), "Aircraft Vortex Spacing System (AVOSS) Conceptual Design," NASA Technical Memorandum 110184, NASA Langley Research Center, Hampton, VA.
- Huffaker, R.M., Jelalian, A.V. and J.A. Thomson (1970), "Laser Doppler System for Detection of Aircraft Trailing Vortices," Proc. IEEE, 58(3), 322-326.
- Koepp, F. (1991), "The infrared Doppler lidar: an important tool for experimental investigation of aircraft wake vortices," in *Technical Digest on Coherent Laser Radar: Technology and Applications* (Optical Society of America, Wash., DC), 12, 306-308.
- Matthews, M., Dasey, T. J., Perras, G. H. and S. D. Campbell (1997), "Planetary Boundary Layer Measurements for the Understanding of Aircraft Wake Vortex Behavior," to appear in Proc. Seventh AMS Conference on Aviation Weather Systems, Feb. 2-7 1997, Long Beach, CA.
- Olsen, J.H., Goldberg, A. and Rogers, M (1971), *Aircraft Wake Turbulence and Its Detection*, Plenum Press, New York-London.

- Page, R.D, Clawson, K.L., Garodz, L.J. and Rudis, R.P. (1991) "Panel Discussion on Tower Fly-By Testing - 1990 Fall Series," Aircraft Wake Vortex Conference, Washington, DC, pp. 49-1 - 49-50.
- Salamitou, P. and R.J. Hansman (1995), "An Algorithm for CW Doppler Lidar Wake Vortex Remote Sensing," in *Coherent Laser Radar*, Vol. 19, 1995 OSA Technical Digest Series (Optical Society of America, Washington DC, 1995), PDP 3-2.
- Salamitou, P., Hansman, R.J., Dasey, T.J. and R.M. Heinrichs (1996) "Range Estimation for CW Lidar Aircraft Wake Vortex Detection," submitted to *Appl. Opt.*